Design and Evaluation of a Monte Carlo Model of a Low-Cost Kilovoltage X-ray Arc Therapy System

by

Dylan Yamabe Breitkreutz

BSc, University of Alberta, 2012
MSc, University of Alberta, 2015

A Dissertation Submitted in Partial Fulfillment
of the Requirements for the Degree of

DOCTOR OF PHILOSOPHY

in the Department of Physics and Astronomy

© Dylan Yamabe Breitkreutz, 2019
University of Victoria

All rights reserved. This dissertation may not be reproduced in whole or in part, by photocopy or other means, without permission of the author.

Supervisory Committee

Design and Evaluation of a Monte Carlo Model of a Low-Cost Kilovoltage X-ray Arc Therapy System

by

Dylan Yamabe Breitkreutz
BSc, University of Alberta, 2012
MSc, University of Alberta, 2015

Supervisory Committee

Dr. Magdalena Bazalova, Supervisor
Department of Physics and Astronomy

Dr. Sergei Zavgorodni, Member
Department of Physics and Astronomy

Dr. Imir Thomo, Outside Member
Department of Computer Science

Abstract

There is a growing global need for proper access to radiation therapy. This need exists predominantly in low- and middle-income countries but exists in some high-income countries as well. The solution to this problem is complex and requires changes in government policy, education and technology. The objective of the work contained in this dissertation is the development of a novel external beam radiation therapy system capable of treating a variety of cancers. The intent of this system is to provide a cost-effective radiation therapy system, which can primarily be utilized in low- and middle-income countries. This new system uses kilovoltage rather than megavoltage x-rays and is therefore much more cost-effective. The ultimate purpose of this kilovoltage radiation therapy system is to improve access to radiation therapy worldwide by supplementing current radiation therapy technology.

As a first step, the kilovoltage x-ray arc therapy or KVAT system was modeled using the EGSnrc BEAMnrc and DOSXYZnrc Monte Carlo software tools. For this initial study 200 kV arc-therapy was simulated on cylindrical water phantoms of two sizes, each of which contained a variety of planning target volume (PTV) sizes and locations. Additionally, prone and supine partial breast irradiation treatment plans were generated using KVAT. The objective of this work was to determine whether or not skin-sparing could be achieved using the KVAT system while also delivering a clinically relevant dose rate to the PTV. The results of the study indicated that skin-sparing is indeed achievable and that the quality of KVAT treatment plans improves for full 360-degree arcs and smaller PTV sizes.

The second step of this project involved the Monte Carlo simulation of KVAT treatment plans for breast, lung and prostate cancer. Spherical PTVs of 3-cm diameter were used for the breast and lung treatment plans while a 4-cm diameter PTV was used for prostate. Additionally,

inverse optimization was utilized to make full use of the non-conformal irradiation geometry of KVAT. As a means of comparison, megavoltage treatment plans that could be delivered by a clinical linear accelerator were generated for each patient as well. In order to evaluate the safety of KVAT treatment plans, dose constraints were taken from published Radiation Therapy Oncology Group (RTOG) reports. The results of this study indicated that the 200 kV breast and 225 kV lung KVAT treatment plans were within dose constraints and could be delivered in a reasonable length of time. The 225 kV prostate treatment plan, while technically within dose constraints, delivered a large dose to non-critical healthy tissues due to the limited number of beam angles that did not pass through boney anatomy. It was concluded that plans such as prostate with large volumes of bone present might not be feasible for KVAT treatment.

The third step aimed to expand upon previous work and simulated more realistic KVAT treatment plans by using PTV volumes contoured by radiation oncologists. Additionally, this study used a completely redesigned KVAT geometry, which employed a stationary reflection anode and a new collimator design. The design modeled in this study was based upon the specifications of the prototype system under construction by PrecisionRT, a commercial partner. Three stereotactic ablative radiotherapy (SABR) lung patients were selected that had received treatment at the Vancouver Island Cancer Centre. In order to fully cover the PTVs of each patient, spherical sub-volumes were placed within the clinically contoured PTV of each patient. Dose constraints for at-risk organs were taken from an RTOG report on stereotactic body radiation therapy and were used to inversely optimize the 200 kV KVAT treatment plans. The calculated KVAT plans were compared with the clinical 6 MV SABR plans delivered to each patient. The results of this study indicated that KVAT lung plans were within dose constraints for

all three patients with the exception of the ribs in the second patient who had a tumor directly adjacent to the rib cage.

The fourth and last step of this project was the experimental validation of a simple, proof-of-principle KVAT system. Simple geometric methods were used to design a collimator consisting of two slabs of brass separated by ~6 cm, each with 5 apertures, which would create an array of 5 converging beamlets. The collimator was used with a tabletop x-ray tube system. A rectangular solid water phantom and cylindrical TIVAR 1000 phantom were placed on a rotation stage and irradiated using 360-degree arcs. EBT3 gafchromic film was placed in each phantom to measure two-dimensional dose distributions. Film dose distributions were analyzed and compared to Monte Carlo generated dose distributions. Both the rectangular solid water phantom and cylindrical TIVAR phantom showed skin-sparing effects in their dose distributions. The highest degree of skin-sparing was achieved in the larger, 20 cm diameter cylindrical phantom. Furthermore, the measured film data and calculated metrics of the rectangular phantom were within 10% of the MC calculated values for two out of three films. The discrepancy in the third film can be explained by errors in the experimental setup.

In conclusion, the work contained in this dissertation has established the feasibility of a cost-effective kilovoltage arc-therapy system designed to treat deep-seated lesions by means of Monte Carlo simulations and experimental dosimetry. The studies performed so far suggest that KVAT is most suitable for smaller lesions in patient anatomy that does not involve large amounts of boney anatomy. Perhaps most importantly, an experimental study has demonstrated the skin-sparing ability of a simple KVAT prototype.

Table of Contents

List of Figures

List of Tables

Acknowledgments

I strongly believe that the correct choice of research project is only half of what is necessary for a successful and enjoyable PhD experience. Of equal, if not greater importance in my opinion, is the choice of supervisor. I am thoroughly grateful for my learning experience under the mentorship of Dr. Magdalena Bazalova-Carter who has a seemingly limitless amount of knowledge and time for her students and is a genuinely wonderful person. I am lucky we randomly met at a conference and I asked her to be my PhD advisor.

I would like to acknowledge Dr. Michael Weil for his expertise in radiation oncology and for an excellent collaboration experience throughout my PhD. Michael was the progenitor of the cost-effective radiation therapy system upon which my entire PhD work was based.

Also of great importance was my collaboration with Dr. Marc-André Renaud and Dr. Jan Seuntjens of McGill University who developed the inverse optimization engine I used in my work.

I would also like to thank Dr. Sergei Zavgorodni for his help with obtaining patient data for my work from the Vancouver Island Cancer Centre and for helping with the simulation of clinical treatment plans.

I am grateful to Dr. Douglas Boyd, Dr. Samuel Song, Dr. Jaeyoung Han and Dr. Michael Weil (and all others) of PrecisionRT and Imatrex for their roles in the parallel development and production of the radiation therapy system designed and evaluated in my work. I am also thankful for their generous donation of a computing-cluster, which greatly improved the computation resources available to me.

I am also thankful to Dr. Chris Johnstone, Nolan Esplen and Henry Baxter for their assistance in other aspects of my work - Chris for his help with the small animal radiation

research platform, Nolan for teaching me about radiochromic film dosimetry and Henry for his coding work and expertise.

Finally, I would like to thank my family, Alistair Kornelsen, Dale Breitkreutz, Carol Breitkreutz, Sara Breitkreutz, Henry Smith and Nori Smith, for their constant support.

This work was supported by an NSERC Vanier scholarship and an AAPM graduate fellowship.

1. Introduction

Radiation therapy (RT) is a critical tool in the treatment of cancer. With one half of cancer patients receiving RT in some form during their treatment[2], there is a high demand for access to RT services. Unfortunately, there is a global disparity in access to RT between high-income and low- and middle-income countries. While the solution to this disparity is complex and requires change in technology, education and government policy, the development of a cost-effective RT technology would be a step in the right direction. The main objective of this PhD research is the design, simulation and experimental validation of a novel, low-cost kilovoltage x-ray arc therapy (KVAT) system. The KVAT system potentially brings three main benefits to the field of RT and the treatment of cancer. Firstly, the x-ray tubes and accompanying technology necessary to generate kilovoltage (kV) photons are far less expensive and complicated than the medical linear accelerators (linacs) needed to generate the megavoltage (MV) photons. Linac generated MV photons are the primary external beam RT technique used in the cancer clinic. Secondly, the lower energy of kV photons requires far less shielding than MV photons. While a linac vault requires approximately 7 feet of concrete to safely house clinical accelerators, only 5 mm of lead would be required for a machine operating at 200 kV. This difference results in a large difference in infrastructure cost. The third benefit of the KVAT system is its capability for image-guided RT. For imaging, kV photons are preferred as they produce higher quality radiographic images than MV photons. The KVAT system will be capable of kV imaging during treatment due to the dual function of the kV x-ray source. While linacs are able to image with both kV and MV photons, the kV photon source is separate from the MV source and is not designed for image-guided RT. This work represents necessary steps in the successful development of the KVAT system, which will provide a low-cost radiation therapy technology to treat deep-seated lesions and supplement the global cancer care system.

1.1 Radiation Therapy

The main method used in RT is the irradiation of lesions with MV photons generated from a medical linac. While RT has proven to be an effective means of controlling the growth of cancerous lesions through cell killing, it is also destructive to healthy tissue. For this reason, one of the most important problems in RT is the delivery of a therapeutic dose to the malignant lesion while sparing as much healthy tissue as possible. If healthy tissues receive too much dose the patient will be at risk of short and long-term complications. These complications vary in severity and range from superficial skin damage to tissue necrosis and secondary, radiation-induced tumours.

In an attempt to spare as much healthy tissue as possible many advancements in external beam RT have aimed to increase the accuracy and conformality (the property of how well the radiation field matches the malignant lesion volume) of treatments. Of particular importance to this work is volumetric modulated arc therapy (VMAT), an advanced technique which has been implemented widely in clinics within the last 10 years[3]. During a VMAT treatment, radiation is delivered in a continuous arc while dynamically modulating the radiation field with multi-leaf collimators, resulting in highly conformal radiation delivery. Due to the complicated modulation of VMAT treatments they must be generated using computer optimization techniques.

1.2 Radiotherapy in Low and Middle-Income Countries

Recent studies have highlighted the disparity between RT access in high-income and low- and middle-income countries (LMICs) and the imperative need to address the problem[2,4–11]. Increasing incidence rates of cancer compounds this problem. In 2012 there were 8 million new cases of cancer in LMICs and the incidence rate is projected to increase to 14.7 million new cases in 2035[10]. Additionally, the majority of cancer deaths occur in LMICs[4]. Not only are the majority of cancer cases arising in LMICs but these countries also lack the radiotherapy

resources needed to treat their patients. Datta et al. estimated a deficit of almost 7000 external beam radiotherapy systems in 2014 in LMICs[6]. North America has approximately 12 MV RT machines per million people while Africa has approximately 0.25 MV RT machines per million people[11]. The solution to this problem is complex and must be addressed from many directions including government policy, infrastructure, technology and education.

1.3 Dissertation Objectives

There are four main studies involved in this work. The first study involved proof-of-principle Monte Carlo (MC) simulations of KVAT irradiation of water phantoms and breast lesions. The second study used the MC model of the KVAT system to simulate inversely optimized treatments of idealized, spherical PTVs in breast, lung and prostate patients. The third step extends inversely optimized KVAT to clinical lung patients with non-spherical lesions. The final step of this research will be to experimentally validate a prototype KVAT system in order establish confidence in the MC KVAT model. The beginning of this dissertation will contain relevant background information. Following the background knowledge will be the published work created during this PhD project. Before each manuscript I will endeavor to briefly discuss what work was performed and establish the work in the context of the whole dissertation.

2. Background

2.1 Production of X-Rays

The x-rays used in external beam RT are generated by the collision of high-energy electrons with a high-Z target. The method of electron acceleration and the design of the target differ between an x-ray tube, which is used for the production of kV x-rays, and a linac, which produces MV x-rays. However, the physics describing the generation of x-rays is the same in both machines. When an electron is incident upon a target both radiative collisions and ionizational collisions can occur[12]. In an ionizational interaction, the incident electron interacts with an outer orbital electron of an atom in the target. The result is a deflection of the incident electron and a transfer of energy to the orbital electron, which is ejected from the atom. As a result, the atom becomes ionized as it is now positively charged. If the ejected electron has sufficient energy to create its own secondary chain of interactions, it is called a delta ray. It is possible the incident electron will not transfer enough energy to the orbital electron to eject it. In this case the orbital electron is displaced from its stable position and shortly returns back to it[13]. This process is known as excitation. Incident electrons primarily undergo ionizational interactions within the target and transfer only a fraction of their energy with each interaction. The end result of all ionizational interactions within the target is heat generation. Less commonly, the incident electron will undergo a radiative interaction and emit a photon. A bremsstrahlung photon is emitted when the incident electron interacts with the electromagnetic field of the atomic nucleus resulting in rapid deceleration and deflection of the electron. Due to this rapid energy loss, a photon is created in the braking process due to energy conservation[13]. The energy loss of the incident electron ranges from partial to complete. As a result, bremsstrahlung photons are emitted in a continuous energy range up to the maximum energy of the incident electron. Furthermore, characteristic x-rays can be produced in consequence of

ionizational interactions due to the ejection of orbital electrons. After an orbital electron is ejected, an electron from a higher energy state occupies the vacancy and loses energy. A photon with energy equal to the difference between the higher and lower energy states is then emitted[13]. The efficiency (percentage of electron energy converted to x-rays) for bremsstrahlung is given by

$$Efficiency = 9\times10^{-10} \cdot ZV \quad (1)$$

where Z is the atomic number of the target and V is the x-ray tube voltage[13]. The dependence of this equation on atomic number partially explains the common choice of tungsten (Z=74) for targets. At kilovoltage energies, incident electrons lose approximately 99% of their energy in ionizational interactions and only about 1% in radiative interactions. MV electrons are more efficient with approximately 15% of their energy being emitted (at 20 MeV) as bremsstrahlung photons[12]. In both cases a large amount of heat is generated which constitutes the rest of the explanation for the common choice of tungsten for targets as it has a high melting point.

The angular distribution of emitted x-rays depends on both the energy of incident electrons as well as the thickness of the target. This is important to note as it influences the design of x-ray tubes and linacs that, consequently, must employ very different target geometries. For a thin target and kV energies, the majority of x-rays are radiated at right angles to the original direction of the electron beam. As the energy of the incident electrons increases the distribution shifts towards the initial electron direction. At MV energies, the majority of x-rays are emitted in the forward direction[12].

2.2 X-Ray Tubes

Figure 2.1 illustrates the basic design of an x-ray tube, which consists of a tungsten filament coil (cathode) and an angled tungsten target (anode) embedded in heat sink, all of which is enclosed in an evacuated housing. A thin window exists below the target through which the

photons exit the x-ray tube and serves to filter out any scattered electrons coming from the target. An electric potential is created between the cathode and anode. A current applied to the cathode boils off electrons from the filament, which are accelerated towards the anode. Due to the vacuum between the cathode and anode, the electrons accelerate to high speeds before colliding with the anode to produce x-rays.

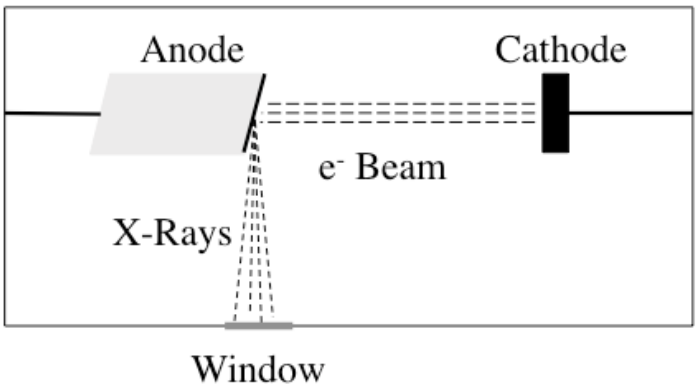

Figure 2.1 – Diagram of a simple x-ray tube.

The shape of the photon beam created by an x-ray tube depends on the dimensions of the focal spot (area over which electrons strike the anode), which in turn depends on the dimensions of the electron beam and the angle of the anode. The size of the focal spot is particularly important to the design of an x-ray tube since a smaller focal spot will generate more heat per cm^2 of the anode and is more likely to cause melting. Additionally, a smaller focal spot creates a sharper beam and is therefore preferred for imaging applications. The size of the focal spot can be effectively reduced by using the principle of line focus, which states that

$$a = Asin\theta \quad (2)$$

where a is the effective focal spot size, A is the actual focal spot size and $\boldsymbol{\theta}$ is the angle of the anode[13].

The specific design of an x-ray tube depends on its purpose. An imaging x-ray tube needs to produce a sharper photon beam in order to produce high quality images and operates at high currents but does not operate continuously or at higher energies. As a result, imaging x-ray tubes use a smaller focal spot and mitigate heating issues with rotating anodes in order to distribute the generated heat over a wider portion of the anode surface. Therapy x-ray tubes, on the other hand, can use a much larger focal spot but need to operate continuously. These considerations result in therapy tubes employing a stationary anode embedded in a large copper heat sink for heat management. The last characteristic of note with regards to x-ray tubes is the "heel effect" which is characterized by the uneven fluence of photons coming from the anode. Since not all photons are generated at the surface of the anode, but rather at some depth, there will be fewer photons in the portion of the beam distal to the cathode due to attenuation within the anode. In addition, due to this attenuation the distal portion of the beam will have a higher mean energy due to the removal of lower energy photons.

2.3 Linear Accelerators

Figure 2.2 illustrates a block diagram of the major components of a linear accelerator. In order to achieve MV energies, electrons from an electron gun are accelerated through a waveguide. Within the waveguide electrons gain energy by interacting with pulsed electromagnetic waves generated in the magnetron. Once the electrons leave the waveguide they are bent by bending magnets, which also helps filter out electrons of incorrect energy, and impact the tungsten target creating MV bremsstrahlung photons. The photons then pass through treatment head of the machine which houses a primary static collimator, flattening filter, ionization chambers, secondary dynamic collimators, multi-leaf collimator (MLC) and an exit window. Critical to VMAT is the MLC, which consists of two sets of moveable tungsten leaves. Each leaf is able to individually move into or out of the photon field resulting in modulation of

the photon beam. Typical linear accelerators in clinics today are capable of generating energies up to 22 MV.

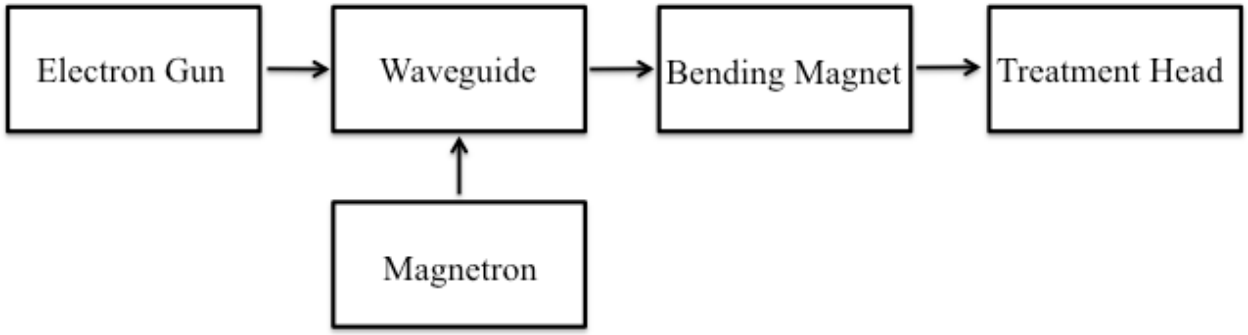

Figure 2.2 – Block diagram of main linac components. Adapted from Khan[13].

2.4 The Interaction of X-Rays in Matter

As x-rays pass through a medium they transfer some of their energy through interactions with that medium. There are four main mechanisms by which photons interact with matter. The probability of any one of these interactions occurring is given by its cross-section and depends primarily upon the energy of the photon and the atomic number or the electron density of the interacting matter.

2.4.1 Rayleigh Scattering

Rayleigh or coherent scattering occurs when a photon interacts with the combined electromagnetic field of orbital electrons. Through this interaction the photon is scattered from its original path but no energy is transferred. The cross section of coherent scattering decreases with energy and increases with atomic number[14]. Figure 2.3 illustrates the cross-section of Rayleigh scattering for water and tungsten for photons with energy of 1 keV to 10 MeV. A scattering mechanism similar to Rayleigh scattering is Thomson scattering by which a photon may be elastically scattered by a free electron.

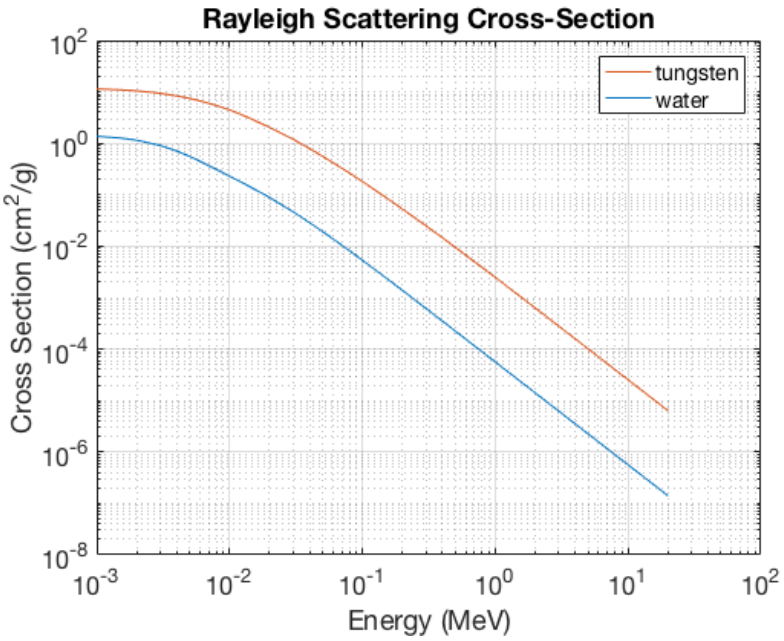

Figure 2.3 – Cross-section of Rayleigh scattering in water and tungsten. Data taken from XCOM: Photon Cross-Sections Database.

2.4.2 Photoelectric Effect

It is possible for an incident photon to be completely absorbed by an atomic nucleus. After this occurs the photon's energy is transferred to an orbital electron in the K, L, M or N shell and is ejected with energy equal to the absorbed photon energy minus the binding energy of the electron (which is now called a photoelectron). A higher energy orbital electron quickly fills the vacancy left by the emitted photoelectron and a characteristic x-ray is emitted. These characteristic x-rays may leave the atom or they may interact with and eject other orbital electrons. Electrons ejected by characteristic x-rays are known as Auger electrons. The photoelectric cross-section is proportional to $\frac{Z^3}{E^3}$, where E is the energy of the photon. Figure 2.4 shows the cross-section of the photoelectric effect for water and tungsten for photons with energy of 1 keV to 10 MeV. The discontinuities in the cross-section of tungsten occur when the

energy of the incident photon equals the binding energy of K, L and M shell of tungsten. As the photon passes each of these energies the probability of interaction greatly increases[13].

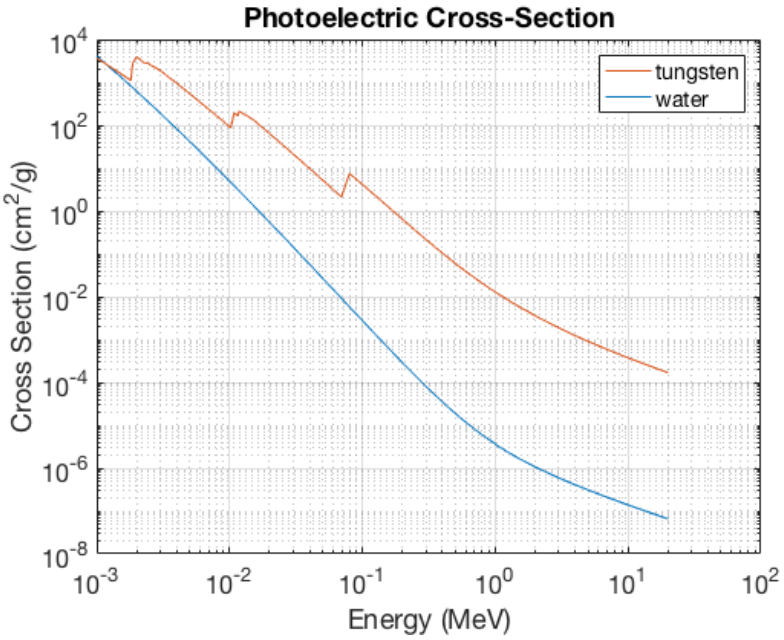

Figure 2.4 – Cross-section of the photoelectric effect in water and tungsten. Data taken from XCOM: Photon Cross-Sections Database.

2.4.3 Compton Scattering

An incident photon may interact with a free electron or an electron with binding energy much less than that of the incident photon through Compton scattering. In this process part of the photon's energy is transferred to the electron resulting in a scattered electron and photon. A higher energy incident photon on average transfers a higher fraction of its energy to the scattered electron. The cross-section of Compton scattering decreases with increasing photon energy and is nearly independent of atomic number[12,13]. Compton scattering is the most probable interaction of photons in soft tissues for photon energies relevant to radiotherapy, 100 keV – 10 MeV. Figure 2.5 shows the cross-section of Compton scattering for water and tungsten for photons with energy of 1 keV to 10 MeV.

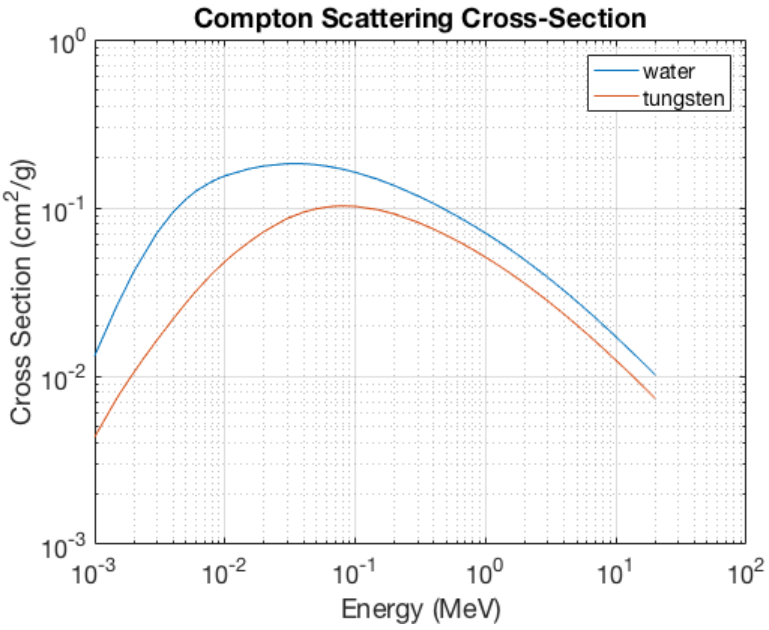

Figure 2.5 – Cross-section of Compton scattering in water and tungsten. Data taken from XCOM: Photon Cross-Sections Database.

2.4.4 Pair Production

A photon with energy greater than 1.022 MeV is able to interact with the electromagnetic field of an atomic nucleus and create a positron and electron pair. Since the rest energy of electrons and positrons is 0.511 MeV, any photon energy greater than 1.022 MeV appears as kinetic energy of the electron and positron. The energy distribution of the positron and electron varies depending on the energy of the incident photon. The electron and positron created in pair production undergo radiative or ionizational collisions. Near the end of the positron's path it will interact with a nearby free electron and the two will annihilate. This annihilation produces two photons each with 0.511 MeV of energy that are emitted in opposite directions in order to satisfy conservation of momentum[13]. Above the threshold energy of 1.022 MeV, the cross-section of pair production increases with both atomic number and photon energy. Figure 2.6 shows the cross-section of pair production for water and tungsten for photons with energy of 1 keV to 10 MeV.

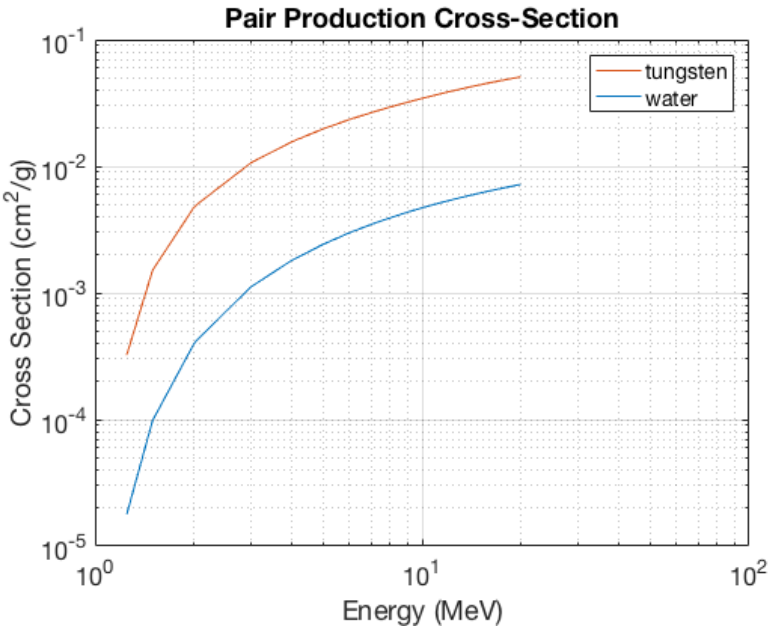

Figure 2.6 – Cross-section of pair production in water and tungsten. Data taken from XCOM: Photon Cross-Sections Database.

2.5 The Interaction of Electrons with Matter

As an energetic electron travels through a medium it will interact via radiative or ionizational interactions, which have been discussed previously. The majority of energy loss takes place through ionizational interactions in lower Z materials and at lower electron energies. The rate at which an electron loses kinetic energy per unit path length is known as the stopping power and is defined for both radiative (S_{rad}) and ionizational (S_{ion}) processes. The range of an electron can be determined by integration of the reciprocal of the total stopping power ($S_{tot} = S_{ion} + S_{rad}$)[12].

$$R = \int_0^{E_0} \frac{dE}{S_{tot}} \quad (3)$$

2.6 Dose Calculation

With information on the probability of photon interactions and the energy lost along an electron's path, the dose delivered by a photon beam can be calculated. As photons travel through a medium they are attenuated exponentially as they undergo interactions and transfer portions of their energy to the electrons of the medium. The number of photons N, which are transmitted through a medium of thickness x, is

$$N = N_0 e^{-\mu x} \quad (4)$$

where N_0, is the initial number of photons and μ, is the total attenuation coefficient. The total attenuation coefficient is determined from the sum of cross-sections of Rayleigh scattering, Compton scattering, the photoelectric effect and pair production. If, in addition to the number of photons that interact, we also have the mean energy absorbed by the medium per photon interaction, the energy absorbed in a medium of thickness x (assuming x is small) can be calculated as

$$D = \overline{E_{ab}} \mu n x \quad (5)$$

where $\overline{E_{ab}}$ is the average energy absorbed per photon interaction, n is the number of photons incident on the medium and $\mu n x$ is the number of photons interacting in the medium of thickness x[12]. The dose to the medium can then be calculated by dividing by the mass of the medium. Under the condition of charged particle equilibrium (where the energy of charged particles leaving a given volume is equal to the energy of charged particles entering the volume) it is more convenient to calculate dose at a point using

$$D = \psi \left(\frac{\mu}{\rho}\right) \overline{E_{ab}} \quad (6)$$

where ψ is the energy fluence at the point in question and ρ is the density of the medium[12].

Another common concept when discussing the interactions of radiation with matter is kerma. While dose is the amount of energy *absorbed* per unit mass, kerma represents the amount of kinetic energy *transferred* to a medium from photons to electrons. In which case we have the equation

$$K = \Psi \left(\frac{\mu}{\rho}\right) \overline{E_{tr}} \quad (7)$$

where $\overline{E_{tr}}$, is the mean energy transferred per photon interaction. This distinction is important because depending the energy of the photons and the material in question, the amount of energy absorbed per unit mass will differ from the amount of energy transferred to secondary electrons. For example, highly energetic electrons may have a range which takes them past the volume of medium in which we are calculating dose and thus all of the energy transferred to those electrons is not absorbed. Furthermore, secondary electrons may emit bremsstrahlung radiation which may not be absorbed locally. This second point raises the distinction between collisional and radiative kerma. Collisional kerma is the portion of total kerma which is transferred to the medium by secondary electrons through ionization and excitation whereas radiative kerma is the portion of total kerma which is converted into bremsstrahlung. A few useful relationships between these concepts are

$$K = K_{col} + K_{rad} \quad (8)$$

and

$$K_{col} = K(1 - g) \quad (9)$$

where K_{col} is collisional kerma, K_{rad} is radiative kerma and g is the fraction of energy lost to bremsstrahlung. Under certain conditions, such as negligible values of g and charged particle equilibrium, kerma is equivalent to dose.

2.7 Basic Treatment Planning Concepts

Two important concepts in RT necessary to the discussion in this dissertation are the planning target volume (PTV) and the cumulative dose volume histogram (DVH). The PTV defines the target volume in RT plans. The PTV is actually a nested structure and includes the clinical target volume (CTV) and the gross tumour volume (GTV). The GTV is the volume of the cancerous lesion visible on a diagnostic scan. The CTV includes the GTV plus a margin, which accounts for the presence of any microscopic cancer cells present. Lastly, the PTV includes the CTV and GTV with a margin to account for any error in patient setup or treatment delivery.

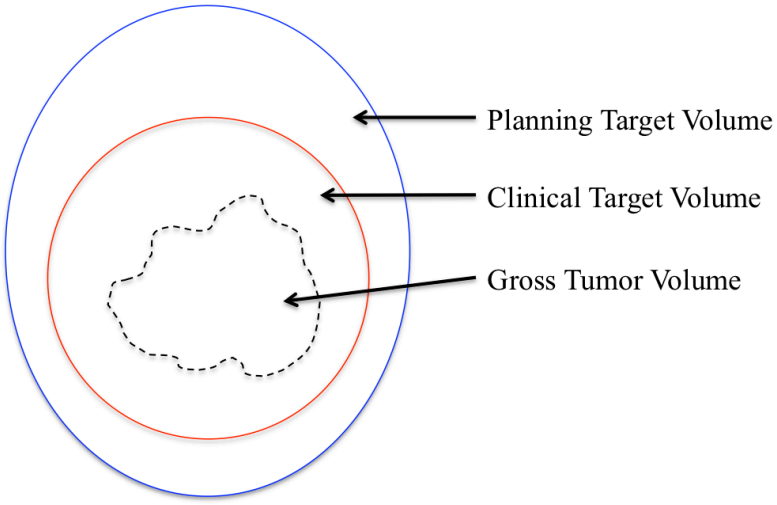

Figure 2.7 – Illustration of the relationship between the PTV, CTV and GTV.

2.7.1 Dose Volume Histograms

DVHs are frequently used to plan and evaluate RT treatments. DVHs graphically provide information on the dose delivered to percentage volumes of various structures in a RT therapy plan. DVHs are essential to the evaluation of radiotherapy treatments and, in conjunction with detailed dose constraint information (section 2.7.2), can be used to determine if a plan meets the

required dosimetric considerations to treat the tumor while minimizing the risk to healthy tissue and at-risk organs. Figure 2.8 is an example of a DVH for a lung treatment plan. As an example, in Figure 2.8 we see that the 100% of the PTV is receiving approximately 12.5 Gy in the KVAT treatment while 10% of the heart receives only 2.5 Gy. The ideal plan will deliver 100% of the prescribed dose to 100% of the PTV volume while minimizing the dose delivered to critical structures.

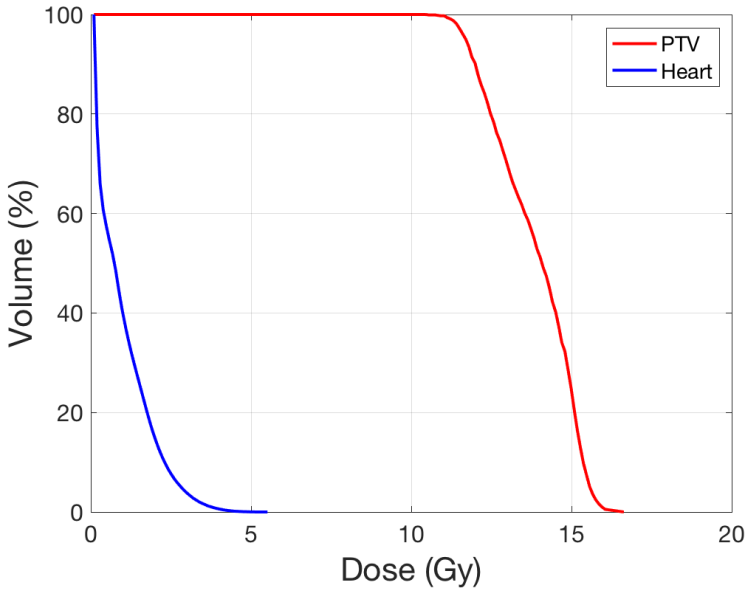

Figure 2.8 – Example of a DVH.

2.7.2 Dose Constraints

The amount of dose that an organ can receive depends on many factors such as the organ's importance, it's function, it's radiation resistance or sensitivity, the structure of the organ, and the type and energy of radiation being used for treatment and the number of fractions over which a patient receives treatment, to name a few. While each patient presents a unique set of circumstances under which a radiation treatment plan must be developed, there do exist protocols that outline general standards for common radiotherapy treatments. These protocols outline the dose that should be delivered to the tumor and the limits of dose that can be delivered

to organs-at-risk. For example, RTOG 0915 for stereotactic body radiation therapy of lung cancer stipulates a dose of 48 Gy delivered over 4 fractions to the PTV while no more than 1 cc of the ribs receives 32 Gy[15]. These documents created by the Radiation Therapy Oncology Group (RTOG) are written by experts in RT and are informed by expertise, radiobiology and data from clinical trials.

2.8 Comparison of Kilovoltage and Megavoltage Radiotherapy

Both kilovoltage and megavoltage photons are used in the clinic today for external beam radiotherapy. The applications for which they are used, however, are quite distinct. Kilovoltage photons are exclusively used for superficial tumours whereas megavoltage photons are the gold standard of treatment for the majority of cancers treated with external beam radiotherapy. There are three main differences between the use of kilovoltage vs megavoltage photons for external beam radiotherapy. The first is that lower energy photons are much more likely to interact via the photoelectric effect. In comparison, Compton interactions dominate in the megavoltage energy range. Secondly, megavoltage photons have superior penetration due to their higher energy. Lastly, while kilovoltage photons deliver their maximum dose at surface, megavoltage photons deliver their maximum dose at a depth that increases with photon energy. This difference can be visualized in the comparison of percentage depth dose (PDD) plots of kilovoltage and megavoltage photons (Figure 2.9).

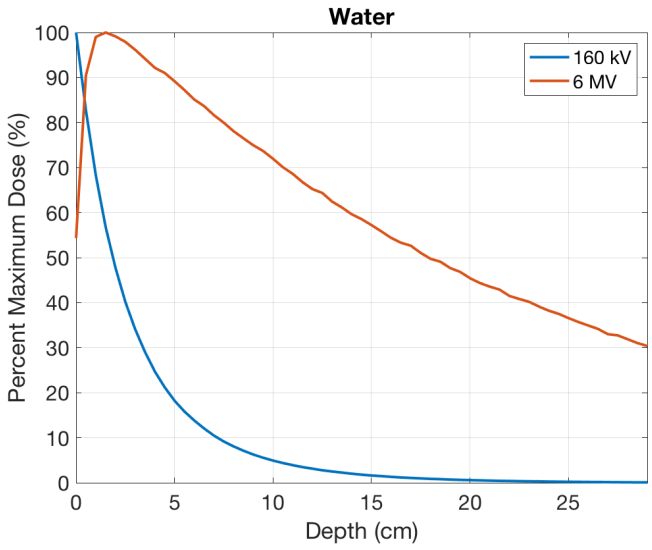

Figure 2.9 – Percent depth dose curve of a 6 MV and 160 kV photon beam in water.

The increasing trend of dose deposition starting at the surface and peaking at approximately 1.5 cm depth seen in the 6 MV photon curve is known as the build-up region. It is evident, however, that dose build-up is not present in the 160kV photon curve. This is due to the range of the secondary electrons created by photons. For lower, kilovoltage energies, secondary electrons have limited range and deposit most of their dose close to the site of interaction. However, the secondary electrons created by megavoltage photons are able to travel a fair distance from the site of interaction and deposit dose along their tracks, which terminate downstream. As the photon beams passes through a medium there will be a certain depth, which is dependent on the beam's energy, at which the energy carried away from the site of interaction by secondary-electrons will be equal to the energy deposited at the site of interaction by electrons originating upstream. This condition is known as charged particle equilibrium (CPE) and the maximum dose deposited by a megavoltage photon beam occur at the depth at which CPE has been established. Past this point the dose deposited by a megavoltage photon beam falls off as the primary beam is attenuated. The presence of build-up regions in megavoltage photon beams results in skin-

sparing characteristics in megavoltage external beam treatments and is of significant importance to the ability of these treatments to spare skin and healthy tissues.

2.9 Radiobiology

2.9.1 Biological Damage from Radiation

The primary method by which radiation results in cell death is through DNA damage. DNA damage is categorized as indirect or direct. Direct damage occurs when an energetic electron or photon ionizes an atom in the DNA resulting in damage. If this damage is repaired the cell will survive. If repair is unsuccessful the cell may die by a variety of mechanisms or remain senescent (inactive cellular division). Ultimately, the cell will not reproduce - the objective of RT. Indirect damage results in the same effect as direct damage but in these cases the energetic electron or photon ionizes cellular water. The ejection of an electron from water through ionization results in the production of highly reactive free radicals, which diffuse away from the site of ionization and may damage DNA[16].

2.9.2 Relative Biological Effect

Not all ionizing radiation deals damage to biological systems in the same way. For example, 1 Gy delivered by 6 MV photons will have significantly different biological results than 1 Gy delivered by 200 MeV protons. The difference in the damage dealt by different types of radiation is commonly quantified by the measure of relative biological effect (RBE) and is formulated as

$$RBE = \frac{D_{ref}}{D_{test}} \quad (10)$$

where D_{test} is the dose delivered by the test radiation that results in a specific level of biological damage and D_{ref} is the dose delivered by a reference radiation that results in the same level of biological damage[17]. The specified level of biological damage is usually quantified in terms of cell killing. To measure this one would irradiate cells at different levels of radiation and create a

cell survival curve and determine what amount of radiation from each source results in, for example, 50% cell survival or 50% cell killing. Typical reference radiation is either 250 kVp x-ray or Cobalt^{60} gamma rays. The RBE of a radiation type is fundamentally based on the nature of how that radiation deposits energy in the biological medium and is typically quantified in terms of the radiation's linear energy transfer (LET) in units of keV/μm [17]. LET is a means by which the density of ionization tracks created by ionizing radiation can be quantified. A higher density of ionization tracks typically results in a greater degree of biological damage and a higher RBE. It should also be stated that RBE depends on the quantity used to represent biological damage and several different measures have been used such as cell killing, double-strand breaks, neoplastic transformation and chromosomal aberration[18]. Furthermore, RBE may vary with the extent of which each measure is used. For example, the RBE determined using 50% cell kill may be different than the RBE determine using 20% cell kill. Conflicting information exists on the RBE of kilovoltage photons in comparison to megavoltage photons, which is of interest to this work. A report from the ICRP in 1990 states that the RBE is 1 for all x-rays and gamma rays whereas other information reports higher RBE's of kilovoltage photons in comparison to megavoltage photons[19,20].

3. Material and Methods

3.1 Monte Carlo Simulation of Radiation

Monte Carlo methods are computational algorithms that use successive sampling of (pseudo) random numbers for numerical calculations. There are many applications for MC methods one of which is for calculating the travel, interaction and dose deposition of radiation. There are a number of MC codes available for dose calculation purposes, some of which include VMC++[21], Geant[22], BEAMnrc/DOSXYZnrc[23,24], MCNP[25] and Penelope[26]. Each code differs in the particulars of the method by which they calculate the transport of radiation. BEAMnrc/DOSXYZnrc was chosen for this work because it has been validated for kilovoltage x-rays, which are the primary focus of the work presented here[27].

The physics of radiation transport is well described by photon attenuation cross-section, electron stopping power and electron interaction cross-section data. With the addition of the density and composition information of the medium through which radiation travels, both the location and type of interaction is known probabilistically. Random numbers can be sampled to determine what interactions occur and where they occur in the medium[28]. Photons and electrons are treated differently in MC codes due both to the different types as well as the different relative number of interactions they undergo as they traverse through a medium. Photons interact via Rayleigh, photoelectric, Compton and pair production processes and generally have few interactions separated by relatively large distances in comparison to electrons. On the other hand, electrons interact via elastic and inelastic collisions, the latter of which results in ionization or excitation of the medium, and numerous such interactions occur over short distances. As a result, photons are often simulated in an "analog" event-by-event manner whereas special techniques such as condensed history are used to make electron transport more efficient.

3.1.1 Photon Transport

Photon transport is essentially comprised of five steps, which are repeated in a step-by-step fashion during the MC simulation. First, a photon is sampled from the source distribution such as a point source, a pencil beam or a phase space file. Each sampled photon will have an energy, position, weight and angular direction. Second, the distance the photon travels, r, to the next interaction location is determined using a uniformly sampled random number between 0 and 1, denoted here as χ, and the linear attenuation coefficient of the material the photon is travelling through, μ, according to $r = -\frac{\ln(1-\chi)}{\mu}$. Third, the photon travels to the site of interaction using ray tracing. Fourth, the type of interaction at the interaction site is determined by sampling a random number from a probability distribution reflecting the probability of each interaction option as determined by cross-section data. Fifth and lastly, the interaction is simulated and the resulting energy and direction change is determined based on differential cross-section data of the given process.

3.1.2 Electron Transport

Electrons may also be simulated using a step-by-step process similar to photons. However, the number of electron interactions that each electron undergoes is so large that an analog simulation of all interactions along an electron's path would be extremely computationally intensive. To increase the efficiency of MC simulated electrons the condensed history method was developed by Berger. Using this technique, a large number of electron interactions are simulated in a small number of condensed steps. To preserve the accuracy of electron transport not all electron interactions should be condensed but only those that fall below a certain energy transfer threshold. Electron interactions that would create a bremsstrahlung photon or a secondary electron with energy larger than a set threshold are simulated in an analog manner.

3.1.3 Cutoff Factors

It is not efficient to compute the path of a photon or electron throughout its entire history. After a certain number of interactions, the energy of the photon or electron will be such that it is unlikely to travel past further than a certain distance. For example, if a photon or electron does not have the needed energy to transport energy a distance further than the voxelized dimensions of the simulation, then computation time can be save by simply depositing the remaining energy of the photon or electron locally. In MC simulations this energy cutoff is set by the ECUT and PCUT parameters. The incident energy of radiation and the properties of the medium should both be considered to set ECUT and PCUT as a poor choice of these settings will either result in inaccurate results or longer simulation times.

3.1.4 Structure of EGSnrc Simulations

MC simulations in the EGSnrc code system are separated into two parts one of which is simulated in BEAMnrc and the second of which is simulated in DOSXYZnrc. The first part of a simulation consists of defining the geometry of a radiation system and simulating the production of radiation from the system. System geometry in BEAMnrc is performed by defining a number of individual component modules (CM). Each CM has a particular geometry and serves a specific purpose. For example, one can define a rectangular slab of material of arbitrary thickness, a block of material with a number of customizable openings or an x-ray tube, to name just a few. By combining CMs most radiotherapy system geometries can be modeled. Once the system geometry has been defined a radiation source type is chosen to travel through the system. For linacs and x-ray tubes, an incident electron beam is simulated to strike a bremsstrahlung target to produce x-rays and the path of the created x-rays are simulated through the system and finally scored in a phase space file at the system's exit.

After BEAMnrc simulations a phase space file containing particles (generally photons and electrons) characteristic of the simulated system geometry is stored. This phase space file is then used as the input into the dose calculation simulation in DOSXYZnrc. There are two main ways of defining dose calculation geometry or phantom in DOSXYZnrc. One can either manually define the geometry and material of the phantom or a previously generated phantom file can be used. It is generally most useful to define a phantom independently of DOSXYZnrc as more complex geometries can be modeled. After phantom definition, the location of the phase space file or input radiation source can be specified and dose can be calculated in the phantom.

3.1.5 Material Specification

An important aspect of both BEAMnrc and DOSXYZnrc simulation is the specification of material properties since material information is crucial for the calculation of radiation transport and dose deposition. The EGSnrc code system comes with a default set of material data but the user can specify new materials according to the PEGS4 format which is detailed in the user manuals of EGSnrc[23,24]. Relevant information for the definition of PEGS4 data is elemental composition, material type, and density. Rayleigh scattering data is also not automatically included as it is only relevant for lower energy ranges. During a BEAMnrc or DOSXYZnrc simulation the PEGS4 program is run for each material present in the simulation. This program produces a set of necessary cross-section data using linear interpolation of the cross-section data contained in the PEGS4 file for each material. It is important that the cross-section data contained in the PEGS4 files corresponds to the energy range of photons and electrons in the MC simulation. An improper data energy range will result in inaccurate or failed simulations.

3.1.6 Uncertainty in Monte Carlo and Variance Reduction Techniques

An entire MC simulation consists of many histories of electrons and photons. As the number of histories increases the simulation's approximation of reality increases. In general, the

statistical error of MC methods decreases with $\sqrt{N}$, where N is the number of histories. One can imagine that MC simulations of sufficient levels of statistical uncertainty can require a large amount of computation time. To improve the efficiency of MC simulations various variance reduction techniques have been developed which, when properly implemented, greatly increase the efficiency of MC simulations with little impact on the simulation's reflection of realistic physics. A commonly used variance reduction technique is bremsstrahlung splitting. This technique greatly increases the speed with which a photon beam is generated via bremsstrahlung interactions in a high-Z target, such as the transmission target of a linac or the anode of an x-ray tube. When bremsstrahlung splitting is used, every time an electron creates a bremsstrahlung photon that photon is split into N photons with a weight of $1/N$, where N is the chosen splitting number. Bremsstahlung splitting may be either uniform or directional. In uniform splitting all bremsstrahlung events are split whereas in directional splitting only bremsstrahlung events that would result in a photon traveling in a defined direction are split. Directional splitting is more complex to use properly but improves simulation efficiency to a greater extent than uniform splitting.

3.2 Ionization Chamber Dosimetry

In order for both the experimentation and clinical application of radiotherapy to be successful, the dose delivered by a radiotherapy system needs to be measurable. A number of different tools exist for the purpose of quantifying radiation dose. One of the most common tools is the ionization chambers. Ionization chambers vary widely in design but are all used to measure exposure. Exposure is defined as

$$X = \frac{dQ}{dm} \quad (11)$$

where dQ is the absolute value of the total charge of ions created in air of mass dm once all energetic electrons put in motion by photons have come to a stop[13]. Exposure can be related to other quantities of interest in radiotherapy, such as air kerma, by

$$K_{air} = \mathrm{X}\left(\frac{W}{e}\right)_{air} \quad (12)$$

where $\left(\frac{W}{e}\right)_{air}$ is the average energy expended per unit charge of ionization created in dry air and has a value of $8.76\times10^{-2} Gy/R$ (R = units of Roentgen).

As a concrete ionization chamber example, consider a Farmer ionization chamber, which is a commonly used ionization chamber for clinical dosimetry of photons and electrons. Farmer chambers are composed of a cylindrical graphite chamber. Within the graphite walls is a central rod of aluminum, which serves as an electrode. Between the central cathode and chamber walls is air. When connected to an electrometer, a voltage potential is established between the central electrode and the chamber walls. As photons pass through the chamber, secondary electrons are produced in air and excite and ionize air molecules. The ions produced over the secondary electron tracks are accelerated by the chamber's potential and are collected and the total charge is read out by the electrometer.

The current standard for dosimetry of low to medium energy (40 – 300 kV) x-rays is the AAPM's Task Group 61 report[29]. This document outlines the recommended protocol for measuring the dose delivered by x-rays of up to 300 kV with the use of ionization chambers and phantoms. The protocol requires the user to have an ionization chamber and electrometer which have been calibrated by user's national standards laboratory. National standards labs possess the equipment and conditions necessary to deliver external beam radiation at a variety of energy levels with known levels of intensity. For x-rays of energy between 40 and 300 kV, ionization chambers are calibrated in terms of air-kerma. When a chamber and electrometer are sent for

calibration, a known amount of air-kerma is delivered to the ionization chamber which results in a measurement of charge on the electrometer. These two values are then used to calculate an air-kerma calibration factor for a given beam quality specified by HVL and tube potential which relates the amount of charge measured by the chamber and electrometer to the amount of air-kerma deposited in the chamber

$$N_K = \frac{K_{air}}{M} \quad (13)$$

where N_K is the air-kerma calibration factor in units of $\mathrm{Gy/C}$, K_{air} is air-kerma in units of Gy and M is the measured charge in units of C. It should be noted that the value M is not simply the raw reading of the electrometer but rather the corrected reading and accounts for factors which will affect the amount of charge collected such as ambient temperature and pressure, ion recombination effects, polarity effects and the accuracy of the electrometer (equation 14). The value of N_K is dependent on beam energy. Typically, a standards lab will calibrate the ion chamber and electrometer for a variety of beam qualities or the beam quality, which most closely matches the beam of the user's lab. Beam quality is typically defined in terms of both HVL and tube potential.

$$M = M_{raw} P_{TP} P_{ion} P_{pol} P_{elec} \quad (14)$$

Once a user receives their ionization chamber, electrometer and calibration factors from the standards laboratory, they are then able to irradiate the chamber with their own x-ray system and determine the absorbed dose in water at a depth of 2 cm according to

$$D_{w,z=2cm} = M N_K P_{Q,cham} P_{sheath} [(\overline{\mu_{en}}/\rho)^{w}_{air}]_{water} \quad (15)$$

where $D_{w,z=2cm}$ is the dose to water at a reference depth of 2 cm, $P_{Q,cham}$ is the chamber correction factor P_{sheath} is the correction factor to account for changes in photon absorption and scattering due to the water-proofing sheath and $[(\overline{\mu_{en}}/\rho)^{w}_{air}]_{water}$ is the water-to-air ratio of

mean mass energy absorption coefficients for the photon spectrum at the point of measurement in water in the absence of the chamber[29]. It should be mentioned that calculated values of absorbed dose to water can be made from measurements of air-kerma due to the low energy of the photons to which this protocol applies. These low photon energies ensure an almost negligible value of g and low ranges of secondary electrons to ensure the condition of charged particle equilibrium.

3.3 Film Dosimetry

The use of the TG 61 protocol allows one to make measurements of dose in water at a depth of 2 cm in one's own lab. Once the number of mAs (current-time product) or beam-on time needed to deliver a particular dose to water at a depth of 2 cm is known, this information can be used to accurately deliver variable amounts of dose to this reference depth of 2 cm. However, ionization chambers are only one-dimensional dosimeters since they only give the dose value at one particular point. If two dimensional dose maps are needed the use of an ionization chamber becomes inefficient. Furthermore, the spatial resolution of ion chambers may not be adequate for the task at hand. Radiochromic film is a staple tool in dosimetry and serves as an effective means of two dimensional dose measurements. The term *radiochromic* refers to the direct coloration of a material due to the interaction with ionizing radiation[30]. Radiochromic films vary in structure, thickness and composition but all consist of a polyester base, a radiosensitive layer and a transparent coating. Radiochromic films can also be made to closely approximate the radiological properties of materials of interest to simplify the measurement of absorbed dose to a particular material. Most radiochromic films, however, are approximately equivalent to water or muscle. Upon interaction with ionizing radiation, the radiosensitive layer undergoes a chemical change resulting in coloration proportional to the amount of dose delivered to the film. The coloration of the film requires no processing and is relatively stable 24 hours

after exposure[30]. A flatbed scanner can then read the film and measurements of optical density can be made. Optical density is defined as

$$OD = log \frac{I_0}{I_t} \quad (16)$$

where OD is optical density, I_0 is amount of light collected in the absence of the film and I_t is the amount of light transmitted through the film. Since the amount of coloration is proportional to the amount of dose delivered to the film, values of optical density can be related to dose after a calibration curve has been made. A calibration curve can be made by exposing separate pieces of film to various levels of known dose. The optical densities of each of these dose levels are then measured and plotted against dose. After this a film can be irradiated to unknown and non-uniform doses and readings of optical density can be used to determine two dimensional dose maps. Radiochromic films are energy dependent and therefore a separate calibration curve is required for beams of differing quality.

3.4 Inverse Planning and Optimization

In optimization a problem is posed to which there exists one or a number of best or optimal solutions. Solving this problem requires a method of evaluating the "cost" of any proposed solution. Cost is essentially a measure of whether a solution increases or decreases the quality of the overall solution. The main purpose of computer optimization is to iteratively search through a parameter space of possible solutions, evaluate their cost, and approach the solution that minimizes cost and is therefore optimal. In radiotherapy, the general problem is to deliver a prescribed dose to the PTV while sparing the surrounding healthy tissue as much as possible. The parameter space of solutions generally consists of possible treatment geometries, beam intensities, beam delivery time and beam modulation. This parameter space is decidedly more complex in VMAT than KVAT. In VMAT the beam is modulated dynamically by the

MLC as it rotates around the patient. As a result, the optimization algorithm must optimize the configuration of the MLC and the intensity of the treatment beam. In KVAT there are a discrete number of beamlets to choose from at each treatment angle. Additionally, the treatment time of each beam is variable. In both the VMAT and KVAT optimizations performed in this work the cost of any proposed solution to the problem is defined using dose volume histogram constraints on both the PTV and organs-at-risk (OAR). In the planning stages of the optimization procedure dose constraints on the PTV and each OAR are specified and given a weight dependent on the importance of the constraint. The optimization algorithm will then choose a solution from the parameter space, evaluate the choice, either accept or reject that solution choice and repeat until a suitably optimal solution is reached. This planning process in RT is termed "inverse" since we are first specifying the desired treatment and then using optimization to determine how it is achieved.

3.4.1 Column Generation

It should be stated that while the general formula for computer optimization is similar between different problems, the specifics by which the parameter space is searched depends on the optimization algorithm employed. In this project we have employed an optimization framework developed by collaborators at McGill university, which we will refer to as the McO. The McO uses the column generation method optimization algorithm. Unlike most other optimization algorithms, column generation divides the optimization problem into a master problem and a sub-problem. Initially, the sub-problem is optimized to determine a subset of solutions to the master problem containing "good" solutions[31,32]. This subset is then used to find an optimal solution to the master problem. More specifically, when determining an optimized RT plan the McO starts with an empty plan. The algorithm then determines the beamlet that delivers the highest dose to the PTV without regard for other dose constraints. This first solution is then

used to determine further ‘optimal’ solutions that decrease the cost function. Column generation is useful for problems that have a large parameter space since it does not search through the entire parameter space in each iteration of the master problem.

4. Monte Carlo Simulations of a Kilovoltage External Beam Radiotherapy System on Phantoms and Breast Patients

Published in Medical Physics 2017

Introductory Remarks

The purpose of this first work was to demonstrate a proof-of-principle example of the ability of a kilovoltage x-ray radiotherapy system to deliver radiation to a target volume at depth while achieving a skin-sparing effect. This was performed by simulating dose delivery from the KVAT system to cylindrical water phantoms containing a variety of spherical PTVs of various sizes and depths. Additionally, as a more realistic case, a partial breast irradiation was simulated using patient CT data.

4.1 Introduction

Radiotherapy (RT) is an essential tool in the treatment of cancer. It is estimated that 40% of patients that were cured of cancer have received radiation therapy as a stand-alone treatment or combined with other methods such as chemotherapy[33]. The standard of RT care is the delivery of high-energy (6 - 15 MV) photons, generated by a medical linear accelerator (linac), to the site of disease. Linacs utilize a number of expensive technologies, such as precisely machined waveguides and high voltage generators, to accelerate electrons to relativistic speeds. Upon collision with a tungsten target these electrons produce megavoltage (MV) bremsstrahlung photons, which are filtered, collimated and directed to the site of treatment. The high energy of these photons necessitates expensive treatment infrastructure known as "vaults" to house the linac in order to shield medical personnel from radiation. The result of this high cost is strain on healthcare systems. Bentzen *et al*. estimate that even developed countries are currently not meeting their demand for linacs[33]. For example, Great Britain was meeting only 50% of its radiotherapy needs as of 2004. In the same year, 11.4 million people were diagnosed with cancer worldwide and incidence has continued to rise. The World Health Organization estimates yearly global cancer incidence rates will rise to 16 million by 2020[34]. In the face of the rising incidence of cancer, the costs of treatment will increase the pressure on healthcare systems

already weighed down by high prices. This leads to the conclusion that a lower cost RT option is needed to supplement current RT technology.

In contrast to MV radiotherapy systems, lower energy kilovoltage (kV) photons can be generated with inexpensive x-ray tubes. MV photons are characterized by a build-up region of radiation dose, which allows the delivery of clinical doses to deep-seated lesions and reduces the dose delivered to skin. On the other hand, kV photons do not share this characteristic of build-up. As a result, treatment of a deep-seated tumor would deliver unacceptably high doses to the intervening tissues hit by a conventional kV beam en-route to the lesion.

Previously, Prionas *et al*. have investigated the feasibility of delivering kV photon radiotherapy on a specialized breast CT platform using Monte Carlo modeled arc therapy[35]. Our group has recently presented a design of a cost-effective 200 kV kilovoltage arc therapy (KVAT) x-ray source consisting of a large tungsten anode and a custom linear collimator, which collimates incident photons into a number of converging beamlets intersecting at the radiation isocenter[36]. By using converging beamlets of kV photons, the dose to healthy tissues above a deep-seated tumor is reduced by spreading the photons over a larger area. At the site of the tumor all of the beams converge and deliver dose higher than that delivered to the surrounding healthy tissue. We have previously shown that conformal dose delivery to a single 4-cm diameter target at a depth of 10 cm was achievable with the novel KVAT source. In addition, previous work by Bazalova-Carter et al. experimentally verified the output, compared to Monte Carlo simulations, of a kV therapy source which shares the same principle of multiple converging kV photon beams[37]. As it is common to perform computational modelling of novel techniques to determine their potential before prototyping, we have yet to perform experimental validation of our current system. This is however, an essential stage in the future of our KVAT system. In this work we extended our investigations employing Monte Carlo modeling KVAT treatments to a total of 24 deep-seated tumors of different sizes and depths in homogeneous phantoms as well as to KVAT treatments of two partial breast irradiation cases, for both 4-cm and 3-cm diameter lesions, as a follow-up to

our original study[36]. This work is intended to determine the optimal range of lesion sizes and depths treatable by our KVAT system.

4.2 Materials and Methods

4.2.1 KVAT Source Design

An illustration of the geometry of our treatment system, including gantry, source and couch, is shown in Figure 4.1. Our kV x-ray source for therapy was reworked from concepts used in kV x-ray imaging sources, in particular employing scanning electron beam methods to generate x-rays and distribute beams. Our source has been designed to deliver conformal arc therapy to spherical lesions of 1, 2, 3 and 4 cm in diameter at three different depths in cylindrical water phantoms of 16.2 cm and 32.2 cm in diameter. Additionally, the source was designed to deliver dose to a 4-cm and 3-cm breast tumor based on patient CT data in both the prone and supine position.

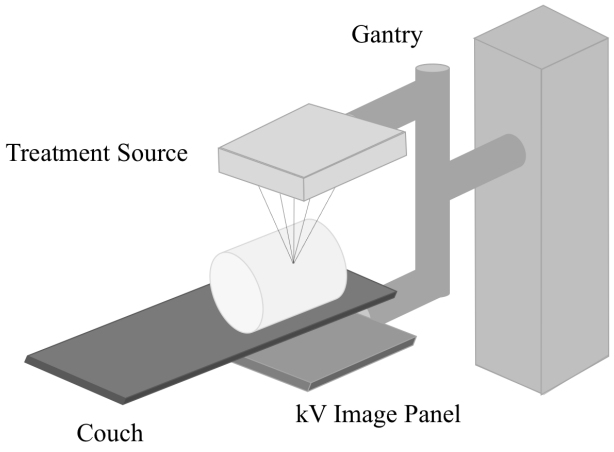

Figure 4.1 – Illustration of the KVAT system geometry including couch, gantry arm, treatment source and kV image detector panel.

Our KVAT source employed a 30 cm × 30 cm tungsten anode and a novel collimator consisting of nine converging holes in a linear array[36]. It should be noted that the 30 cm × 30 cm

anode was from a previous design and a much thinner anode, such as 30 cm × 1 cm, could be all that is required for the system. The beam filter is located directly above the beamlet holes of the collimator. Beamlet holes were spaced along a 30-cm length of the collimator. Additionally, in order to produce a sharp beam penumbra, the thickness of the collimator was 10 cm. The design of the KVAT source and the optimized collimator design parameters were recently presented by our group[36]. Our previous work optimized the source parameters (listed in Table 4.1) for the treatment of a 4-cm diameter lesion located at 10-cm depth in a 40-cm diameter phantom. With the exception of source extent, which was changed to 30 cm, and SAD, all parameters determined by the previous optimization were used in this study for treatments of various lesion sizes located at a number of depths in two different phantoms.

In the irradiation approach taken in this work, each tumor size requires an individual collimator to produce beamlets, which adequately cover the lesion. The collimator was designed such that the width of each beamlet at isocenter was equal to the width of the lesion. The source-to-surface distance (SSD) is defined as the distance from the bottom of the collimator to the surface of the patient or phantom. The source-to-axis (SAD) distance is then SAD = SSD + lesion depth and is fixed for phantom and patient studies to 38.1 cm and 34.4 cm, respectively. Three lesion depths were chosen for each lesion size in both phantoms (Table 4.2). The "deep" lesion was located at 8.1 cm and 16.1-cm for the 16.2 cm and 32.2-cm phantom, respectively. The "middle" lesion was located at 4.1 cm and 8.1 cm for the 16.2 cm and 32.2-cm phantom, respectively. Lastly, the center of the "superficial" lesion was located at a depth such that the distance between the surface of the phantom and the proximal portion of the lesion was 1 cm. Figure 4.2 illustrates the placement of each lesion inside the 32.2-cm phantom.

Table 4.1 – KVAT source design parameters for the phantom study.

Parameter	*Value*
Electron Beam Energy	200 keV
Anode Thickness	32 μm
Beam Filtration	0.4 mm Cu
Number of Collimator Holes	9
Source Extent	30 cm
Collimator Hole Size	0.5 mm
Collimator Thickness	10 cm
Source-to-Axis Distance	38.1 cm
Treatment Arc Angle	120 degrees

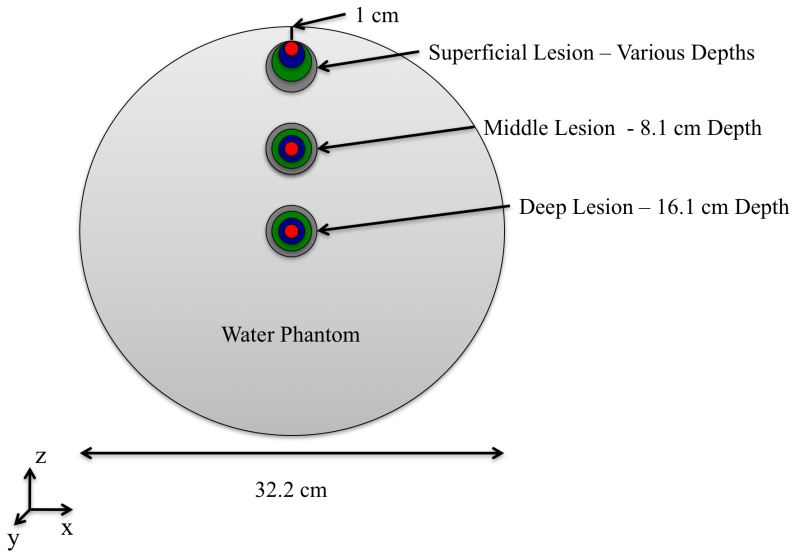

Figure 4.2 - Illustration of various lesion sizes (1 cm [red], 2 cm, [blue], 3 cm [green] and 4 cm [dark grey]) and positions in the 32.2-cm water phantom.

4.2.2 KVAT Source Simulation

Simulation of the KVAT x-ray source was performed using the BEAMnrc package of EGSnrc v2016[24,38]. The EGSnrc engine has been used and validated in previous published work[36,39]. Monoenergetic 200 keV electrons were used as the incident beam in all simulations. For each x-ray beamlet, a separate electron beam position on the anode was simulated using a pencil beam of 0.01-cm radius. The position of the electron beam on the anode was optimized for maximum x-ray fluence. The layers of tungsten (32 μm), niobium (20 μm), beryllium (5 mm), water (3 mm) and copper (filter, 0.4 mm) were modeled using the "SLABS" component module. The brass (C35300) collimator was split into five separate "BLOCK" component modules of 2 cm each. Nine 8-sided polygons were used to approximate circular cavities in the collimator for each collimator level. The diameter of each polygon measured on the proximal side of the collimator was 0.5 cm. The intersection of each x-ray beamlet produced by the collimator was set to the center of each lesion. Electron and photon cutoff energies were set at 0.521 keV (including 0.511-keV rest energy) and 0.01 keV, respectively. XCOM cross-section data was used for all simulations. Photons were scored directly after leaving the collimator as a phase space file for use in dose calculations in the DOSXYZnrc code[24]. We used variance reduction techniques to speed up the simulations. Bremsstrahlung cross-section enhancement with an enhancement factor of 1 and enhancement constant of 200 as well as uniform bremsstrahlung splitting with a splitting factor of 200 were used[39]. For both techniques, Russian roulette was turned on. Each phase space file contained a minimum of 10^5 photons.

4.2.3 Phantom Study

Monte Carlo KVAT dose delivery was simulated using the DOSXYZnrc code package of EGSnrc[24,38]. Dose was calculated for a total of 24 cases – four lesion sizes (4 cm, 3 cm, 2 cm and 1 cm) at each of three tumor positions (superficial, middle and deep) for two phantom sizes (16.2 cm and 32.2 cm). The calculated value of dose per particle was converted into cGy/min with a 200-mA tube current using a conversion factors of 8.86×10^{20} particles per 30 minutes irradiation at 200 mA and (1/30∗100 cGy/Gy)[36]. Additionally, for a reference, a 120-degree arc treatment,

delivered with 6-MV photons approximated by the Mohan6 spectrum[40] with a 2 cm × 2 cm field, was simulated for the 2-cm lesion located at the superficial depth of the 16.2-cm phantom.

Both phantoms were generated using MATLAB (The Mathworks, Nattick, MA) and followed the DOSXYZnrc format. Voxel size was set at 2 mm × 2 mm × 2 mm. The 16.2-cm phantom contained 81 × 81 × 81 voxels and the 32.2-cm phantom contained 161 × 161 × 161 voxels. The area surrounding cylindrical phantoms was set to air while the phantom itself was composed of water. The phase space files of the nine beamlets, from each of the 24 cases, were separately used as the source (ISOURCE = 8) in the DOSXYZnrc simulations. The SAD of all tumors was set to 38.1 cm with the SSD varying according to the depth and size of the lesion as well as the phantom size. Table 4.2 details the depths and SSDs of each lesion for both phantoms.

Table 4.2 – Lesion depths and for each lesion size in both the 16.2-cm and 32.2-cm phantom.

	Target Location	*1-cm Lesion Depth (cm)*	*2-cm Lesion Depth (cm)*	*3-cm Lesion Depth (cm)*	*4-cm Lesion Depth (cm)*
16.2-cm Phantom	Superficial	1.5	2.1	2.5	3.1
	Middle	4.1	4.1	4.1	4.1
	Deep	8.1	8.1	8.1	8.1
32.2-cm Phantom	Superficial	1.5	2.1	2.5	3.1
	Middle	8.1	8.1	8.1	8.1
	Deep	16.1	16.1	16.1	16.1

For the middle and superficial lesions, a 120-degree arc was used while a 360-degree arc was used for the deep lesions. For each simulation, beamlets were weighted according to their distance to the isocenter using the inverse square law and the 3ddose files were combined using MATLAB. With this weighting, beamlets with a further distance to travel to the lesion were weighted higher. All dose distributions were normalized to the dose delivered to 95% of the lesion volume to facilitate comparison.

For each of the 24 phantom dose distributions calculated, three metrics were determined using MATLAB: i) the *lesion-to-skin* ratio was calculated as the ratio of the D_{95} (the dose

delivered to 95% of the lesion volume) divided by the mean dose delivered to a 2.4 cm × 2.4 cm × 2 mm volume in the center of the beam at the surface of the patient where the highest skin dose is delivered; ii) the dose to a 0.8 cm × 0.8 cm × 0.8 cm volume at isocenter (referred to as "*isocenter dose*") representing the x-ray source output (cGy/min) for a 30-minute treatment, and iii) *dose homogeneity*, the ratio of the maximum dose and the minimum dose delivered to the lesion. A skin thickness of 2 mm was chosen to sample the dose delivered to the basal layer at 0.7 mm depth and the dermis at 1 mm depth[41]. Additionally, depth dose curves, lateral dose profiles and cumulative dose volume histograms (DVHs) were calculated for each of the 24 dose distributions generated.

4.2.4 Patient Study

Monte Carlo KVAT delivery was simulated for two breast patients treated with a hypothetical partial breast irradiation. In all cases dose to medium was calculated. One patient phantom was created using the CT data of a female patient in the supine position, and another one was created from CT data for a female patient in the prone position. KVAT was simulated for hypothetical lesions of 4 cm and 3 cm in diameter. The tumors were centrally located approximately 3 cm below the skin in the left breast. For reference, volumetric modulated arc therapy (VMAT) and 3D conformal radiation therapy (3D CRT) dose distributions using 6-MV photons were generated using the Eclipse™ treatment planning system (Varian Medical Systems, Palo Alto, CA) for the 4-cm and 3-cm lesions of the supine case. As our KVAT breast treatments are partial breast treatments, 3D CRT plans were chosen as a comparison due to their use in clinical trials for accelerated partial breast irradiation[42,43]. VMAT was also used for comparison as these dose distributions more closely resemble those produced by our KVAT system in terms of conformality. Dose calculation of VMAT and 3D CRT plans were performed using the VMC++[21] dose calculation package and a modelled Varian TruBeam™ linac. VMC++ was used for these calculations as part of previously existing in-house software[44]. All VMC++ calculated plans employed a voxel size of 2.5 mm × 2.5 mm × 2.5 mm and had an error of less than 1%. It is important to note that VMC++ and DOSXYZnrc have shown excellent agreement[45].

Supine patient CT data was converted into an EGSnrc phantom using RT_Image[46]. The original CT data was downsampled from a voxel size of 1.27 mm × 1.27 mm × 2.00 mm to 3.8 mm × 3.8 mm × 4.0 mm to reduce calculation time. Hounsfield units were converted to mass densities using a clinical calibration curve. Four ICRU materials were assigned to the phantom: air, inflated lung, skeletal muscle and ribs (2-6)[47]. The Hounsfield unit range corresponding to these materials was as follows: air (-1000:-850), lung (-850:-300), muscle (-300:100) and ribs (100:2000). We simulated the 120-degree KVAT with an SAD of 34.4 cm for each lesion size. In addition, treatments using larger arcs of up to 180-degrees, as well as increased filtration up to 4-mm Cu, were simulated in order to investigate methods to reduce rib dose. The VMAT plan was generated for a 180-degree arc with constraints maximizing lesion uniformity and minimizing body dose. 3D CRT plans consisted of four wedged, non-coplanar fields with multi-leaf collimators shaped to the PTV with a circular margin of 0.7 cm. RT_Image was used to calculate all dosimetry metrics in the patient studies.

Segmented prone breast image data acquired on the dedicated breast scanner at UC Davis[48] were converted to an EGSnrc phantom and downsampled from 0.5 mm × 0.5 mm × 0.5 mm to 2.0 mm × 2.0 mm × 2.25 mm voxels. The five materials in the image were set to adipose, glandular, partial glandular and skin ICRU materials, as well as air. All prone breast KVAT treatments used a 360-degree arc around the circumference of the breast with an SAD of 34.4 cm. Additionally, simulations of 360-degree, 6-MV linac treatment were calculated using the Mohan 6 spectrum in BEAMnrc for the 4- and 3-cm lesions.

4.2.5 Criteria for Evaluation of KVAT Plans

The metric of lesion-to-skin ratio was used as a measure of clinical acceptability. According to Lee et al., an orthovoltage (1 mm Cu half value layer) dose of 3000 cGy delivered in 200 cGy fractions with a 10 cm x 10 cm field results in an acute reaction of desquamation and moderate late changes to the skin[49]. It should be noted that given the variety of factors such as field size, energy and dose fractionation that affect acceptable maximum skin dose, it is difficult to state exact skin dose limits for our KVAT system without clinical data. In this work we accept

maximum mean skin dose of 250 cGy per fraction as a reasonable cutoff for clinical acceptability. It should be noted that the 200 kV KVAT system investigated here has a half value layer of 1.17 mm Cu when used with a 0.4 mm Cu filter and irradiates approximately 80 cm^2 of tissue in the 4 cm supine breast case with a 180-degree arc. Dose prescription and fractionation require careful consideration of clinical data as well. We chose to follow the fractionation scheme of 3850 cGy delivered over 10 fractions to D_{95} as used by NSABP-B39/RTOG 0413 for partial breast irradiation[43]. With this dose prescription the minimum lesion-to-skin ratio to be deemed clinically viable was 1.5.

To evaluate the breast dose distributions, lesion-to-skin ratio and lesion dose homogeneity were calculated. To assess the elevated dose to bone from the KVAT source for the supine case, the ratio of D_{95} to the mean dose delivered to the rib located most centrally in the beam was calculated. In addition, DVHs of the lesion, the heart, and the ipsilateral lung, as well as mean body doses, were compared for the 4-cm KVAT, VMAT and 3D CRT supine cases. All breast dose distributions were normalized to D_{95}, the dose delivered to 95% of the volume of the lesion.

4.3 Results

4.3.1 Phantom Study

Dosimetric data for the 2-cm diameter lesion in the 16.2-cm phantom are displayed in Figures 4.3, 4.4 and 4.5 for the deep, middle and superficial lesion locations, respectively. Axial, sagittal and coronal dose distributions, depth-dose curves, dose profiles in the *x* and *y* directions, and cumulative lesion DVHs are included in these figures.

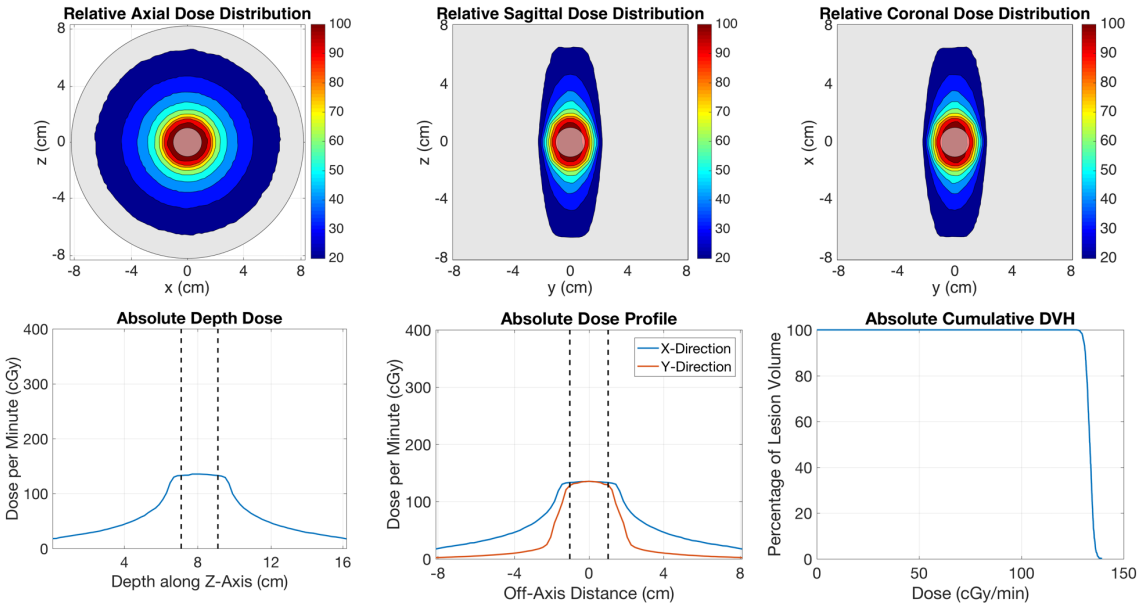

Figure 4.3 – Dosimetry from the 16.2-cm phantom – deep 2-cm lesion. Top row, left to right: axial, sagittal and coronal dose distributions for a *360–degree arc* treating the deep, 2-cm lesion at a depth of 8.1 cm with KVAT. Bottom row, left to right: depth dose curve, dose profiles and lesion DVH. The dashed lines in the depth dose curve and dose profiles represent the edges of the lesion.

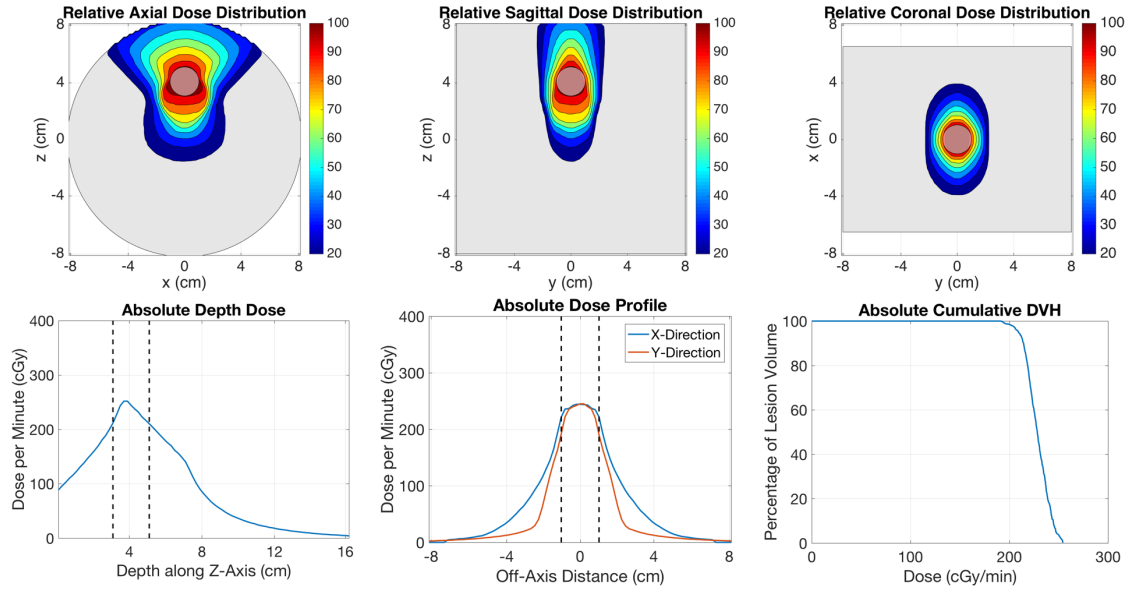

Figure 4.4 – Dosimetry from the 16.2-cm phantom – middle 2-cm lesion. Top row, left to right: axial, sagittal and coronal dose distributions for a *120–degree arc* treating the middle 2-cm lesion at a depth of 4.1 cm with KVAT. Bottom row, left to right: depth dose curve, dose profiles and cumulative lesion DVH.

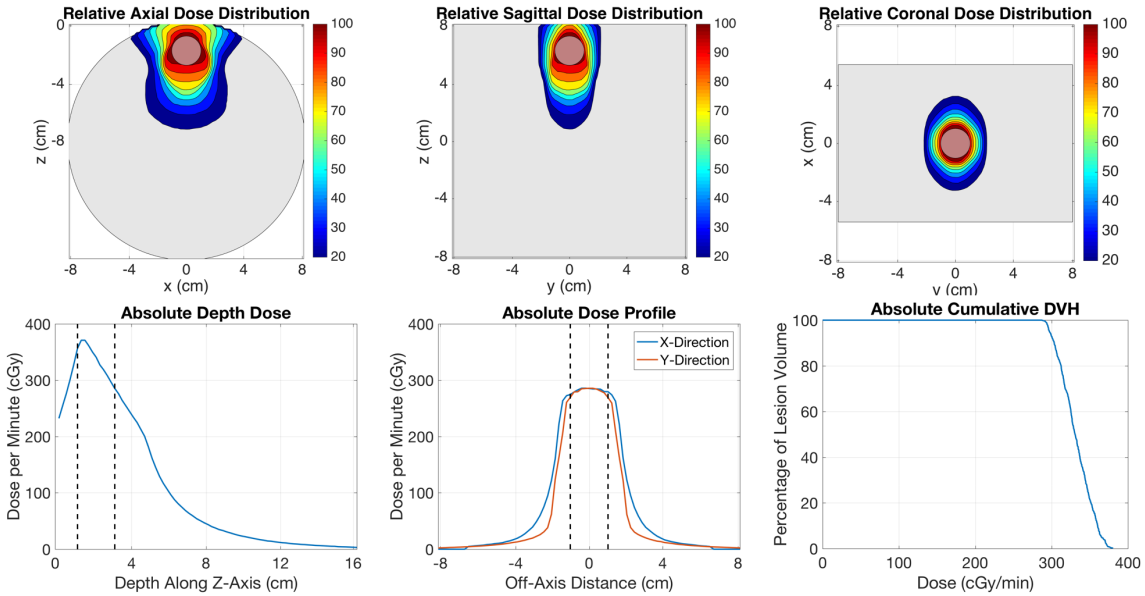

Figure 4.5 - Dosimetry from the 16.2-cm phantom – superficial 2-cm lesion. Top row, left to right: axial, sagittal and coronal dose distributions for a *120–degree arc* treating the superficial 2-cm lesion at a depth of 2.1 cm with KVAT. Bottom row, left to right: depth dose curve, dose profiles and lesion DVH.

The calculated values of lesion-to-skin ratio, isocenter dose and dose homogeneity for 1-cm, 2-cm, 3-cm and 4-cm lesions in each of the three positions for the 16.2-cm and 32.2-cm phantom are displayed in Figure 4.6a and Figure 4.6b, respectively.

a) 16.2-cm Cylinder Phantom

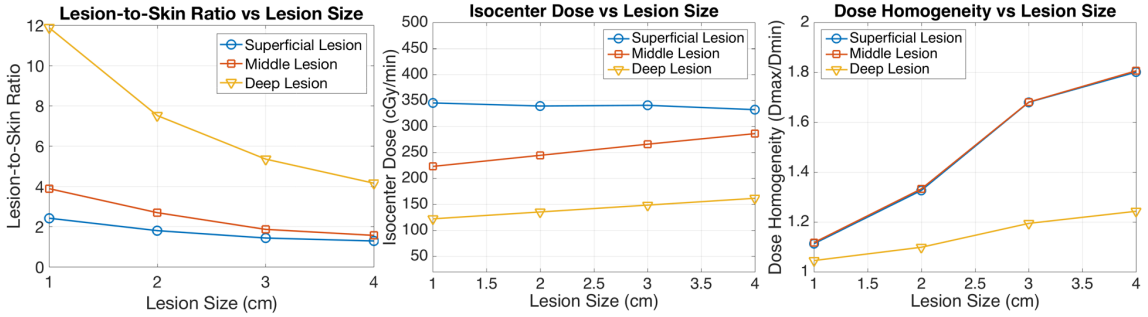

b) 32.2-cm Cylinder Phantom

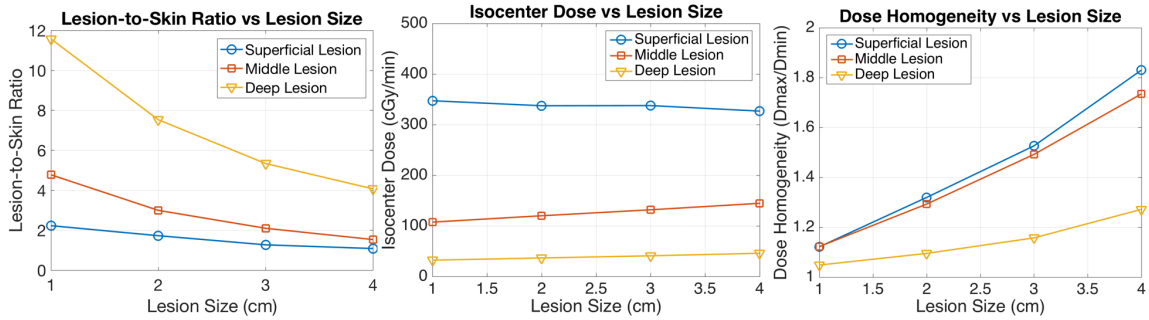

Figure 4.6 – Left to right: lesion-to-skin ratio, isocenter dose, and dose homogeneity as a function of tumor size for the 16.2-cm phantom (a) and the 32.2-cm phantom (b).

The highest lesion-to-skin ratio was calculated to be 11.9 for the 1-cm deep lesion in the center of the 16.2-cm phantom, while the lowest lesion-to-skin ratio was calculated to be 1.9 for the 4-cm superficial lesion in the 32.2-cm phantom. The highest dose to isocenter was calculated to be 345.2 cGy/min for the 1-cm superficial lesion of the 16.2-cm phantom, while the lowest dose to isocenter was found to be 32.3 cGy/min for the 1-cm deep lesion of the 32.2-cm phantom. The most homogenous dose distribution, with a homogeneity index of 1.05, was found for the 1-cm central lesion of the 16.2-cm phantom, while the least homogenous dose distribution, with a homogeneity index of 1.83, was found for the 4-cm superficial lesion of the 32.2-cm phantom. Lastly, the mean integral dose delivered to the entire phantom for each case is listed in Table 4.3. For reference to standard clinical dose distributions Figure 4.7a presents axial, sagittal and coronal dose distributions for the 2-cm superficial lesion irradiated 6-MV photons. Figure 4.7b illustrates the relative cumulative DVH of the 2-cm superficial lesion irradiated 6-MV photons and KVAT.

Table 4.3 – Mean integral dose delivered to the entire phantom (normalized to D_{95}).

	Target Location	*Mean Integral Dose 1-cm Lesion (%)*	*Mean Integral Dose 2-cm Lesion (%)*	*Mean Integral Dose 3-cm Lesion (%)*	*Mean Integral Dose 4-cm Lesion (%)*
16.2-cm Phantom	Superficial	2.1	4.0	6.7	10.3
	Middle	3.4	5.9	8.8	12.4
	Deep	6.1	9.5	13.8	18.2
32.2-cm Phantom	Superficial	0.4	0.8	1.3	2.1
	Middle	1.4	2.3	3.6	4.9
	Deep	4.6	7.1	9.9	13.0

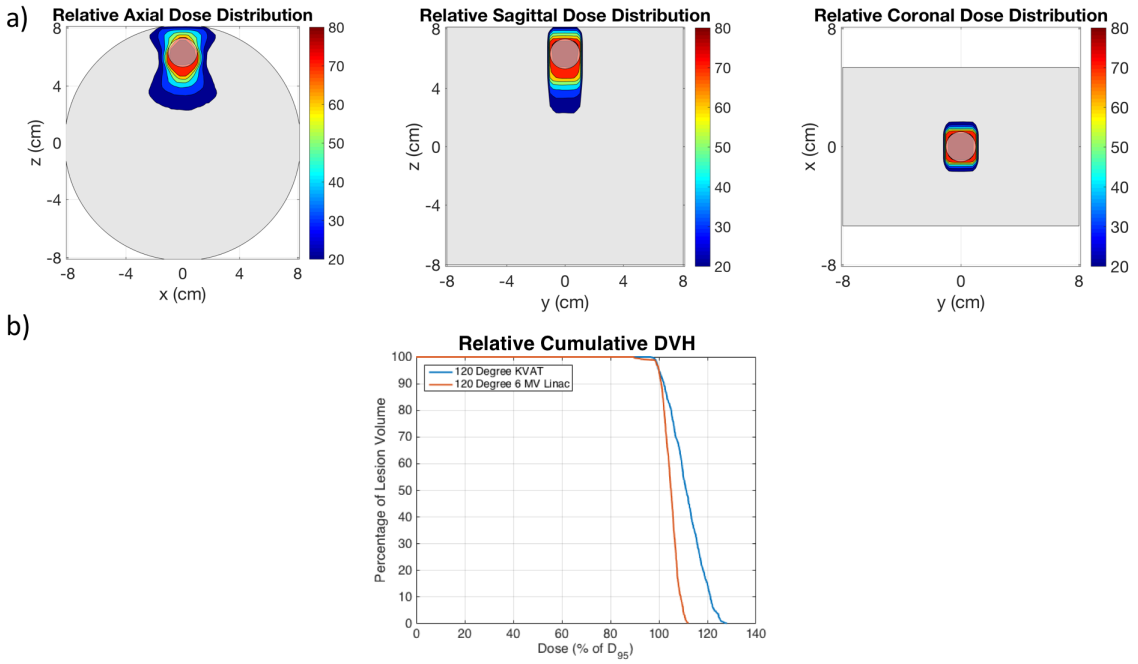

Figure 4.7 – Dosimetry from the 16.2-cm phantom – superficial 2-cm lesion. a) Left to right: axial, sagittal and coronal dose distributions for a *120–degree arc* treating the superficial 2-cm lesion at a depth of 2.1 cm with 6 MV photons. b) Cumulative DVH (normalized to D_{95}) for the 2-cm diameter lesion at the superficial position in the 16.2-cm phantom irradiated with KVAT vs. 6-MV photons in a *120-degree* arc.

The lesion-to-skin ratio of the 6-MV photon dose distribution for the 2-cm diameter superficial lesion in the 16.2-cm phantom was calculated to be 5.2 with a homogeneity value of 1.25. The KVAT dose distribution yielded a lesion-to-skin ratio of 1.8 and a homogeneity value of 1.33. The mean integral dose to the entire phantom volume was 1.9 % of D_{95} for the 6 MV plan and 4.0 % for the KVAT plan.

4.3.2 Patient Study

Figure 4.8 shows the axial, sagittal and coronal dose distributions of the 4-cm supine case treated with 180-degree KVAT, 3D-CRT and 180-degree VMAT. From the axial view it can be seen that the 10% isodose lines of KVAT and VMAT are similar. The 50% isodose line of the VMAT plan is slightly tighter than KVAT. It can also be seen that KVAT is more conformal than 3D CRT in which the 90% and 50% isodose line covers a larger volume of healthy breast tissue surrounding the lesion. Due to the KVAT source geometry using non-coplanar beams, the dose spread in the *z*-axis is wider compared to the VMAT plan and similar to the 3D CRT plan. It is worthwhile to note that while the 3D CRT plan irradiates the whole breast to much higher levels, the heart, lung and ribs are spared significantly in comparison to both VMAT and KVAT.

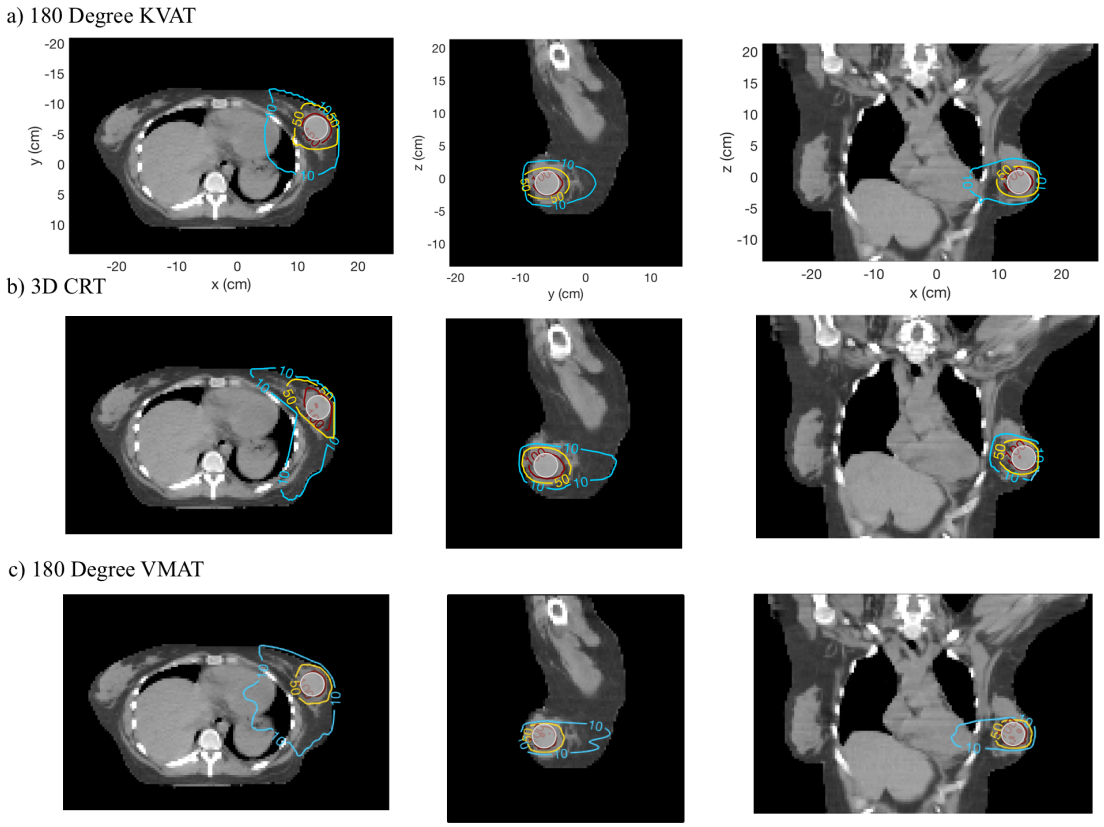

Figure 4.8 – Axial, sagittal and coronal dose distributions for the 4-cm supine breast case treated with a) 180-degree KVAT (0.5 mm Cu filter), b) 3D CRT and 180-degree 6-MV VMAT. The approximate size of the lesion is outlined by the grey circle.

Figure 4.9 contains the DVHs of the lesion, heart and the ipsilateral left lung for the 180-degree KVAT, 3D CRT and 180-degree VMAT dose distributions. Table 4.4 lists the calculated values of lesion-to-skin ratio, dose homogeneity and rib-to-lesion ratio for the 4-cm and 3-cm lesions for 120-degree and 180-degree KVAT, 180-degree VMAT and 3D CRT cases. The mean body dose as a percentage of D_{95} was calculated as 1.6%, 1.4% and 2.0% for the VMAT, 3D CRT and KVAT plan, respectively.

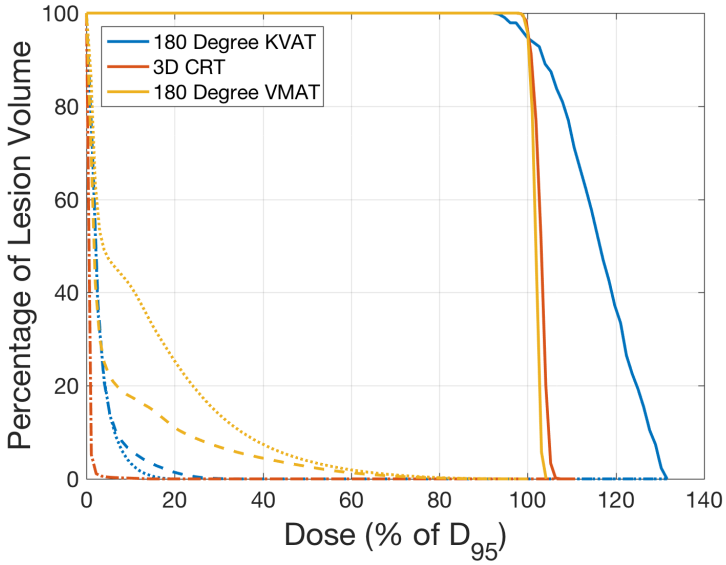

Figure 4.9 - Cumulative DVH (normalized to D_{95}) for the 4-cm lesion treated with 180-degree KVAT, 3D CRT and 180-degree VMAT represented by the blue, orange and yellow lines, respectively. Solid lines, dashed lines and dotted lines represent the lesion, left lung and heart, respectively.

Table 4.4 – Calculated values of lesion-to-skin ratio, dose homogeneity and lesion-to-rib ratio for the 4-cm and 3-cm KVAT, VMAT and 3D CRT supine breast cases.

Case	*Lesion-to-Skin Ratio*	*Homogeneity*	*Lesion-to-Rib Ratio*
4 cm 120 Degree KVAT	1.1	1.64	1.3
4 cm 180 Degree KVAT	1.4	1.67	1.5
4 cm 180 Degree VMAT	3.1	1.09	3.2
4 cm 3D CRT	2.8	1.08	30.1
3 cm 120 Degree KVAT	1.5	1.44	1.7
3 cm 180 Degree KVAT	1.9	1.44	1.8
3 cm 180 Degree VMAT	5.3	1.14	5.1
3 cm 3D CRT	3.5	1.09	68.0

Lesion-to-skin ratio was highest with a value of 5.3 for the 3-cm VMAT plan while the 3-cm 180-degree KVAT plan yielded a lesion-to-skin ratio of 1.9. For the 4-cm case the highest lesion-to-skin ratio was 3.1 for the VMAT plan. The lowest value was 1.1 from the 120-degree KVAT treatment but was improved with increased filtration and arc angle and was calculated to

be 1.4 for the 180-degree KVAT plan with 4-mm Cu filtration. This trend followed for the lesion-to-rib ratio with the highest 3-cm lesion value being calculated as 5.4 for the VMAT plan, while the KVAT plan having a lower value of 2.0. In terms of homogeneity, thanks to the Eclipse plan optimization the most uniform dose distributions were generated by VMAT, with values of 1.14 for the 3-cm lesion and 1.09 for the 4-cm lesion. For KVAT the best homogeneity value of 1.44 was found for the 120-degree treatment of the 3-cm lesion followed by the 120-degree treatment for the 4-cm lesion with a homogeneity index of 1.64. The 180-degree KVAT treatment of the 4-cm lesion was the least homogenous with a calculated homogeneity index of 1.67. Both 3D CRT plans had extremely high lesion-to-rib ratios due to the largely tangential direction of the beams used.

Figure 4.10 illustrates the prone breast cases with the 4-cm and 3-cm lesions treated with KVAT, and Table 4.5 compares relevant dose metrics between the prone and supine cases of KVAT.

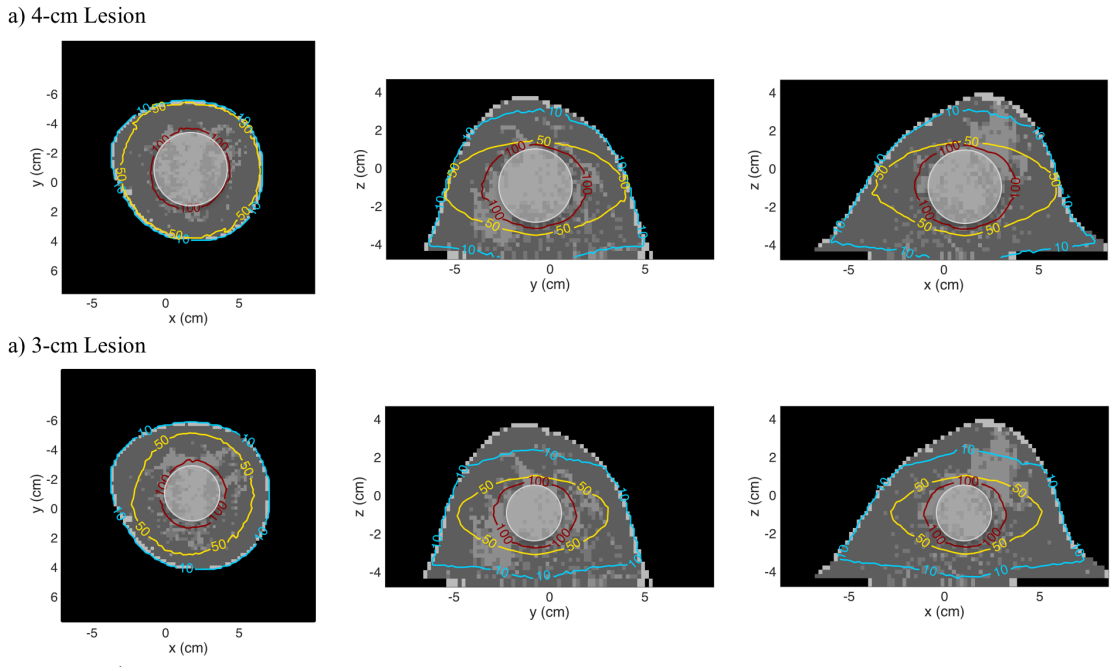

Figure 4.10 – Axial, sagittal and coronal dose distributions for the prone breast 360-degree KVAT treatment of the 4-cm lesion (a) and the 3-cm lesion (b). The approximate size of the lesion is outlined by the grey circle.

Table 4.5 – Calculated values of lesion-to-skin ratio and dose homogeneity for the 4-cm and 3-cm lesions in the prone breast patient treated with KVAT and un-optimized 6-MV linac photons.

Case	*Lesion-to-Skin Ratio*	*Homogeneity*
4 cm KVAT	2.3	1.43
4 cm 6 MV Linac	5.2	1.29
3 cm KVAT	3.3	1.31
3 cm 6 MV Linac	6.9	1.31

Lesion-to-skin ratio was calculated to be 3.3 and 2.3 for the 3-cm and 4-cm prone breast KVAT treatment, respectively. For the 6-MV linac simulations the lesion-to-skin ratio was higher and calculated to be 6.9 and 5.2 for the 3-cm and 4-cm lesion, respectively. The homogeneity index was found to be 1.31 for the 3-cm lesion prone breast KVAT treatment and 1.43 for the 4-cm lesion prone breast KVAT treatment. For the 6-MV linac simulations the homogeneity value was slightly better and calculated as 1.29 and 1.31 for the 4-cm and 3-cm lesion, respectively.

4.4 Discussion

4.4.1 Evaluation of KVAT Plans

Of the criteria chosen to evaluate KVAT plans, the metric of lesion-to-skin ratio was used to determine clinical acceptability. This choice is in part due to the higher attenuation of lower energy photons in superficial tissue which typically renders the use of kV photons unacceptable for the treatment of deep-seated lesions. Other considerations include the difficulty in using either dose rate or homogeneity as a strict method of determining clinical viability. Isocenter dose values calculated for phantom and patient studies serve as a useful indication of potential KVAT treatment times but these are also affected by field modulation and fractionation. Typical clinical treatments with MV photons use dose rates of 100-600 cGy/min. However, intensity modulated radiation therapy (IMRT) may be delivered at lower dose rates due to extreme modulation of the beam. In addition, treatment times increase in hypofractionated treatments. Given the variety of factors that affect dose rate and treatment time it is difficult to state a minimum acceptable dose rate for our KVAT system. Despite this difficulty, the dose rate of 100 cGy/min commonly used in the past serves as a useful reference.

The metric of homogeneity cannot serve as a strict measure of clinical acceptability. While it is widely held that intratumor dose homogeneity is dosimetrically favorable, historical clinical evidence suggests that a more peaked dose distribution within the tumor may be more effective[50]. In addition, less homogenous dose distributions are characteristic of gamma knife treatments of small lesions[51]. Therefore, despite the importance of knowing what the homogeneity of the lesion dose is, we do not hold it as a metric capable of indicating a plan's clinical viability when considered in isolation.

In addition to skin dose, it is important to be aware of the dose to ribs since the 200 kV beam will deliver more dose to boney anatomy relative to a higher energy MV beam. For supine breast irradiation, the dose to ribs should be limited to avoid rib fracture and pain. RTOG 0413 does not state any guidelines for maximum rib dose. However, a study by Aoki et al., observed no radiation induced rib fractures after stereotactic body radiotherapy when the maximum dose

delivered to the ribs was less than 5360 cGy delivered with a prescription dose of 600 cGy per fraction over a total of 9 fractions[52]. Given our prescription of 3850 cGy delivered over 10 fractions, the risk of rib fracture is likely to be minimal in our supine breast KVAT plans in which the maximum isodose lines present in the ribs is 50% corresponding to a dose of 1925 cGy.

4.4.2 Phantom Study

A number of trends can be seen in the metrics calculated from the phantom plans. Isocenter dose decreased as lesion depth increased due to the added attenuation of the beamlets. Given the decrease in dose rate below 100 cGy/min for deep lesions in the 32.2-cm phantom, treatment of lesions at depths of 16.1 cm will be less clinically practical. Values of isocenter dose did not change significantly with changing lesion size. Lesion-to-skin ratio decreased at shallower depths as the higher doses surrounding the lesion moved closer to the skin. With respect to lesion size, lesion-to-skin ratio increased and dose became more homogenous with a reduction in lesion size. The values of lesion-to-skin are fairly consistent for the deep lesions in both the 16.2-cm and 32.2-cm phantoms. This is the result of the beamlets in the 32.2-cm case being spread out over a larger surface area upon entrance of the phantom in comparison with the 16.2-cm case due to skin beam divergence which results in a lower mean skin dose. Based on our guideline of a minimum acceptable lesion-to-skin ratio of 1.5 we see that all phantom lesion cases with the exception of the 4-cm and 3-cm superficial lesions. The 4-cm middle lesion in the 32.2-cm phantom and the 16.2-cm phantom are very near the acceptable skin dose limit with a lesion-to-skin ratio of 1.5 and 1.6, respectively. Dose becomes less homogenous as lesion depth was reduced, a consequence of the 120-degree rotation being unable to provide the same coverage of the lesion. Examination of the DVHs (Figures 4.3-4.5) show that the most uniform dose coverage was achieved with a centrally positioned, smaller lesion. As the size of the lesion increased and its position moved closer to the skin, dose homogeneity decreased. It should be noted, however, that the difference between the middle and superficial lesions was not significant in terms of lesion dose homogeneity as can be seen in Figure 4.6. The 6-MV arc

treatment produced more homogenous coverage of the lesion with a high lesion-to-skin ratio of 5.2 (Figure 4.7). In comparison, while the KVAT treatment was less homogenous and had a lower lesion-to-skin ratio of 1.8, it nonetheless was a good result for the much lower photon beam energy.

4.4.3 Patient Study

From Table 4.4, it can be seen that increasing the arc angle of the KVAT improved both lesion-to-skin ratio and lesion-to-rib ratio. These advantages derived from the same number of photons being spread over a larger area of skin and more photons travelling at larger angles off the ribs (similar to a tangential beam). The added filtration used in the 180-degree KVAT case also reduced dose to both skin and ribs due to higher mean beam energy. Despite the improvements to lesion-to-skin ratio upon increasing arc angle, we see that only the 3-cm 180 degree KVAT plan satisfies our constraint on skin dose with a lesion-to-skin value of 1.91. Whereas, the 3-cm 120-degree plan and 4-cm 180-degree plans come close with values of 1.5 and 1.4, respectively. It is worthwhile to note that the lesion-to-skin ratios determined in the phantom and patient cases are consistent. Decreasing the lesion size of KVAT increased lesion-to-skin and lesion-to-rib ratios as well as producing smaller homogeneity indices. A smaller lesion could be covered more easily, which increases lesion homogeneity. Furthermore, a smaller lesion has less volume near the ribs and skin and results in lower doses to both.

Figure 4.8 demonstrates that in comparison to both KVAT and VMAT, 3D CRT is less conformal to the lesion volume. This indicates that a technique such as VMAT is a more appropriate comparison for KVAT than 3D CRT even though VMAT is not typically used for partial breast irradiation. In addition, 3D CRT delivers higher dose to the surrounding healthy breast tissue. Due to the tangential direction of the beams, however, the benefit of 3D CRT is less dose delivered to the ipsilateral lung, heart and ribs.

Calculated values for the VMAT plans have higher lesion-to-skin ratios and lower homogeneity values and serve as a useful reference for our external beam KVAT source for the supine breast cases. Similarly, 360-degree 6-MV linac plans yield higher lesion-to-skin ratios

and lower homogeneity values than 360-degree KVAT plans for both the 4- and 3-cm prone breast lesion cases.

It is important to note that all KVAT simulations have yet to be optimized. It is our intention to use inverse optimization to decide on appropriate beamlet weighting. Additionally, our optimization work will include an increased number of beamlets to allow for even greater flexibility of treatment delivery. However, performing this inverse optimization is not trivial and is the subject of future work. We anticipate that optimization of delivered beamlets will improve dose conformality and greatly reduce dose to organs at risk. Figure 4.9 shows an ideal lesion DVH for the VMAT supine breast case plan as well as reduced volumes of the lung receiving low dose in comparison to the KVAT plans. However, the VMAT plan delivers a higher dose to the heart than the KVAT plan, likely due to the higher energy photons and their deeper penetration. Additionally, it can be seen that 3D CRT delivers far less dose to the heart, ipsilateral lung and ribs. With respect to the prone breast cases, a smaller lesion results in a higher lesion-to-skin ratio and increased dose homogeneity for the same reasons as discussed above. Furthermore, a comparison between the 4-cm lesion prone and supine cases shows improvement to lesion-to-skin ratio and increased homogeneity for the prone orientation. This is the result of the 360-degree arc, which is made possible by the prone orientation and allows for more uniform coverage of the lesion while also spreading the dose to healthy breast tissues over a wider volume while maintaining the dose to the lesion. The same holds for the 3-cm lesion prone vs. supine case. While lesion-to-rib ratios cannot be evaluated for the prone treatments, it is expected that dose to the ribs would be minimal as the lesion would move further away from the ribs due to the effects of gravity. However, the effects of gravity may also result in more of the heart and lungs being exposed to the radiation field. This effect of gravity, along with other benefits of prone patient positioning, have been demonstrated by Fahimian *et al*. in their work investigating prone accelerated partial breast irradiation[53].

4.5 Conclusions

In this work, we have presented a Monte Carlo model of a novel arcing kilovoltage x-ray radiotherapy system and demonstrated its capabilities in the treatment of a variety of phantom cases and two breast cases. The system is capable of using photons generated from a scanning beam 200-kV x-ray source to deliver up to 345 cGy/min to a 1-cm superficial lesion, generating clinically acceptable dose distributions with lesion dose volume histograms similar to those generated by the Gamma Knife system. While dose to bone increases with the lower energy photons, the rib doses delivered in these supine breast KVAT plans does not threaten complications of rib fracture or chest wall pain. However, limitations on acceptable skin dose restricts the size of treatable lesions in the supine breast case to 3-cm. This work supports the feasibility of a low-cost kilovoltage radiotherapy system and has determined that the KVAT system is best suited to the treatment of smaller lesions of 1 – 2 cm in diameter at depths down to 8.1 cm and moderate lesions of 3-cm diameter with larger arc angles at depths ranging from 3 cm to 8.1 cm. Larger lesions of 4-cm diameter are expected to be treatable at depths of at least 4.1 cm (in a 16.2-cm phantom) and 8.1 cm (in a 32.2-cm phantom). For lesions of 1 – 4 cm in diameter treatment depths of up to 16.1 cm are possible at the cost of decreased dose rate. Future research will focus on optimization of KVAT treatment plans in order to evaluate additional clinical benefits.

5. Inverse Optimization of Low-Cost Kilovoltage Arc Therapy Plans for Breast, Lung and Prostate Patients

Published in Medical Physics 2018

Introductory Remarks

While the first paper was able to demonstrate that the KVAT system could deliver dose to deep-seated lesions while sparing healthy tissues above the lesion, more complicated treatment scenarios needed to be investigated in order to demonstrate the clinical utility of KVAT. To this end, the second manuscript investigated MC simulated KVAT treatments of breast, lung and prostate patients. The main determining factor of success in these experiments was whether or not the KVAT plans could deliver the prescribed dose to the PTV without exceeding dose constraints placed on organs-at-risk. Our investigation into the capabilities and limitations of KVAT was also furthered by using inverse optimization to take advantage of the large number of possible incident beam angles produced by the KVAT system.

5.1 Introduction

Studies have suggested a lack of adequate access to radiation therapy (RT) in low and middle-income countries (LMICs)[4–7]. One study, by Datta et al., estimates that by 2020 these countries may have a deficit of approximately 9000 medical linear accelerators (linacs)[6]. Furthermore, in 2004 it was estimated that some high-income countries, such as Great Britain, met only 50% of their demand for linacs. It can therefore be argued that there is a need for more cost-effective external beam RT systems in global cancer care. One possible solution to this problem is the use of lower energy kilovoltage x-ray technology, which has the benefit of being less expensive and requires less shielding.

One of the first attempts to treat non-superficial lesions with kilovoltage photons was grid therapy in the early 1900's[54]. This technique employed a metal "grid" through which the primary photon beam passed and created an array of parallel small photon beams. The intent behind this method was to spatially fractionate the delivered radiation, thereby reducing the complications

suffered by the skin. Treatment of deep-seated lesions with kilovoltage photons has also been investigated by a number of groups more recently. Rose et al.[55] used a modified CT scanner to treat contrast injected brain metastases and reported a reduction in the size of the metastases while maintaining safe brain doses. Prionas et al.[35] demonstrated the feasibility of using a dedicated breast CT scanner for breast irradiation. Lastly, Abbas et al.[56] utilized a polycapillary optical cable to produce converging kilovoltage x-rays with a focal spot size of 0.2 mm to produce a skin sparing effect.

Our group has created a Monte Carlo (MC) model of a kilovoltage (kV) arc-therapy (KVAT) system, which has been designed to treat deep-seated lesions while sparing skin and organs at risk (OARs). This is accomplished by using a specially designed collimator to create a linear array of converging beamlets. The beamlets are spread over a larger volume of healthy tissue and skin while converging at isocenter to deliver a higher dose to the treatment volume. Previously, we calculated KVAT RT plans for cylindrical water phantoms and generated crudely optimized KVAT plans for spherical targets in patients. This study served as a preliminary evaluation of the KVAT system's irradiation capabilities. The main conclusion from this previous work was the need for more advanced planning methods to improve the quality of KVAT plans in order to spare OARs and decrease dose to bony anatomy.

Here we present inversely optimized KVAT plans for breast, lung and prostate patients. As this work is intended as an intermediate step in the systematic and theoretical evaluation of the KVAT system, idealized spherical volumes were used as planning treatment volumes (PTVs) within the patients. The inverse optimization process was guided by dose constraints on OARs as documented by RTOG protocols and relevant literature. Our KVAT plans were compared to MC generated megavoltage (MV) volumetric modulated arc therapy (VMAT) plans as points of

reference for the quality of contemporary clinical RT. The goal of this work was to evaluate the quality of inversely optimized KVAT plans in the presence of at-risk organs and bony anatomy and to determine if these plans are safe enough for patients to warrant further development of the KVAT system.

5.2 Materials and Methods

5.2.1 KVAT Source Design

Figure 5.1 is a rendering of one potential design of the KVAT system and illustrates the x-ray source mounted on a slip-ring gantry and the location of the patient on the treatment couch. Figure 5.2 is a modified image from our previous work[57] and illustrates the geometry of the KVAT transmission source and the geometry of KVAT radiation delivery. The x-ray source MC model consists of a 60-cm by 1-cm tungsten transmission anode with an electromagnetically steered electron beam running at 200-225 keV for radiation therapy as well as lower energies for imaging. A 0.4-mm copper filter is positioned below the anode to harden the beam. A specially designed collimator with a depth of 10 cm containing up to 31 diverging (increasing diameter) holes is positioned below the copper filter. The number of holes in the collimator is dependent on the size of the planning treatment volume (PTV) being irradiated.

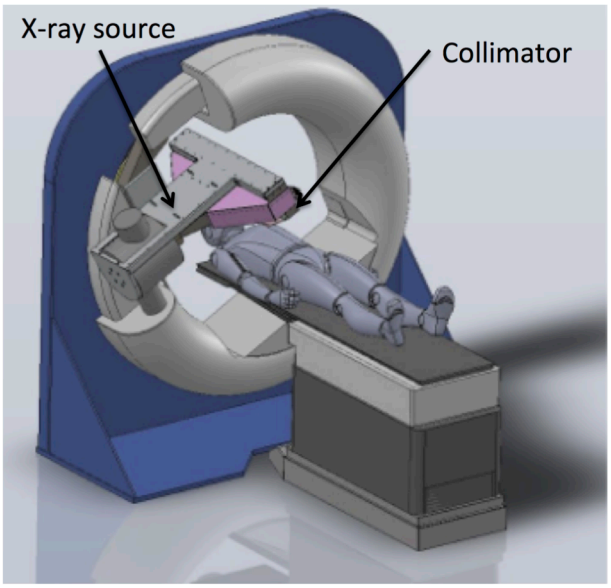

Figure 5.1 - Illustration of the KVAT system and patient geometry.

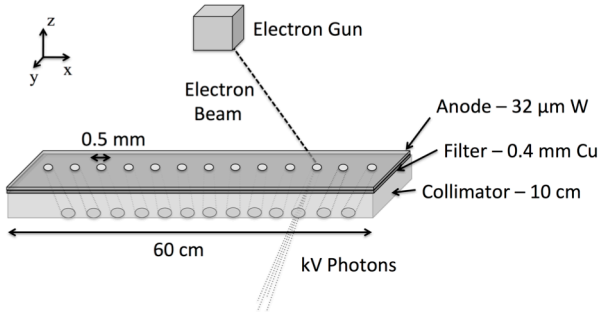

Figure 5.2a - Illustration of the KVAT transmission source.

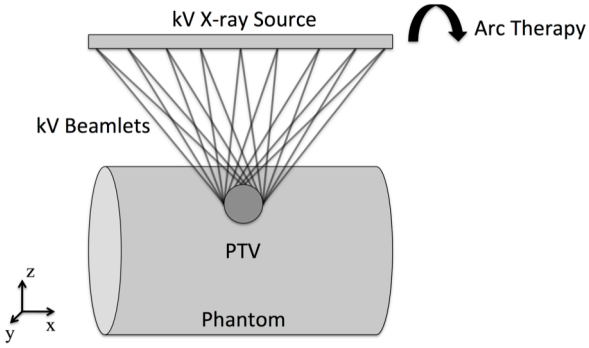

Figure 5.2b – Illustration of the geometry of KVAT radiation delivery to a phantom.

Bremsstrahlung photons are generated in the anode and are collimated into up to 31 beamlets focused at isocenter (the origin of the treatment coordinate system placed at the center

of the PTV). The collimator has been designed such that the width of the beamlets at isocenter is equal to the width of the PTV being treated. As a result, the number of circular collimator apertures and their diameter is calculated based on the size of the PTV. PTV depth does not affect collimator design, as the patient will be positioned such that the centre of the PTV is at isocenter. Since the diameter of the collimator apertures is dependent on PTV size, several collimators will be needed and collimators will be exchanged depending on the needs of the treatment, similar to early CyberKnife™ systems[58].

Collimator design parameters are listed in Table 5.1. These values were determined through computer optimization and MC modeling[36]. Experimental validation of a source of similar design and energy was performed previously by our group[37]. The source-to-axis distance (SAD), which is measured from the bottom of the collimator to isocenter, was fixed at 30 cm. The collimator aperture size of 0.5 mm is defined at the top of the collimator and is the same for all collimators, regardless of the PTV size.

Table 5.1 – KVAT source design parameters.

Parameter	*Value*
Electron beam energy	200 - 225 keV
Anode thickness	32 μm
Beam filtration	0.4 mm Cu
Number of collimator holes	27 - 31
Source extent	60 cm
Collimator hole size	0.5 cm
Collimator thickness	10 cm
Source-to-axis distance	30 cm
Treatment arc angle	180 - 360 degrees

5.2.2 KVAT Source MC Simulations

The KVAT source was simulated with the BEAMnrc package of EGSnrc[38]. An incident monoenergetic electron pencil beam with 200 keV was modeled for the breast patient while 225 keV monoenergetic electrons were used for the lung and prostate patients. 200 keV was used for the breast patient since the PTV was not located behind any bone that would receive higher dose due to increased beam attenuation. The mean energy of the 200 keV spectrum was 91.82 keV

while the mean energy of the 225 keV spectrum was 97.67 keV. Given the larger amount of bony anatomy in the lung and prostate patient, any increased beam penetration was deemed worthwhile. The incident beam position was simulated separately for each beamlet at an anode location that maximized x-ray fluence. The anode was modeled with the "SLABS" module and consisted of 32 μm of tungsten. Below the anode is 20 μm of niobium, 5 mm of beryllium and 3 mm of water for heat dissipation as well as a 0.4 mm copper filter. Due to the limitations of the BEAMnrc/EGSnrc modelling code, specifically the non-flexible square dimensions of the component modules used for the anode and filter, the anode was modelled with a 60-cm by 60-cm slab. It should be noted that this has no effect on the production photons in comparison with the 60-cm by 1-cm anode in the design.

The collimator was modeled with five "BLOCK" modules using brass C35300; each block had a thickness of 2 cm for a total thickness of 10 cm in order to produce sharp beamlet penumbras. Splitting the collimator into sub-components was necessary to control the divergence of the holes, as the vertices of each hole can only be explicitly defined at the top of each component module. The diameter of each opening at the top of the collimator was 0.5 cm. Each collimator opening was modeled with an eight-sided polygon. Thirty-one openings were used for the 3-cm PTVs while twenty-seven openings were used to treat the 4-cm PTV. The maximum number of openings was used while maintaining a minimum septa thickness of 3.5 mm on the bottom of the collimator. The collimator openings were designed such that all beamlets intersect at the center of the PTV.

Energies of 0.521 MeV (including rest energy of 0.511 MeV) and 0.01 MeV were used as the transport cutoff values for electrons and photons, respectively, in all BEAMnrc calculations. Electron and photon energy cutoffs of 0.811 MeV and 0.01 MeV, respectively, were used in

DOSXYZnrc calculations. All simulations used XCOM cross-section data. Photons in each beamlet were scored after leaving the collimator in separate phase space files for dose calculations in DOSXYZnrc[59]. Variance reduction techniques were used to decrease BEAMnrc simulation time: bremsstrahlung cross-section enhancement with an enhancement factor of 1 and an enhancement constant of 200 was and uniform bremsstrahlung splitting with a splitting factor of 200[39]. Russian roulette was turned on for both techniques.

5.2.3 Patient Studies

To evaluate the feasibility of KVAT treatments in a straightforward fashion, KVAT and VMAT doses were calculated to idealized PTVs located at three treatment sites. A 3-cm diameter spherical PTV was simulated in a breast and a lung patient and a 4-cm diameter spherical PTV was simulated in a prostate patient. The 3-cm lung PTV consisted of a 1-cm sphere of muscle surrounded by lung tissue. The breast PTV was located in the left breast at a depth of 3 cm. The lung PTV was located at a depth of 9 cm in the patient's left lung. The prostate PTV was located at a depth of 20 cm. Depth was measured as the distance from the skin to the center of the PTV along the line from the center of the collimator. Table 5.2 summarizes the PTV size and depth, beam energy, treatment arc and dose prescriptions for each patient.

Table 5.2 – PTV diameter and depth, beam energy, treatment arc and dose prescription for the breast, lung and prostate patients.

Patient case	*PTV diameter (cm)*	*PTV depth (cm)*	*Beam energy (kV)*	*Treatment arc (degrees)*	*Dose prescription (Gy)*
Breast	3	3	200	180	38.5
Lung	3	9	225	360	60
Prostate	4	20	225	360	73.8

5.2.4 Dose Prescription and Organs-at-Risk Constraints

Dose prescription and dose constraints on OARs were taken from RTOG protocols 0413, 0617 and 0415 for the breast, lung and prostate cases, respectively[43,60,61]. Table 5.3 contains all dose constraints used. A prescription of 60 Gy delivered in 2 Gy/fx over a total of 30 fractions was used for the lung patient. A dose prescription of 38.5 Gy delivered in 3.85 Gy/fx over 10 fractions was used for the breast patient. For the prostate patient, 73.8 Gy was prescribed and delivered in 1.8 Gy/fx over 41 fractions. All dose prescriptions were specified to 95% of the PTV volume (D_{95}) and all presented dose distributions were normalized to D_{95}.

In the breast patient case, the OARs considered were ribs, left lung, heart, uninvolved healthy left breast tissue and skin. The esophagus, spinal canal, ribs, heart, skin and lungs were considered OARs for the lung patient. Lastly, for the prostate patient, the rectum, bladder, femoral heads, inferior spinal vertebrae, skin, pubic bone and acetabulum were considered OARs. No dose constraints for femoral heads, skin, ribs, acetabulum, spinal vertebrae or pubic bones existed in these protocols and as a result the dose constraints for these organs were taken from published data on radiation complications[49,52,60,62,63]. The rationale for each of these dose constraints is included in the discussion and the values of all constraints are included in Table 5.3.

Table 5.3 – Dose constraints for organs-at-risk.

Organ (Patient case)	*Max dose (Gy)*	*Volume (%)*	*Prescription dose (Gy)*
Heart (Breast)	1.9	40	38.5
Healthy left breast (Breast)	19.3, 38.5	60, 35	38.5
Left lung (Breast)	11.5	15	38.5
Ribs (Breast, Lung)	53.6	0	38.5, 60
Heart (Lung)	40, 45, 60	100, 67, 33	60
Esophagus (Lung)	34 (mean dose)	-	60
Spinal canal (Lung)	50.5	0	60
Healthy left lung (Lung)	20 (mean dose)	-	60
Bladder (Prostate)	65, 70, 75, 80	50, 35, 25, 15	73.8
Rectum (Prostate)	60, 65, 70, 75	50, 35, 25, 15	73.8
Acetabulum (Prostate)	50	50	73.8
Pubic bone (Prostate)	50	50	73.8
Femoral head (Prostate)	40, 45	40, 25	73.8
Spinal vertebrae (Prostate)	50.5	0	73.8
Skin (Breast, Lung, Prostate)	0.25 (per fx)	0	38.5, 60, 73.8

5.2.5 KVAT Dose Calculations and Optimization

All KVAT dose calculations were run with the DOSXYZnrc package of EGSnrc[59] and the dose to medium was reported. The dose calculated by DOSXYZnrc was converted into dose rate in cGy/min using the conversion factor of 2.96×10^{19} particles per minute of irradiation at a tube current of 200 mA[36].

For the KVAT simulations, computed tomography (CT) images of each patient were converted into an .egsphant file with 2.5 mm × 2.5 mm × 2.5 mm voxels using the Radify (LifeLine Software, Inc., Austin, TX) web application. Four materials were used for each patient phantom. All patients used air and skeletal muscle, while the breast and lung patients also used inflated lung and ribs (2-6), and the prostate patient used gastrointestinal tract and femoral bone. All material composition definitions were taken from International Commission on Radiological Protection (ICRP) data[47] and converted into material files used by DOSXYZnrc. A clinical CT

calibration curve was used to convert Hounsfield units (HU) to mass densities. For the lung and breast patient, the HU range corresponding to each material was as follows: air (-1000:-950), lung (-950:-300), muscle (-300:100) and ribs (100:2000). For the prostate patient the following ranges were used: air (-1000:-950), gastrointestinal tract (-950:-300), muscle (-300:100) and compact bone (100:2000).

The breast patient was treated with a 180-degree arc while the prostate and lung patient were treated with 360-degree arcs. A 180-degree arc was used for the breast case to reduce dose to the patient. The treatment arcs were divided in 5-degree increments. At each treatment angle the dose for each of the 27 or 31 beamlets was calculated. The maximum statistical uncertainty in the voxels with the 20 highest doses was no more than 2.5% for all high-dose beamlets. Statistical error was further reduced as each beamlet is weighted and summed through the process of inverse optimization due to the summation of beamlets at isocenter.

Inverse optimization of KVAT treatments was performed using the McGill University optimization (McO) framework. McO utilized a column generation method for optimization along with quadratic one-sided voxel-based penalty functions and DVH-based penalties[31]. Each beamlet was weighted during the optimization process and assigned a beam-on time in minutes. The maximum number of iterations for each optimized plan was set to 150. The data output of the optimization process was a single .3ddose file and a data file containing the beam-on time for all beamlets.

5.2.6 VMAT Dose Calculations and Optimization

For reference, VMAT treatments planned in Eclipse™ (Varian Medical Systems, Palo Alto, CA) for a Varian TrueBeam™ linear accelerator were simulated using VMC++[21] code and validated in-house software with the same HU to mass density calibration curve used in KVAT dose calculations[64,65]. We employed another MC technique rather than Eclipse™ dose

calculations to produce most accurate dose comparison given the tissue heterogeneities in the lung plans. Breast and lung plans were simulated with energy of 6 MV and the prostate plan was simulated at 15 MV. 15 MV was chosen for the prostate plan to increase penetration of the beam through bony anatomy. VMAT VMC++ simulations also used a voxel size of 2.5 mm × 2.5 mm × 2.5 mm and the dose to medium was reported. All VMC++ dose calculations had a statistical uncertainty of less than 1%.

5.2.7 Data Analysis

Dose data analysis was performed using RT_Image[46] and MATLAB[66]. Axial, sagittal and coronal dose distributions were generated for the KVAT and VMAT plans. Cumulative DVHs for the PTV and OARs (with the exception of skin) were calculated for both optimized KVAT and VMAT plans. For skin, the maximum dose delivered is reported as an indication of skin complication. Mean dose delivered to the partial patient body volume of the CT (referred to as partial body dose) and each OAR except for the skin was calculated. PTV dose homogeneity was calculated as the difference between D_2 and D_{98} normalized by D_{50} as suggested by ICRU 83[67]. The treatment time for each of the optimized KVAT plans was also calculated.

5.3 Results

5.3.1 Dose Distributions and Treatment Times

Figure 5.3 illustrates the axial, coronal and sagittal dose distributions for the 180-degree 200 kV KVAT and 6 MV VMAT breast patient treatments. Figure 5.4 provides the DVH for the PTV, heart, left lung, ribs and uninvolved healthy left breast tissue for the 200 kV KVAT and 6 MV VMAT breast treatments. PTV homogeneity values were 0.231 and 0.056 for KVAT and VMAT, respectively. The KVAT treatment time per fraction was 2.8 minutes. The maximum KVAT skin dose per fraction was 220 cGy/fx. Table 5.4 summarizes the prescription doses and calculated total treatment times for the breast, lung and prostate patient cases. Table

5.5 lists dose constraints for each OAR as well as the dose delivered by KVAT and VMAT to the organ volume relevant to each dose constraint. Table 5.6 lists the mean doses delivered by KVAT and VMAT to all OARs except skin. Table 5.7 lists the homogeneity values of the PTV in the KVAT and VMAT plans.

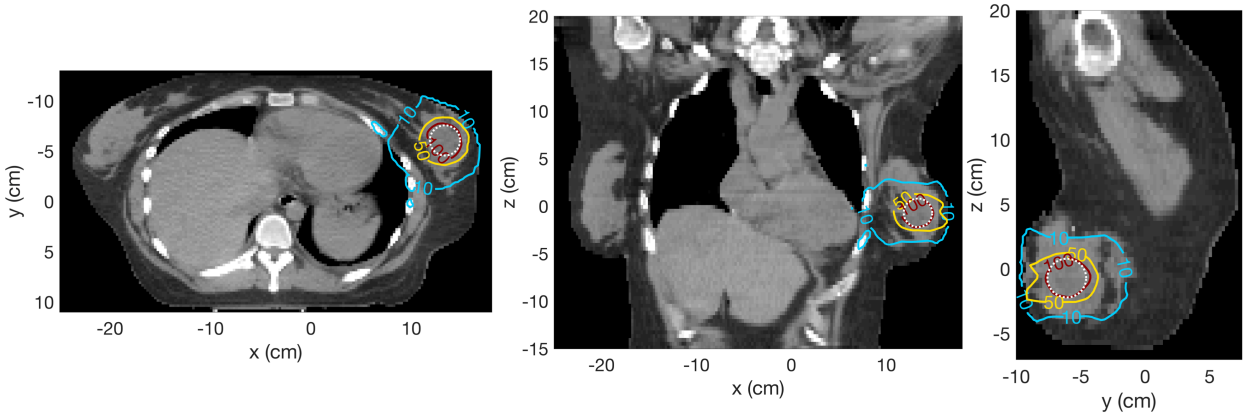

Figure 5.3a - Axial, coronal and sagittal dose distributions of the 180-degree 200 kV KVAT breast treatments. Dose distributions are normalized to D95. Isodose lines shown are 10%, 50% and 100%.

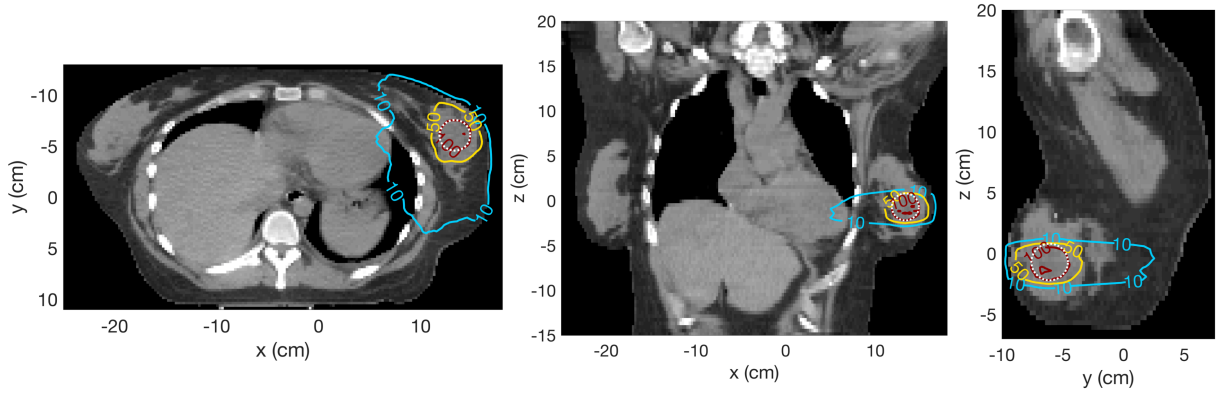

Figure 5.3b - Axial, coronal and sagittal dose distributions of the 180-degree 6 MV VMAT breast treatments. Dose distributions are normalized to D95. Isodose lines shown are 10%, 50% and 100%.

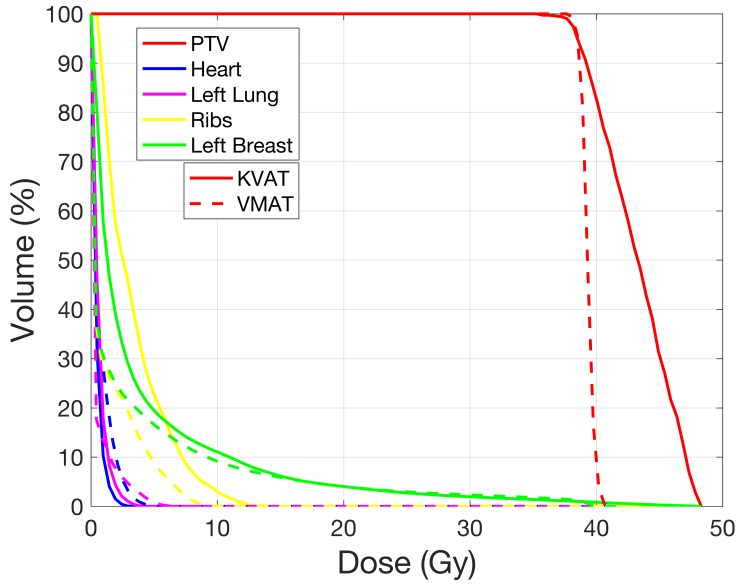

Figure 5.4 - DVHs for the 200 kV KVAT (solid line) and 6 MV VMAT (dashed line) breast treatments.

Table 5.4 – KVAT treatment times and prescribed doses for the breast, lung and prostate patient cases.

Patient case	*Prescription dose (Gy)*	*Dose per fraction (cGy)*	*Total treatment time (min)*	*Treatment time per fraction (min)*
Breast	38.5	385	28.3	2.8
Lung	60	200	78.8	2.6
Prostate	73.8	180	223.8	5.5

Figure 5.5 depicts the axial, coronal and sagittal dose distributions for the 360-degree 225 kV KVAT and 6 MV VMAT lung patient treatments. Figure 5.6 illustrates the DVH for the PTV, heart, uninvolved healthy left lung tissue, ribs, esophagus and spinal canal for the 225 kV KVAT and 6 MV VMAT lung plans. PTV homogeneity values were 0.076 and 0.147 for KVAT and VMAT, respectively. The treatment time per fraction was 2.6 minutes. The maximum KVAT skin dose per fraction was 58 cGy.

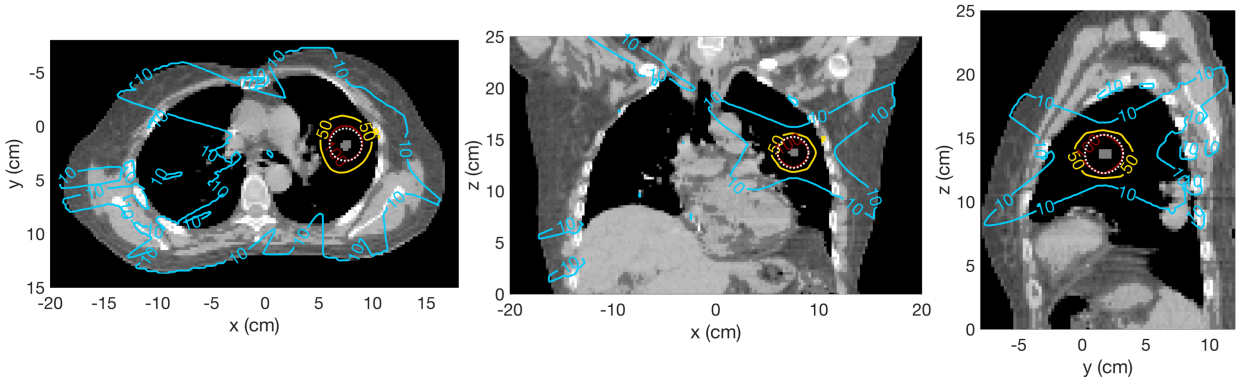

Figure 5.5a - Axial, coronal and sagittal dose distributions of the 360-degree 225 kV KVAT lung treatments. (b) 360-degree 6MV VMAT lung treatments. Dose distributions are normalized to D95. Isodose lines shown are 10%, 50% and 100%.

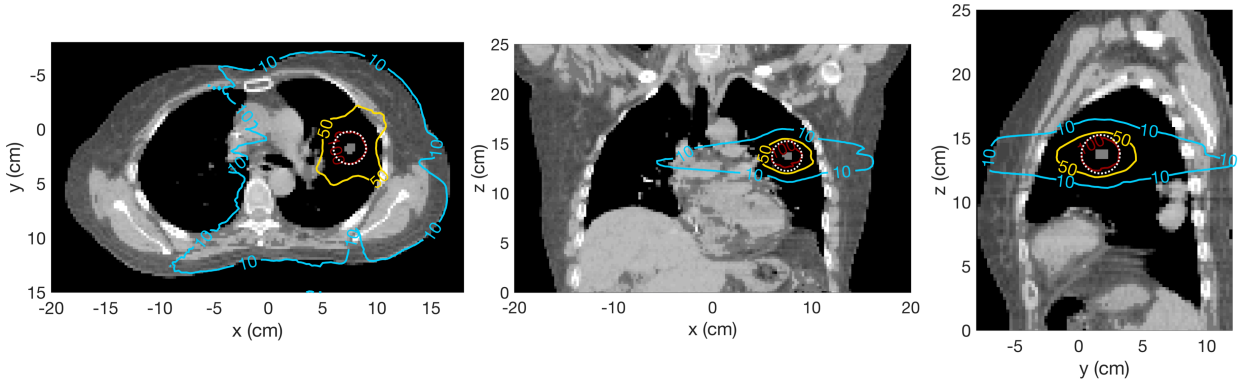

Figure 5.5b - Axial, coronal and sagittal dose distributions of the 360-degree 6MV VMAT lung treatments. Dose distributions are normalized to D95. Isodose lines shown are 10%, 50% and 100%.

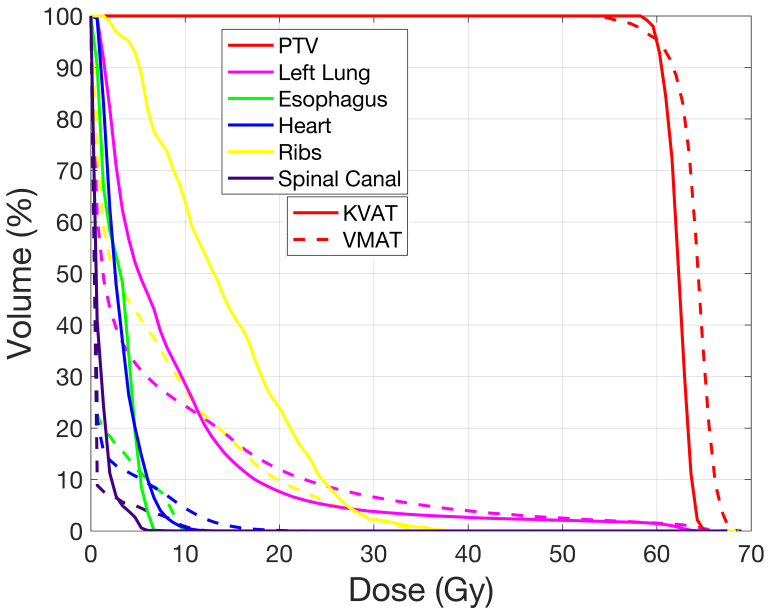

Figure 5.6 - DVHs for the 225 kV KVAT (solid line) and 6 MV VMAT (dashed line) lung treatments.

Figure 5.7 provides the axial, coronal and sagittal dose distributions for the 360-degree 225 kV KVAT and 15 MV VMAT prostate patient treatments. Figure 5.8 depicts the DVH for the PTV, bladder, rectum, pubic bones, left acetabulum, left femoral head, and spine for the 225 kV KVAT and 15 MV VMAT prostate treatments. PTV homogeneity values were 0.177 and 0.124 for KVAT and VMAT, respectively. The KVAT treatment time per fraction was 5.5 minutes. The maximum KVAT skin dose per fraction was 90 cGy.

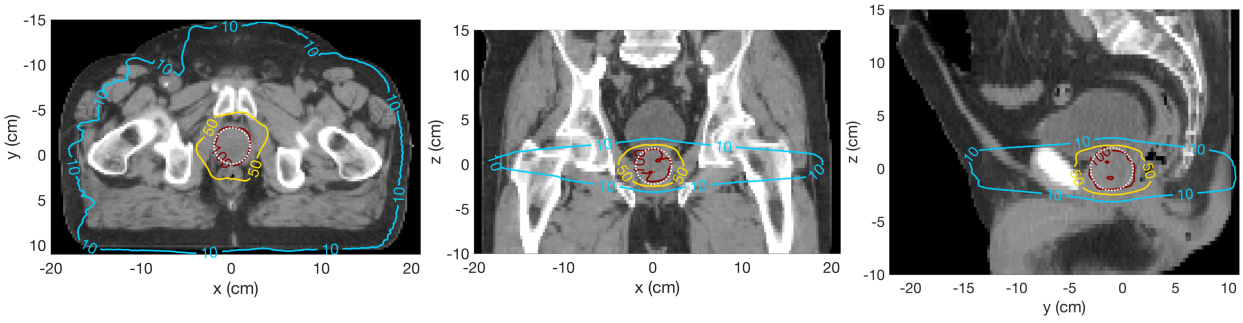

Figure 5.7a - Axial, coronal and sagittal dose distributions of the 360-degree 225 kV KVAT prostate treatments. Dose distributions are normalized to D95. Isodose lines shown are 10%, 50% and 100%.

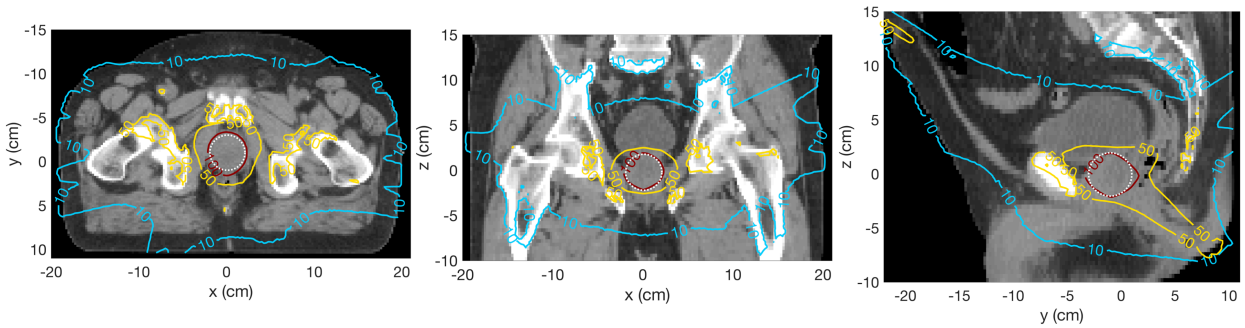

Figure 5.7b - Axial, coronal and sagittal dose distributions of the 360-degree 15 MV VMAT prostate treatments. Dose distributions are normalized to D95. Isodose lines shown are 10%, 50% and 100%.

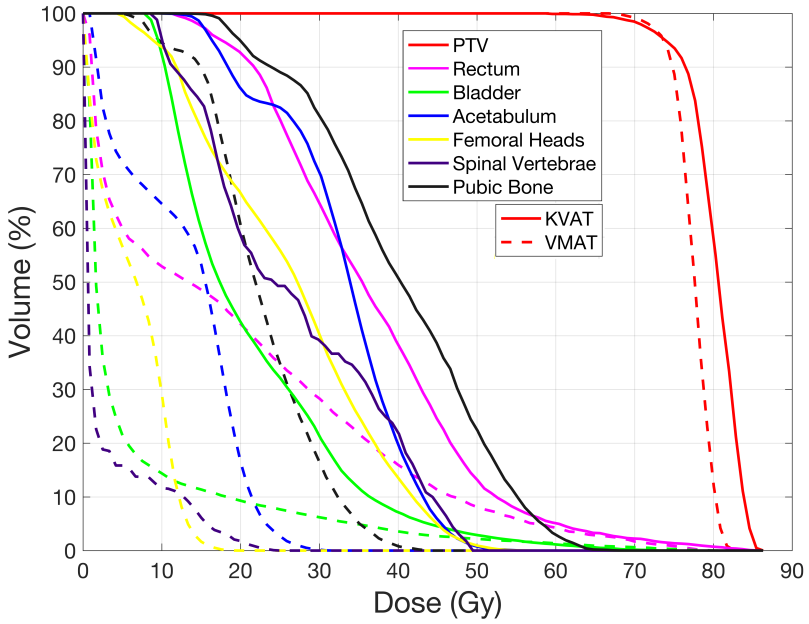

Figure 5.8 - DVHs for the 225 kV KVAT (solid line) and 15 MV VMAT (dashed line) prostate treatments.

Table 5.5 – Dose constraints and doses delivered to each OAR the breast, lung and prostate patient plans.

Organ (Patient case)	*Max dose (Gy)*	*KVAT delivered dose (Gy)*	*VMAT delivered dose (Gy)*	*Volume (%)*
Heart (Breast)	1.9	0.4	0.4	40
Healthy left breast (Breast)	19.3, 38.5	0.9, 2.3	0.3, 0.6	60, 35
Left lung (Breast)	11.5	1.1	0.7	15
Ribs (Breast)	53.6	14.0	10.6	0
Skin (Breast)	2.5 (per fx)	2.2 (per fx)	1.4 (per fx)	0
Heart (Lung)	40, 45, 60	0, 1.9, 3.6	0, 0.3, 0.6	100, 67, 33
Esophagus (Lung)	34 (mean dose)	2.6	1.1	-
Ribs (Lung)	53.6	39.5	35.9	0
Spinal canal (Lung)	50.5	9.4	13.1	0
Healthy left lung (Lung)	20 (mean dose)	8.2	7.1	-
Skin (Lung)	2.5 (per fx)	0.6 (per fx)	0.6 (per fx)	0
Bladder (Prostate)	65, 70, 75, 80	17.3, 23.3, 28.5, 32.8	1.7, 2.5, 4.2, 9.2	50, 35, 25, 15
Rectum (Prostate)	60, 65, 70, 75	35.4, 41.2, 44.7, 48.9	13.3, 25.0, 31.9, 40.9	50, 35, 25, 15
Acetabulum (Prostate)	50	33.9	15.5	50
Pubic bone (Prostate)	50	40.3	21.8	50
Femoral head (Prostate)	40, 45	30.1, 35.0	8.7, 10.4	40, 25
Spinal vertebrae (Prostate)	50.5	49.5	25.0	0
Skin (Prostate)	2.5 (per fx)	0.9 (per fx)	0.3 (per fx)	0

Table 5.6 – Mean dose values for OARs.

Organ (Patient case)	*KVAT mean dose (Gy)*	*VMAT mean dose (Gy)*
Heart (Breast)	0.2	0.5
Healthy left breast (Breast)	3.7	2.9
Left lung (Breast)	0.4	0.3
Ribs (Breast)	3.1	1.2
Partial Body (Breast)	0.27	0.34
Heart (Lung)	2.8	1.2
Esophagus (Lung)	2.6	1.1
Ribs (Lung)	13.7	6.6
Spinal canal (Lung)	0.6	0.5
Healthy left lung (Lung)	8.2	7.1
Partial Body (Lung)	1.91	0.93
Bladder (Prostate)	21.0	5.8
Rectum (Prostate)	36.2	18.8
Acetabulum (Prostate)	32.4	12.4
Pubic bone (Prostate)	39.9	22.2
Femoral head (Prostate)	26.0	6.0
Spinal vertebrae (Prostate)	26.5	2.3
Partial Body (Prostate)	10.06	2.17

Table 5.7 – PTV dose homogeneity values for the KVAT and VMAT breast, lung and prostate plans.

Patient case	*KVAT PTV homogeneity*	*VMAT PTV homogeneity*
Breast	0.231	0.056
Lung	0.076	0.147
Prostate	0.177	0.124

5.3.2 Inverse Optimization and Treatment Time Reduction

In order to illustrate the benefits of inverse optimization, the DVH for a non-optimized KVAT lung plan, which uses a simple beamlet-weighting scheme, is show in Figure 5.9 and compared to the optimized KVAT lung plan. The clearest improvement is reduced rib dose and improved PTV homogeneity. The column generation method finds the beamlet that will have the largest first-order impact on reducing the cost function at every iteration. The beginning of the optimization process is an empty plan with a corresponding dose distribution of 0 Gy in every voxel, meaning that only PTV under-dosing objectives are active. As such, the beamlet which delivers the most dose to the PTV is typically the beamlet chosen by the algorithm to start the optimisation run. The column generation method then uses this first solution to determine the most cost-effective beamlets and adds these in successive iterations[31]. As a result, the cost function of the optimization process quickly decreases and plateaus. This characteristic can be seen in Figure 5.10a in which the cost function of the lung KVAT plan is plotted as a function of iteration number. Since more iterations results in longer treatment times, it is possible to reduce treatment time by reducing the maximum number of iterations the optimizer uses. As an example, we attempted to reduce the treatment time by approximately 33% and then determined the impact on the quality of the treatment plan. After 58 iterations the cost function has decreased to a value only 6.4% higher than its final value at iteration 150. Running a second

optimization with a maximum of 58 iterations yields a treatment time of 48.6 minutes. This is a 37% reduction in treatment time from the original KVAT lung plan. Consequently, the treatment time of the lung KVAT plan can be easily reduced by limiting the maximum number of iterations while only marginally reducing the quality of the plan. Figure 5.10c illustrates the dose volume histograms of the original KVAT lung treatment plan and the lung treatment plan that has been limited to 58 iterations.

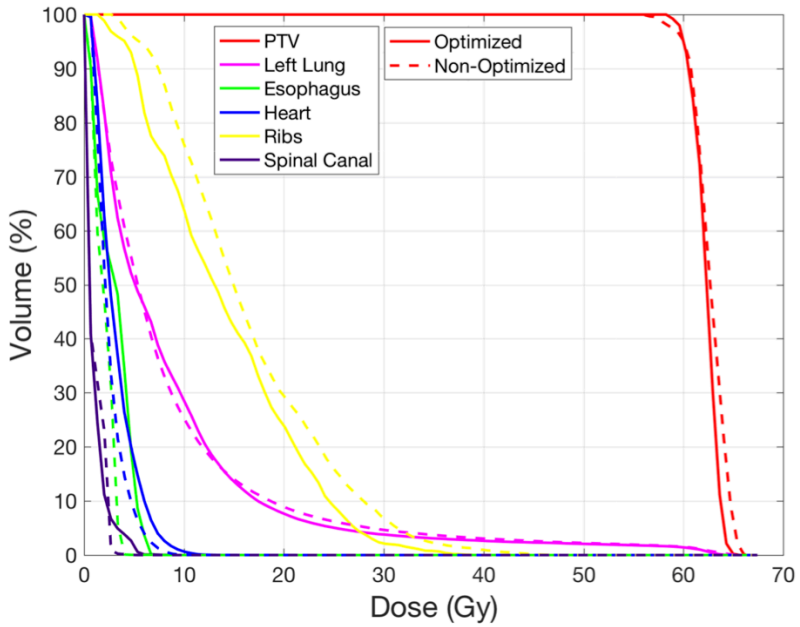

Figure 5.9 - DVH comparison of the optimized KVAT lung plan and the (non-optimized) KVAT lung plan with a simple beamlet-weighting scheme.

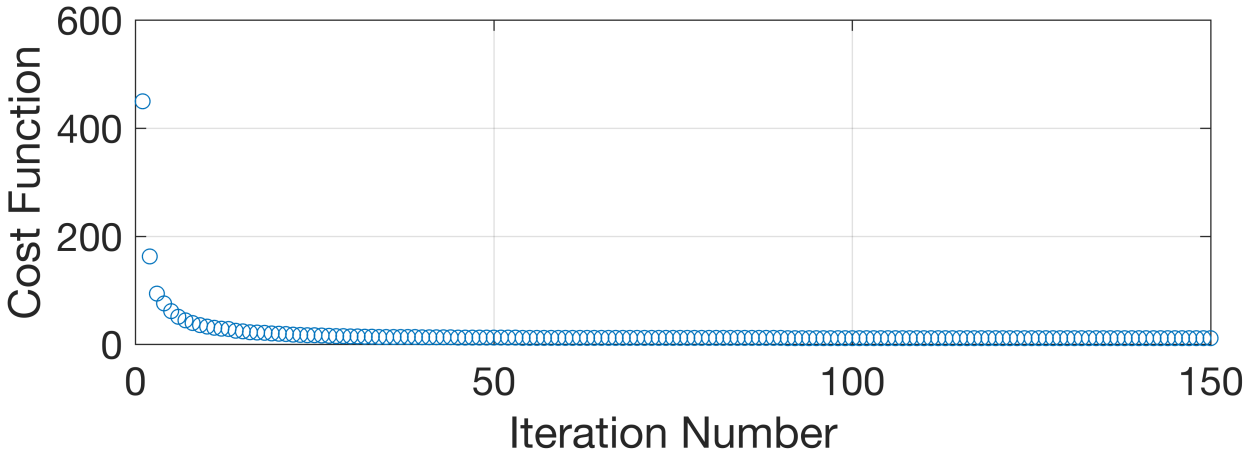

Figure 5.10a – Cost function as a function of iteration number for the lung KVAT optimization plan.

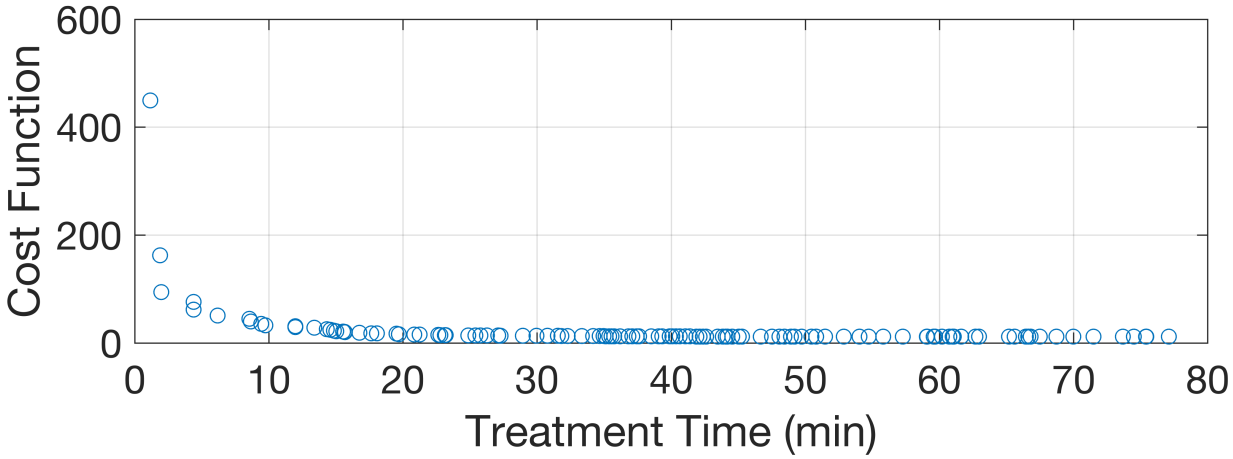

Figure 5.10b – Cost function as a function of treatment time for the lung KVAT optimization plan.

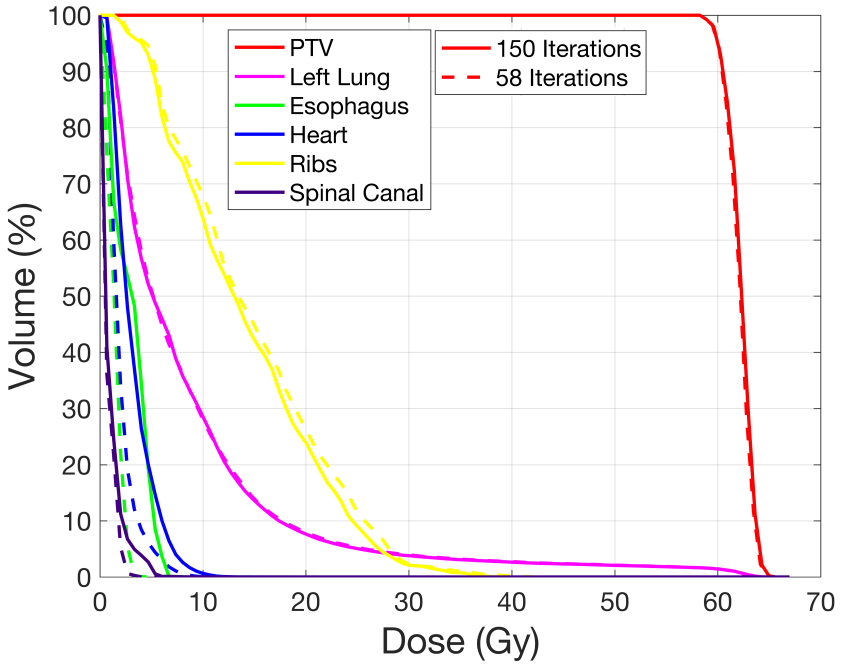

Figure 5.10c - DVHs for the 225 kV KVAT lung treatment without an iteration limit (solid line) and with the iterations limited to 58 (dashed line).

5.4 Discussion

As previously stated, the goal of this study was to evaluate the quality of optimized KVAT plans by comparison to MV VMAT plans. In the following sections, the breast, lung and prostate KVAT and VMAT plans will be assessed according to DVHs, dose distributions, PTV homogeneity and mean integral body dose.

5.4.1 Analysis of Dose Distributions

All dose constraints on the heart, left lung and ribs were met in both breast plans. From Figure 5.3 it can be seen that 200 kV KVAT and 6 MV VMAT plans achieve similar conformality of the 3-cm breast PTV. The VMAT plan, however, resulted in a deeper penetration of the beam due to the higher energy of the 6-MV photons, which can be observed from the dose distributions. Figure 5.4 shows that the primary difference between the KVAT and VMAT breast treatment is the homogeneity of the dose within the lesion. The KVAT plan produced regions of higher dose within the PTV due to the overlap of the beamlets, a

phenomenon which has been observed in previous work[57]. This is not of concern as there has been evidence that a heterogeneous dose within the PTV may not be detrimental[68]. We can also observe from Figure 5.4, increased rib dose and minimal increases in the dose delivered to the healthy left breast and left lung tissue in the KVAT plan compared to VMAT. The VMAT plan results in minimal dose increases to the heart. The lower rib dose in the VMAT is expected considering the higher attenuation and energy absorption of low energy photons by bone.

Both lung plans met dose constraints for all OARs. A comparison of the 225 kV KVAT and 6 MV VMAT lung plans in Figure 5.5. We can see that, unlike the breast plan, the lung KVAT plan delivered higher volumes of low-dose to the entire patient due to the large number of beamlet directions over the 360-degree arc. This is reflected by an increased mean partial body dose of 1.91 Gy in comparison to the 0.93 Gy delivered by VMAT. The lung patient DVH shows a higher dose to ribs with the KVAT plan, which is expected given the lower energy of the kV photons. Despite the increase in rib dose, the KVAT plan did not exceed rib constraints. A larger volume of healthy left lung tissue received doses less than 12 Gy in the KVAT plan while the VMAT plan delivered doses of 12 – 45 Gy to marginally higher volumes of the left lung. For the spinal canal, esophagus and the heart the KVAT plan resulted in larger volumes of tissue receiving low doses while the VMAT plan resulted in marginally larger volumes of tissue receiving high doses. The homogeneity of the KVAT and VMAT lung plans are similar. This increased KVAT homogeneity is due to the 360-degree arc used in this plan.

All OAR constraints were met in both the KVAT and VMAT prostate plans. The homogeneity index of the KVAT prostate plan was 0.177, the highest of any KVAT plan. Despite the 360-degree arc used by the plan, the heavy beamlet modulation employed to avoid large volumes of bony anatomy results in an inhomogeneous PTV dose distribution. From Figure

5.7 we can observe the difficulty of treating the prostate patient with 225 kV photons. The 50% isodose line covers a large volume of the bony anatomy surrounding the prostate. This is due to the increased thickness of the bones in the pelvis in comparison to the chest. Additionally, due to the limited number of beam angles that do not pass through bone we see a high weighting on posterior-inferior beamlets in the sagittal image, resulting in high doses to healthy tissue and the skin. In Figure 5.8 we see higher doses being delivered to all OARs in the KVAT plan. This is again indicative of the difficulty of delivering 225 kV photons in an anatomical region with thick bony anatomy. In order to deliver the needed dose to the PTV a longer beam-on time is required when delivered at lower energy. While all OARs were within constraints, the spinal vertebrae were extremely close to the dose constraint of 50.5 Gy, the dose to the rectum was quite high with 10% of the volume receiving 52 Gy and large volumes of healthy tissue received 50% of the prescription dose. Lastly, the mean partial body dose in the KVAT plan was very high at 10.06 Gy in comparison to the 2.17 Gy delivered by VMAT. It is evident that the KVAT system has difficulty treating the prostate PTV due to the presence of a large volume of bony anatomy. The extension of this result is that any lesion site, which involves a large volume of bony anatomy, such as head and neck cancers, will prove difficult for treatment with KVAT and may be a limitation of the system.

From Figure 5.9 it can be seen that limiting the number of optimization iterations to 58 had very little effect on the quality of the lung plan. For example, the ribs received a small increase to dose but were still within constraints. Of interest is the small increase in dose received by the spinal canal, esophagus and heart in the 150-iteration plan. This is simply due to a larger beam-on time used to treat the patient and the increases were marginal.

Treatment times per fraction were short for both breast and lung patients at 2.8 and 2.6 minutes, respectively. While the treatment time for the prostate patient was longer at 5.5 minutes, this is to be expected given the prostate's large depth in tissue and presence of larger bones through which the photons must penetrate. The reduction of treatment time is possible by limiting the number of iterations used by the optimization algorithm.

5.4.2 Additional Considerations for Dose Constraints

This section is intended to provide justification for the chosen dose constraints on organs that were not included in RTOG protocols. A literature review by Lee et al.[49] found that an orthovoltage (beam quality of 1 mm Cu half-value layer) dose of 3000 cGy delivered in 200 cGy fractions with a 10-cm × 10-cm field resulted in moderate late changes to the skin and acute desquamation. The 200 kV beam of our KVAT system has a half-value layer of 1.17 mm Cu delivered over a larger field size for the 360-degree arc treatments. Precise skin tolerances require clinical context to determine what range of complications are acceptable. Furthermore, skin reactions vary widely with dose prescription, dose fractionation, field size and beam energy. We therefore choose to use 250 cGy/fx as an estimated limit on skin dose in this work.

RTOG 0822 for rectum radiotherapy indicates that the femoral heads should receive no more than 40 Gy to 40% of their volume and no more than 45 Gy to 25% of their volume for a dose prescription of 45 Gy using a 1.8 Gy/fx fractionation scheme[62]. Given that these two constraints represent 89% and 100% of the RTOG 0822 prescription dose using the same fractionation scheme as our prostate prescription of 73.8 Gy, the absolute dose constraints of RTOG 0822 represent reasonable dose cut-offs for the femoral heads in our treatment.

In a study by Aoki et al.[52], it was found that no radiation-induced rib fractures occurred when the maximum dose delivered to the ribs was less than 5360 cGy delivered over 9 fractions with a fractionation scheme of 600 cGy per fraction. We can therefore estimate that the

maximum dose to ribs should not exceed 5360 cGy since none of our fractionation schemes exceed 600 cGy per fraction. RTOG 0630 recommends delivering no more than 50 Gy to 50% of the volume of any weight-bearing bones using a fractionation scheme of 2 Gy/fx to deliver a prescription dose of 50 Gy for the treatment of soft tissue sarcoma. RTOG 0630 uses a lower prescription dose and a similar fractionation scheme to what we have chosen for our prostate patient. For this reason, the absolute limit of 50 Gy to 50% of the weight-bearing acetabulum was chosen as a constraint for our study. While the pubic bone is not weight-bearing, we did not allow to receive more than 50 Gy to 50% of its volume. Due to innervation of the spinal vertebrae, as well as the presence of red bone marrow, the spinal vertebrae is more sensitive to radiation than simple weight bearing bone. For this reason, a maximum dose of 50.5 Gy, which is the dose limit on the spinal canal from RTOG 0617, is more reasonable for the spinal vertebrae.

It should be noted that RTOG dose constraints are specified as dose-to-water. This is also true for the dose constraint taken for rib dose since Aoki et al. measured rib dose in a treatment planning system. For this reason our dose-constraints for all bony anatomy would increase if converted to dose-to-medium constraints. As a result, these dose constraints were more restrictive than they necessarily need to be.

5.4.3 Future Work

Future work on the KVAT system will involve modeling more realistic non-spherical PTVs and experimental verification of the dosimetry of a prototype system. While experimental validation of the new source design is an essential step in this work, it is common practice to first perform MC simulations of a new source design before experimental validation.

5.5 Conclusions

EGSnrc/BEAMnrc, DOSXYZnrc and McO were used to inversely optimize treatments for breast, lung and prostate patient plans delivered using our novel, low-cost KVAT system. All patient plans were compared with VMC++ simulated MV VMAT treatments modeled with a clinical linac. All KVAT plans met the dose constraints on OARs while delivering the prescription dose to the PTV with fractional dose delivery times of no more than 5.5 minutes. However, despite being within dose limits, the prostate patient proved difficult for the KVAT system, due to the presence of large volumes of bone, and illustrates a limitation of the system. While MV VMAT plans delivered, in general, lower dose to OARs, the optimized breast and lung KVAT plans can be considered safe as all dose constraints were met. These results indicate the ability of our system to treat certain idealized, deep-seated lesions with kilovoltage photons while sparing healthy tissues. Furthermore, the results warrant continued study in order to fully determine the capabilities of KVAT technology.

6. Kilovoltage X-Ray Arc Therapy for Three Lung Cancer Patients

Under Review in the Journal of Medical Physics

Introductory Remarks

The third manuscript of this project aimed to extend the MC simulated, inversely optimized KVAT patient plans of the preceding work by considering three lung cancer patients who received stereotactic ablative radiotherapy treatment at the Vancouver Island Cancer Centre. Unlike the plans from previous work, which considered ideal spherical PTVs, the intent of this next investigation was to show that KVAT could be applied to real patients.

6.1 Introduction

An increasing number of research groups are investigating technologies to reduce the cost of radiation therapy (RT)[7]. The interest in this field of work is motivated by recent studies that suggest inadequate access to RT in low and middle-income countries (LMICs)[4,5]. For example, Datta et al. estimates that by 2020 there may be a deficit of approximately 9000 external beam RT systems in LMICs[6]. One potential solution is the use of lower energy kilovoltage (kV) x-rays in place of megavoltage (MV) x-rays from clinical linear accelerators (linacs), since the technology required to produce kV x-rays is less expensive and requires less infrastructure and less shielding to ensure a safe treatment environment. The first historical example of using of kV x-rays to treat deep-seated tumors is grid therapy. First used in the 1900s, grid therapy used an applicator with numerous parallel apertures. Placed in the beam's path, this applicator created spatially fractionated x-ray beams in an attempt to reduce radiation induced complications of the skin[54]. More recently, a number of groups have investigated various methods of adapting kV x-rays to treat deep-seated lesions[35,55,56,69]. Additionally, various research groups have studied the use of kilovoltage x-rays for stereotactic radiotherapy[70–74].

Our research group has created a MC model of a novel, low-cost kV x-ray arc therapy (KVAT) system. The intent of this system is not to replace current RT technology in LMICs but rather to supplement it. The KVAT system was designed to treat deep-seated lesions with kilovoltage photons of adequate power and commensurate heat dissipation delivered via a novel collimator designed to this end. The KVAT design uses an electromagnetically steered 200 keV electron beam and a 70 cm long, water-cooled, reflection-style tungsten anode. Below the anode is a specially designed collimator containing an array of diverging apertures. These apertures collimate the kV x-rays into beamlets which converge at isocenter. The planned dose to skin and healthy tissues is reduced due to the convergent nature of the beamlets wherein photons are spread out over a larger volume of healthy tissues and are focused on the treated volume, which is placed at isocenter. The dose to healthy tissues is further reduced with the use of arc therapy. By modulating the dwell time of the electron beam positions along the anode, true modulated arc therapy can be produced in order to improve dose conformality and avoid at-risk organs.

Previous work by our group has shown the experimental validation of a kilovoltage system which utilizes the same principle of multiple convergent kV beams[37]. As such, it is not within the scope of this work to provide further experimental verification. It should be noted that the MC model investigated in this work is an entirely new design, which utilizes a traditional stationary reflection x-ray tube for superior heat absorption. Furthermore, the collimator modeled in this work has been completely redesigned. Lastly, the system, which is modeled in this work, is currently under construction as a prototype of the KVAT system. Previous work used a MC model of an earlier KVAT system design with a transmission anode in which our group has demonstrated the feasibility of KVAT by simulating arc therapy with cylindrical water phantoms and the partial-breast irradiation of an idealized, spherical PTV in a breast patient[57]. We have

also investigated the use of inverse optimization methods to improve the quality of KVAT dose distributions[1]. This was done by simulating inversely optimized KVAT plans for ideal, spherical PTVs in breast, lung and prostate patients. In this current work we aim to extend our systematic investigation of the capabilities of KVAT by simulating inversely optimized kV plans for 3 clinical lung cancer patients who were treated with 6 MV stereotactic ablative radiotherapy (SABR) at the Vancouver Island Cancer Centre (VICC) of the BC Cancer Agency. We have chosen 3 patients with PTVs of various sizes and location in order to determine which cases may or may not be within dose constraints for organs-at-risk (OAR) using KVAT. Lung cancer patients were chosen due to the high incidence and mortality of lung cancer globally[75]. Furthermore, the range of tumor locations in the chosen 3 patients allowed us to investigate the effect to PTV location on treatment plans and is sufficient for this study. The goal of this work is to test the capabilities and limits of this new KVAT system design using MC techniques in order to determine if continued investigation into this technology is warranted.

6.2 Materials and Methods

6.2.1 KVAT Source Model and Design

The KVAT system consists of an x-ray tube with a 70 cm long, 3 cm wide, water-cooled, tungsten anode. The x-ray tube is mounted on a gantry to enable rotation of the source around the patient for the delivery of arc therapy. Figure 6.1a illustrates the general design of the KVAT system, showing the location of the x-ray tube with respect to the patient. As the 200 keV electron beam is steered across the anode, bremsstrahlung and characteristic photons are created. These photons are then filtered by 0.4 mm of copper and travel through the 70 apertures of the 6-cm thick collimator. The resulting beamlet array converges at isocenter, at a distance of 40 cm from the anode, which is positioned to be the center of the treated volume or planning treatment volume (PTV). Figure 6.1b depicts the design of the x-ray tube and collimator. In Figure 6.1c the

line along the anode which the electron beam is swept and the creation of convergent beamlets is illustrated.

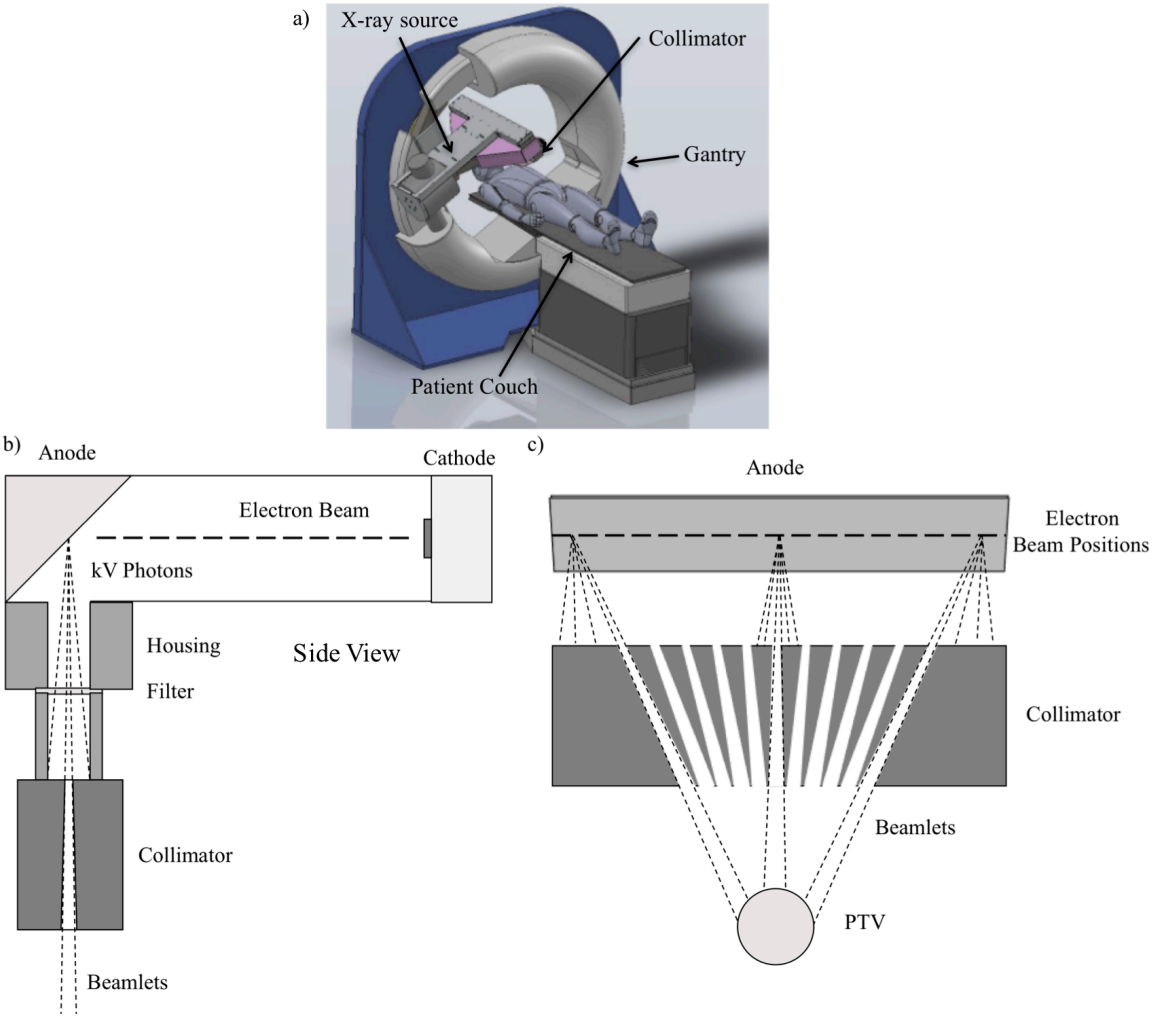

Figure 6.1 – (a) Rendering of the KVAT system showing the gantry, x-ray source, collimator and patient couch (modified from Breitkreutz et al.[1]). (b) Cross section of the KVAT system and (c) a simple illustration of the principle behind the converging beamlets created by the collimator.

6.2.2 KVAT Monte Carlo Model

The KVAT MC model was created using the EGSnrc/BEAMnrc software package[38]. BEAMnrc models consist of different varieties of component modules (CM) each of which is used to model a particular component of x-ray tubes or linear accelerators and their

accompanying components, such as collimators, filters, and metal housing. The first CM of the KVAT model is an XTUBE CM with a 30 degree, 0.1 mm thick tungsten anode (Figure 6.1b and 6.1c). The tungsten anode is embedded in a large copper block for heat dissipation. A 200 keV, circular electron beam with a radius of 0.11 cm was incident on the tungsten anode for all simulations. One limitation of BEAMnrc's XTUBE CM is that the electron beam is always incident on the center of the anode. In order to model different positions of the electron beam along the 70 cm long anode therefore required a multi-step process. First we modified the incident angle of the electron beam. We then scored photons in a phase space file directly below the x-ray tube geometry and translated each phase space file to the corresponding position for each angle. Phase space manipulation was performed using Python. The phase space files were then simulated through the remaining CMs of the KVAT model each of which was simulated with BLOCK CMs. The first of these BLOCKs is a 0.79 cm thick copper housing which also acts as a primary collimator. The collimator opening is 75 cm long and 1.3 cm wide. Second, is a 0.3 mm thick stainless steel filter. Third is a 2.2 mm thick layer of water, which acts as minor additional filtration and is part of the water cooling system. Fourth, there is another stainless steel filter with a thickness of 0.4 mm. Fifth and lastly, is a stainless steel housing and primary collimator with a thickness of 0.5 cm. The length of this opening is 75 cm and the width is 1.3 cm. The converging collimator is placed below the stainless steel housing. The collimator was modeled with ten BLOCK CMs composed of antimonial lead each with a thickness of 0.6 cm. The rectangular apertures were defined by four vertices at the top of each section of the collimator. The apertures of the converging collimator were designed using raytracing methods in MATLAB (The Mathworks, Natick, MA). Each aperture was designed such that the width of each beamlet at isocenter would be a certain size. For example, for a collimator designed to treat

4 cm PTVs the width of each beamlet at isocenter is 4 cm. Since the apertures are square, a full 360-degree rotation produces an irradiated volume which is roughly cylindrical with a diameter equal to the width of each beamlet. After simulation through the entire KVAT system geometry, the photons were scored in phase space files at the bottom of the collimator for calculation in DOSXYZnrc[24]. The mean energy of the beamlets was 86 keV. A minimum of 200,000 photons was scored in the phase space file of each beamlet.

Energy transportation cutoff parameters were set to 0.521 MeV for electrons (including the 0.511 MeV rest energy of an electron) and 0.01 MeV for photons in all BEAMnrc simulations. In all DOSXYZnrc simulations the electron cutoff value was set to 0.811 MeV while the photon cutoff value was set to 0.01 MeV. All simulations used XCOM cross-section data. To reduce BEAMnrc calculation time, variance reduction techniques were used. Uniform bremsstrahlung splitting with a splitting factor of 200 was used. Additionally, cross-section enhancement was used for tungsten with an enhancement factor of 1 and an enhancement constant of 200[39]. Russian roulette was used for both techniques. All simulations were run on a Linux computer with 64 AMD Opteron 6738 cores. BEAMnrc simulations required approximately 2800 CPU hours and DOSXYZnrc simulations required approximately 2500 CPU hours per beamlet set for a single sub-volume.

6.2.3 Patient Studies

The objective of this work was to evaluate the limitations of KVAT treatment plans of clinical tumor volumes. To this end, 3 patients who received stereotactic ablative radiotherapy (SABR) for lung tumors at the VICC were chosen as study cases. The choice of real clinical patients allowed us to compare KVAT to clinical MV RT. Patients were scanned with a 4DCT and PTV volumes were created by adding a uniform 5 mm margin to the contoured IGTV. The first lung patient had an 18 cc PTV located centrally in the left lung. The second lung patient had

a 43 cc PTV located directly in close proximity to the rib cage of the left lung. Lastly, the third patient had an 18 cc PTV located directly next to the heart in the right lung. In order to achieve coverage over the entire PTV volume, a number of sub-volumes with a different isocenter were defined for each patient. This method of RT delivery is similar to the method used in Gamma Knife treatments[76]. Despite the fact that the irradiated volumes of the KVAT system were approximately cylindrical, spherical sub-volumes were defined for simplicity in the treatment planning process. The PTV of patient 1 was covered by three sub-volumes each with a diameter of 3 cm. The PTV of patient 2 was covered by three sub-volumes with diameters of 4 cm. Lastly, the PTV of patient 3 was covered by a single 4-cm diameter sub-volume. Each of the sub-volumes were planned individually with a 360-degree arc of the KVAT system.

6.2.4 Dose Constraints and Dose Prescription

Since an established standard for KVAT dose constraints to OARs and dose prescription does not exist, we chose to use the same dose prescription of 12 Gy/fx over four fractions used by the clinical MV SABR plans. Dose constraints (Table 6.1) were taken from the AAPM's Task Group 101 report on stereotactic body radiation therapy[77]. It should be noted that the values in the report were for 3 and 5 fraction treatments. The values in Table 6.1 have therefore been linearly interpolated to estimate values for 4 fraction treatments. The standard method of dose prescription used in MV RT prescribes the dose delivered to 90-95% of the PTV. For this study we chose to prescribe dose to 90% of the PTV. The same prescription volume will be used for MV SABR treatments.

Table 6.1 – Dose constraints on organs-at-risk from TG 101.

Organ	Dose Constraint (Gy/fx)	Volume (cc)
Heart	7.2	15
Esophagus	7.7	5
Spinal Cord	5.3	0.35
Great Vessels	11.2	10
Lungs	2.7, 2.9	1500, 1000
Ribs	8.8	1
Skin	8.6	10

6.2.5 Patient KVAT Dose Calculation

All KVAT dose calculations were performed in DOSXYZnrc and dose-to-medium was reported. Calculated dose values of Gy/incident particle were converted to Gy/minute using a conversion factor of 60s∗0.2A/1.6E-19C. Patient CT data was converted into .egsphant phantom files with 2.5 × 2.5 × 2.5 mm^3 voxels using the Radify (LifeLine Software, Inc., Austin, TX, USA) treatment planning application. Materials of skeletal muscle, air, inflated lung and ribs (2-6) were used in each patient and the compositions of each material were taken from the International Commission on Radiological Protection (ICRP) data[47]. A clinical calibration curve was used to convert Hounsfield units (HU) to mass densities. The HU ranges of each material were: air (-1000:-950), inflated lung (-950:-300), muscle (-300:100) and ribs (2-6) (100:2000). Each PTV sub-volume was treated with a 360-degree arc and stepped through in 5-degree increments. At each treatment position the dose of 70 individual beamlets was calculated. The error in the 20 highest dose voxels was no more than 2.5% for all dose simulations.

The sets of beamlets for each PTV sub-volume were inversely optimized using the McGill optimization framework (McO)[31]. The McO employs a column generation based optimization algorithm to optimize the weighting of each beamlet delivered to a single sub-volume. The optimization process was guided by dose-volume constraints defined for the PTV and OARs. After optimization was performed for each sub-volume, the resulting .3ddose files were combined using MATLAB[78] to produce the final dose distribution.

6.2.6 Patient SABR Dose Calculation

The SABR plans of each patient were planned by the RT department of the VICC and were delivered by a Varian True-Beam™ linac using 6 MV photons. Each SABR plan consisted of one clockwise 200-degree arc and one counter-clockwise 200-degree arc. The SABR plans were calculated directly from the Eclipse™ treatment planning system using VMC++ and in-house software which had been previously validated[21,44,65]. VMC++ has been shown to agree with EGSnrc to within 1%[45]. The same clinical HU-to-mass density curve we employed previously was used for these calculations. Similarly, the dose calculation grid had voxels of 2.5 × 2.5 × 2.5 mm^3. The highest statistical uncertainty of the SABR dose calculations was 1% and dose-to-medium was reported in the .3ddose files produced.

6.2.7 Data Analysis

Dose distributions were visualized using MATLAB directly from .3ddose and .egsphant files. DVH data was calculated using Radify and then exported to and visualized by MATLAB. Mean integral body dose was calculated from DVH data in MATLAB. Conformity index (CI) values were calculated using DVH data in MATLAB according to the definition in RTOG 62[79]. Using this definition of CI, smaller values indicate a more conformal treatment plan. In this study we calculated CI_{50}, defined as the ratio of the volume encompassed by the 50% (of the prescription dose) isodose line and the volume of the PTV. KVAT treatment times were

calculated with Python using data files containing the beam-on time of each beamlet which were produced in the optimization process.

6.3 Results

Figure 6.2a shows the axial, sagittal and coronal KVAT dose distributions for patient 1 while Figure 6.2b shows the results for SABR. Figure 6.2c and 6.2d present the DVHs for both KVAT and SABR. All OARs are within the prescribed dose constraints for both plans (see Table 6.2). The planned dose to OAR volumes relevant to dose constraints are summarized in Table 6.2. Values of planned mean dose to OARs are presented in Table 6.3. The planned mean body dose was 0.7 Gy and 0.3 Gy for KVAT and SABR, respectively. KVAT and SABR CI_{50} values were 7.4 and 4.1, respectively. The planned KVAT treatment time for a 12 Gy fraction was 49 minutes for 3 sub-volumes.

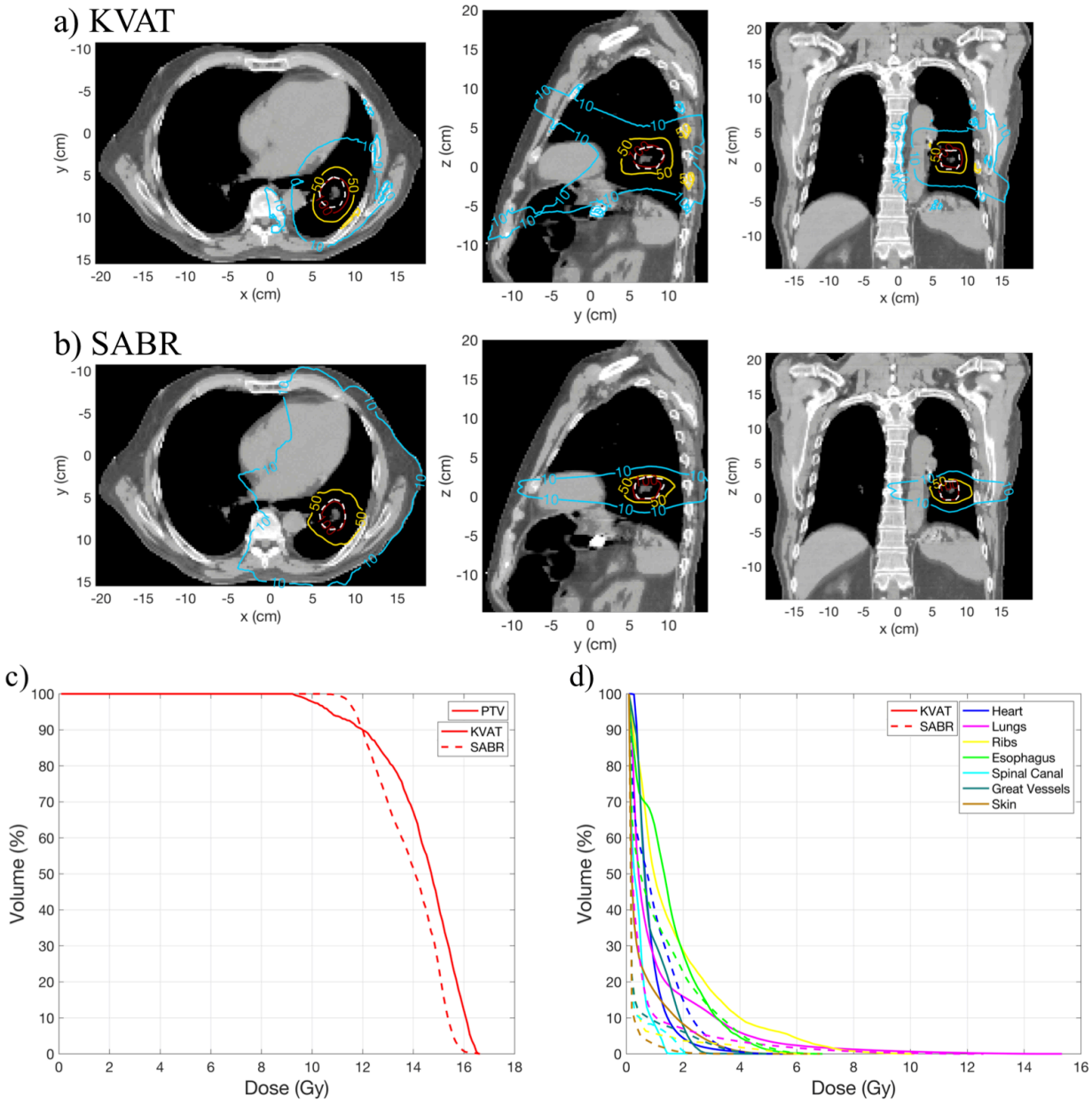

Figure 6.2 – (a) Axial, sagittal and coronal dose distributions for patient 1 for KVAT and (b) SABR. Isodose lines shown are for 12 (red), 6 (yellow), and 1.2 (blue) Gy. The dashed line indicates the PTV in the dose distributions. (c) PTV DVH and (d) OAR DVH of the KVAT and SABR plans of patient 1. A dose of 12 Gy/fx was prescribed to 90% of the PTV.

Figure 6.3a illustrates the axial, sagittal and coronal KVAT dose distributions for patient 2 and Figure 6.3b shows the SABR dose distributions. Figure 6.3c and 6.3d show the DVHs for

the KVAT and SABR plans of patient 2. All OARs are within dose constraints for both plans with the exception of the ribs in the KVAT plan which had a planned dose of 22.2 Gy/fx to 1 cc (Table 6.2). The planned mean body dose was 1.0 Gy and 0.4 Gy for KVAT and SABR, respectively. CI_{50} values for KVAT and SABR plans were 11.2 and 3.5, respectively. The planned KVAT treatment time for a 12 Gy fraction was 65 minutes for 3 sub-volumes.

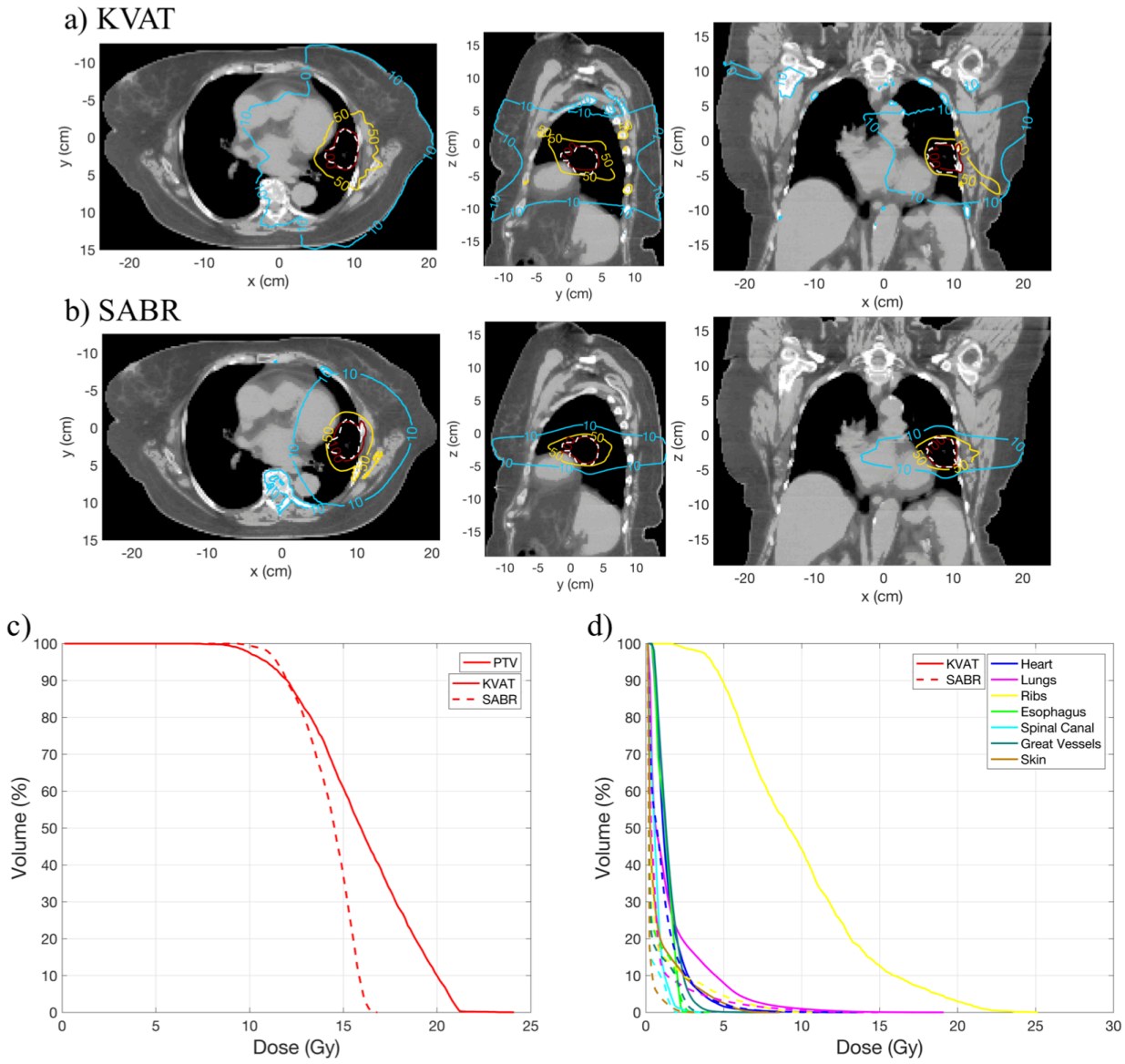

Figure 6.3 – (a) Axial, sagittal and coronal dose distributions for patient 2 for KVAT and (b) SABR. Isodose lines shown are for 12 (red), 6 (yellow), and 1.2 (blue) Gy. The dashed line indicates the PTV in the dose distributions. (c) PTV DVH and (d) OAR DVH of the KVAT and SABR plans of patient 1. A dose of 12 Gy/fx was prescribed to 90% of the PTV.

Figure 6.4a illustrates the axial, sagittal and coronal KVAT dose distributions for patient 3 and Figure 6.4b shows the SABR dose distributions. Figure 6.4c and 6.4d depict the DVH for the KVAT and SABR plans of patient 3. All OARs are within dose constraints for both plans

(Table 6.2). The planned mean body dose was 0.9 Gy and 0.3 Gy for KVAT and SABR, respectively. KVAT and SABR values CI_{50} metrics were 12.0 and 4.5, respectively. The planned KVAT treatment time for a 12 Gy fraction was 26 minutes for the single sub-volume.

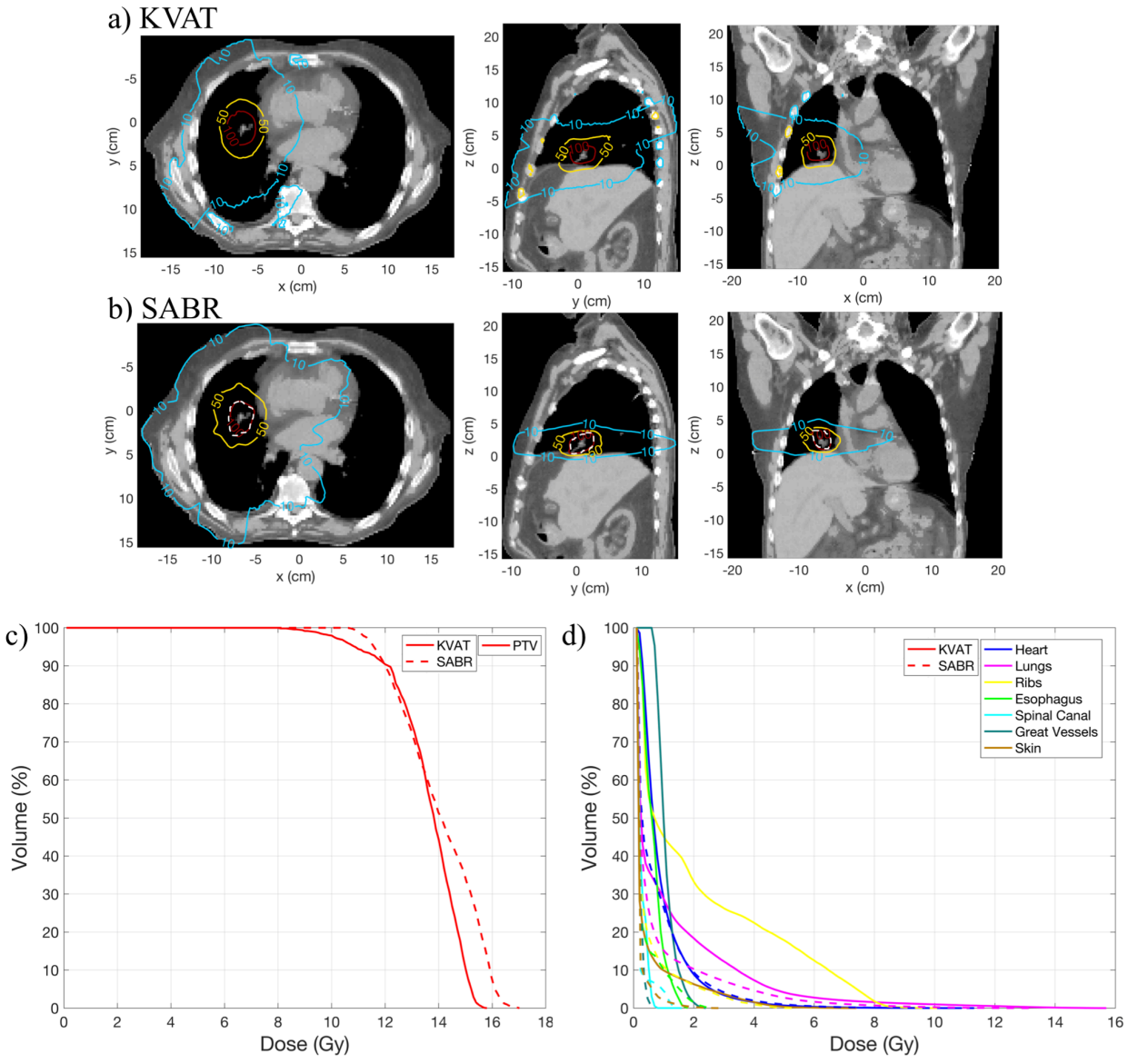

Figure 6.4 – (a) Axial, sagittal and coronal dose distributions for patient 3 for KVAT and (b) SABR. Isodose lines shown are for 12 (red), 6 (yellow), and 1.2 (blue) Gy. The dashed line indicates the PTV in the dose distributions. (c) PTV DVH and (d) OAR DVH of the KVAT and SABR plans of patient 1. A dose of 12 Gy/fx was prescribed to 90% of the PTV.

Table 6.2 – KVAT and SABR doses to volumes specified by dose-constraints planned for organs-at-risk for each lung cancer patient.

Organ	Dose Constraint (Gy/fx)	Patient 1 KVAT Dose (Gy/fx)	Patient 1 SABR Dose (Gy/fx)	Patient 2 KVAT Dose (Gy/fx)	Patient 2 SABR Dose (Gy/fx)	Patient 3 KVAT Dose (Gy/fx)	Patient 3 SABR Dose (Gy/fx)
Heart	7.2	3.4	3.4	5.5	6.1	4.3	4.7
Esophagus	7.7	3.7	3.9	2.0	1.9	1.1	0.8
Spinal Cord	5.3	1.4	2.0	2.6	1.8	0.7	1.3
Great Vessels	11.2	2.2	2.3	3.0	2.5	1.1	0.2
Lungs (1000cc)	2.9	0.8	0.4	1.1	0.5	0.8	0.4
Lungs (1500cc)	2.7	0.5	0.2	0.5	0.2	0.3	0.2
Ribs	8.8	8.8	5.5	22.2	8.5	8.7	4.6
Skin	8.6	4.2	2.0	6.3	2.1	4.8	1.8

Table 6.3 – KVAT and SABR planned mean dose to organs-at-risk.

Organ	Patient 1 KVAT Mean Dose (Gy/fx)	Patient 1 SABR Mean Dose (Gy/fx)	Patient 2 KVAT Mean Dose (Gy/fx)	Patient 2 SABR Mean Dose (Gy/fx)	Patient 3 KVAT Mean Dose (Gy/fx)	Patient 3 SABR Mean Dose (Gy/fx)
Heart	0.8	0.9	1.4	1.1	0.9	0.7
Esophagus	1.5	1.1	1.2	0.5	0.6	0.3
Spinal Cord	0.4	0.2	0.6	0.3	0.2	0.2
Great Vessels	0.8	0.3	1.4	0.5	1.0	0.2
Lungs (1000cc)	1.1	0.6	1.5	0.7	1.3	0.7
Lungs (1500cc)	0.5	0.2	0.5	0.2	0.7	0.2
Ribs	1.6	0.3	9.8	0.8	2.0	0.4
Skin	0.5	0.2	1.1	0.2	0.4	0.2
Body	0.7	0.3	1.0	0.4	0.6	0.3

6.4 Discussion

The purpose of this work was to investigate the capability of the KVAT system to produce treatment plans that do not exceed dose constraints of OARs for clinical lung cancer patients. Each RT plan will be evaluated based on dose distributions, DVHs, conformity index and mean integral body dose.

6.4.1 Patient 1

All dose constraints for OARs were met in both KVAT and SABR plans for patient 1. From Figure 6.3 we can see that, in the axial plane, SABR had lower planned doses (~ 2 to 4 Gy) for a larger patient area in comparison to KVAT. However, the reverse was true for the sagittal and coronal planes. This pattern was present for patient 2 and 3 as well. Figure 6.2a and 6.2b indicates one difference between the KVAT and SABR treatments was the shoulder of the PTV, which was less prominent in KVAT and indicates that a smaller volume of the PTV has higher planned doses. Ribs had the largest mean dose difference between KVAT and SABR with values of 1.6 Gy/fx and 0.3 Gy/fx respectively. This increased rib dose was expected given the lower energy of kV photons and increased interactions by the photoelectric effect. Less prominent differences existed in the mean doses planned to the remaining OARs. The only organ with a higher SABR mean dose was the heart with a value of 0.9 Gy/fx in comparison to the KVAT value of 0.8 Gy/fx. The higher mean body dose delivered by KVAT is also expected given the lower penetration of kV photons and the larger patient area over which the photons are incident. Higher mean body dose is observed in all three patients. The KVAT plan was found to be less conformal than SABR with a CI_{50} KVAT value of 7.4 in comparison to the SABR value of 4.1 (a lower value indicates greater conformality). The two 200-degree arcs of the SABR plan would take approximately two minutes (assuming a dose rate of 600 MU/min, due to heavy modulation). The planned KVAT treatment time of 49 minutes was longer than SABR but this is

expected given the lower output of x-ray tubes in comparison to linacs and the collimation used by the KVAT system. While KVAT treatment times will always be longer than MV treatment times, they will be dependent on the dose prescription used in treatment. The choice of 12 Gy/fx in this work was primarily chosen because of the comparison to SABR plans. There is no precedence for KVAT dose prescription and a lower dose prescription would result in lower treatment times.

6.4.2 Patient 2

With the exception of the ribs in the KVAT plan, all dose constraints are met for patient 2's KVAT and SABR plans. Figure 6.3c shows a much shallower PTV DVH for KVAT in comparison to SABR. This was likely caused by an increased weighting of the beamlets coming from the left of the patient due to both the location of the PTV (closer to the left side of the patient) as well as the larger than average thickness (44 cm across the chest) of the patient. Our previous work showed that a non-360 degree KVAT arc results in dose distributions with a shallower DVH for the PTV. The increased weighting of the left-sided beamlets was a contributor to the high levels of rib dose observed. The location of the PTV directly next to the rib cage made it very difficult to plan beamlets that did not pass through the ribs closest to the PTV. For other patients the dose to ribs was reduced by weighting the beamlets at all angles more evenly, however the large size of patient 2 made the beamlets from the right side of the patient less effective due to the lower penetrating power of kV photons. All of the remaining organs had higher mean doses in the KVAT plan with the next largest difference being 0.9 Gy/fx for the great vessels and skin. The KVAT CI_{50} value of 11.2 indicates a less conformal treatment than SABR which had a CI_{50} value of 3.5. The planned treatment time was the highest of the 3 patients with a total value of 65 minutes for all three sub-volumes. Based strictly on the guidelines of dose-constraints the KVAT plan be may not be recommended and serves as an

example of what clinical situations might be unsuitable for KVAT treatment. However, the context of the patient's treatment should also be taken into account. For instance, if this was for a palliative case and the patient was suffering from bone pain due to the tumor's invasion of the rib cage, such a treatment may improve the patient's condition despite the increased probability of a rib fracture. Moreover, it is possible that the enhanced kV cross-section of the calcified cortical bone absorbed most of the dose and spared the marrow. MV beams are less sensitive to organ composition, and presumably yield higher bone marrow dose, which might significantly weaken osseous structural integrity at lower values of total absorbed bone dose. Furthermore, in a developing country, if KVAT was an option available for RT the benefits of treatment may outweigh the risk of a radiation induced rib fracture.

6.4.3 Patient 3

Dose constraints for all OARs were met by both the KVAT and SABR plan for patient 3. Once again we see the shoulder of the of the PTV DVH is lower for KVAT in comparison to SABR. For patient 3 all OARs had higher values of planned dose in the KVAT plan compared to the SABR plan. The largest difference was observed for the ribs which had a mean dose of 2.0 Gy/fx and 0.4 Gy/fx in the KVAT and SABR plan, respectively. The second largest difference was 1.0 Gy/fx for the great vessels. KVAT was less conformal with a CI_{50} value of 12.2 as compared to the SABR value of 4.5. The KVAT treatment time for patient 3 was 26 minutes for a planned fraction of 12 Gy. The increased treatment time for patient 3 (26 minutes for a single sub-volume) is due to the more stringent constraints placed on the optimization process. As can be seen by the PTV DVH the coverage of the PTV is improved in patient 3 in comparison to the other patients and the consequence of this is increased beam-on time.

6.4.4 Additional Comments

Based on the treatment times of each treatment plan the average dose rate per sub-PTV of the KVAT system range from 0.46 cGy/min to 66 cGy/min.

An additional concern that will affect treatment times will be the use of gating. The margins around the IGTV used in each plan were 5 mm which is adequate for using a breath-hold technique during lung radiotherapy[15]. The treatment times required to deliver 12 Gy may be too long for a patient to undergo such a treatment. In such cases the dose prescription may have to be reduced. However, as mentioned previously, there is no precedent for dose prescription in KVAT and statements of necessary dose prescriptions would require much more research. The dose of 12 Gy/fx was chosen in this work solely due to the comparison to SABR treatment plans which used this dose prescription.

6.5 Conclusions

In this work we have used the BEAMnrc and DOSXYZnrc packages of EGSnrc along with the McO optimization framework to simulate and inversely optimize KVAT treatment plans of three lung cancer patients. VMC++ was used to simulate the clinical SABR plans delivered to each patient for a point of comparison. All OARs were within dose constraints taken from the AAPM Task Group 101 report on stereotactic body radiotherapy with the exception of the rib dose of patient 2. Due to the high rib dose planned for patient 2, lung tumors located directly adjacent to the rib cage will present difficult treatment situations for KVAT. However, the results of patient 1 and 3 indicate the ability of our system to treat certain lung tumor sites without exceeding dose constraints on critical organs. Further work should be performed to assess the ability of the KVAT system to treat additional cancer disease locations such as bone metastases and breast lesions.

7. Experimental Demonstration of the Skin Sparing Ability of a Proof-of-Principle Kilovoltage Arc Therapy System

In preparation for submission to Medical Physics

Introductory Remarks

All the previous work of this PhD project concerned simulations of KVAT. Simulations are incredibly helpful as a means of determining whether a system will work before it has been constructed and as a guide in the design process. Furthermore, once a system has been constructed a model can be used to test the system's capabilities. Before the start of my project work was done on an existing kilovoltage source, which employed the same principle of converging beamlets as KVAT. A MC model of this system was created and validated against experimental measurements of the system's dosimetric output. This work was thought to be strong enough to serve as the foundation of the design and evaluation of the KVAT system's capabilities. Ultimately, however, this previous system was not intended for therapy and differed in design from the KVAT system. Therefore, the logical last step of my project was the experimental validation of the ability of a simple, proof-of-principle KVAT system to produce focused dose at depth while sparing healthy tissues. To show this we used a tabletop kV x-ray system and a simple collimator employing the principle of multiple converging beamlets.

7.1. Introduction

The standard of clinical external beam radiation therapy (RT) is the delivery of megavoltage (MV) x-rays from a medical linear accelerator (linac). While MV RT is an effective means of cancer treatment, the high cost of the required technology and infrastructure results in unequal access to cancer RT care between high-income and low- and middle-income countries[4,5]. Lower energy kilovoltage (kV) x-ray systems, while requiring less expensive technology to produce and less costly shielding requirements, are traditionally unsuitable for the treatment of

deep-seated cancers due to their lack of penetration and skin-sparing ability. In this work we present experimental evidence of the skin-sparing ability of a proof-of-principle kilovoltage (kV) arc therapy system (KVAT) which uses a specially designed collimator, which serves to reduce skin dose, and compare measured phantom data to Monte Carlo (MC) simulations.

Dosimetry of kV x-rays, which are primarily used for imaging purposes given that superficial orthovoltage therapy is not frequently performed in clinics, can be performed using ionization chambers, thermoluminiscent dosimeters, radiographic and radiochromic films[80]. While ionization chambers could in principle be used to measure the dose from our KVAT system, they would not be ideal for measuring sharp dose gradients and a specialized phantom would be required to create an approximation of a two-dimensional dose distribution. In contrast, radiochromic film is inherently two-dimensional and has high enough resolution to measure sharp dose gradients. For these reasons radiochromic films were chosen to measure dose for this study.

The primary objective of this work was to demonstrate experimental evidence of the skin-sparing ability of a simple prototype kilovoltage x-ray arc therapy (KVAT) system. The secondary objective was to validate a Monte Carlo (MC) model of the prototype system. Our group has previously investigated two separate MC models (transmission and reflection target based systems) of a KVAT system, both of which employed the same fundamental idea of using an array of converging beamlets in conjunction with arc-therapy to achieve a skin-sparing effect while delivering clinically-relevant dose to a deep-seated treatment volume[1,57]. Previous work on KVAT includes MC simulations of cylindrical water phantoms demonstrating skin-sparing effects[57], inversely optimized and MC generated treatment plans for breast, lung and prostate patients using idealized, spherical treatment volumes[1] and, most recently, the generation of MC

simulated and inversely optimized treatment plans for lung cancer patients with real clinically contoured treatment volumes[81]. While further investigative work on the treatment potential of KVAT was of interest, it was practical to first experimentally demonstrate the fundamental skin-sparing ability of KVAT.

In this work we used a tabletop x-ray system along with a custom-built brass collimator to create a linear array of 5 converging beamlets. The array of beamlets was used to irradiate a cylindrical high-density polyethylene (HDPE) phantom and a rectangular solid water phantom, which were rotated on a rotating stage during irradiation. Dose was measured by inserting radiochromic film into each phantom to record two-dimensional dose distributions. Measured values of dose from the irradiated films were compared to Monte Carlo simulated dose distributions. The quality of dose distributions was analysed in terms of target-to-skin ratio, full-width at half maximum (FWHM), penumbra size and dose output.

7.2. Materials and Methods

7.2.1 Tabletop X-Ray System

The tabletop x-ray system (Figure 7.1 and 7.2) consisted of a Comet MXR-160/22 (Comet AG, Herengasse, Switzerland) x-ray tube mounted on a vertical translation stage (IMS300LM-S, Newport Corp., Irvine, USA). The vertical translation stage holding the x-ray tube was mounted on a horizontal translation stage (IMS600LM-S, Newport Corp., Irvine, USA). The x-ray tube's horizontal translation stage was able to move towards and away from the phantom position. The phantoms were placed on a rotating stage (RVS80CC, Newport Corp., Irvine, USA). The horizontal stage has a translation range of 600 mm and a positioning accuracy of 7.5 μm. The vertical stage has a movement range of 300 mm with a positioning accuracy of 4.5 μm. The rotation stage can rotate fully through 360 degrees with an accuracy of 10 milli-degrees.

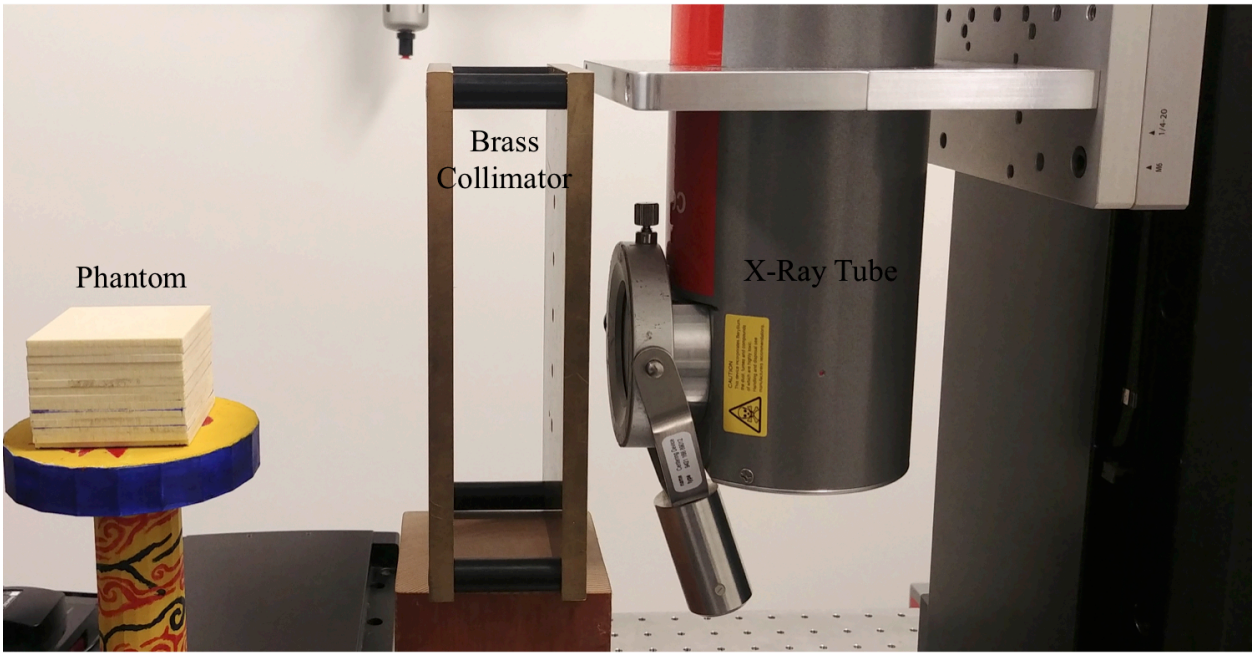

Figure 7.1 – Photograph of the tabletop x-ray tube experimental setup.

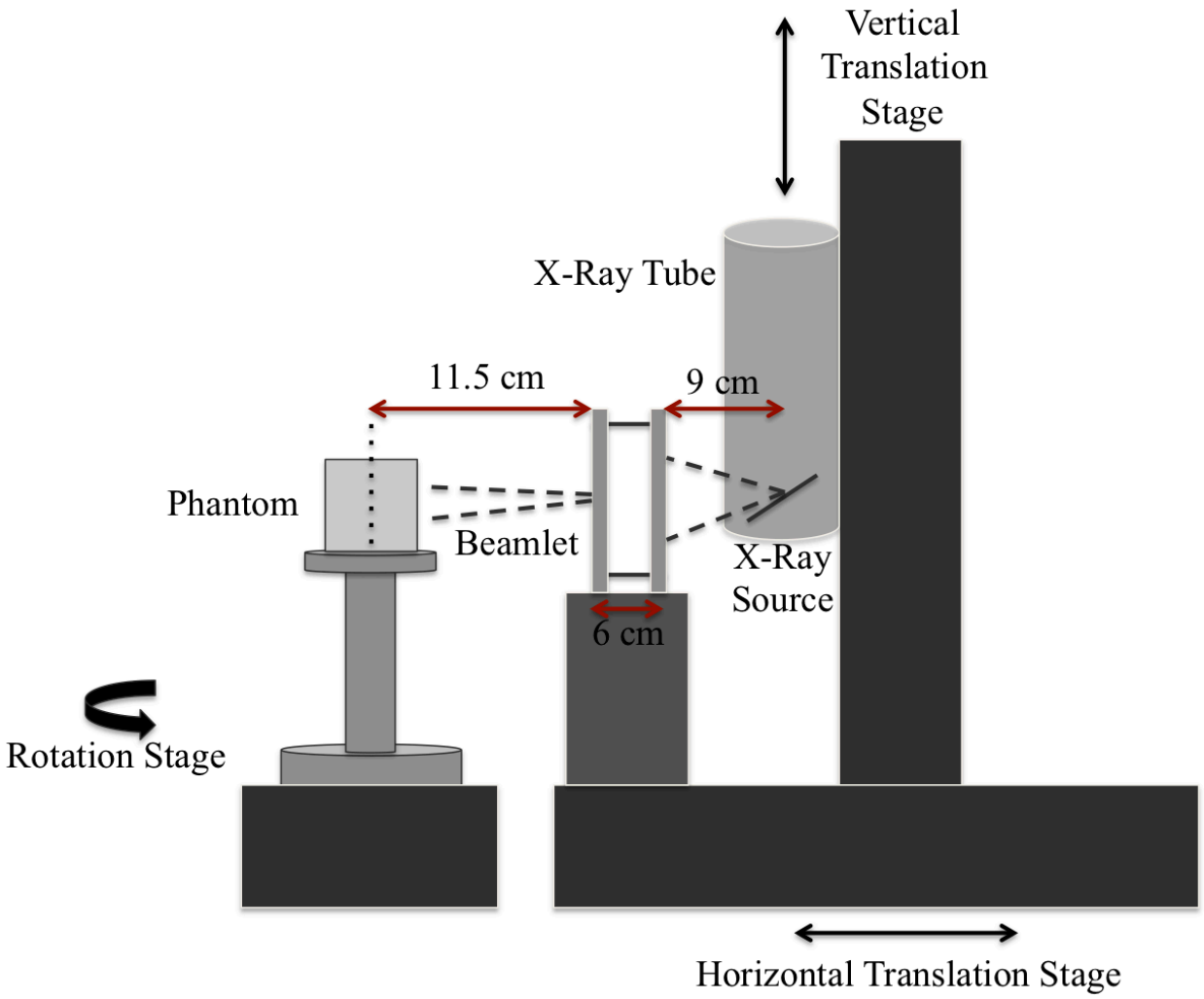

Figure 7.2 – Diagram of the tabletop x-ray tube experimental setup.

7.2.2 Collimator Design

The brass collimator (Figure 7.3) consisted of two 20 cm × 10 cm brass slabs each with a thickness of 0.93 cm. The two brass slabs were separated by plastic spacers to space the brass slabs ~4 cm apart, which created a distance of 6 cm between the outer faces of the collimator. In each brass slab, five holes were drilled as the apertures of the five beamlets. The location and diameter of each aperture were determined by projecting a point source located 9 cm behind the x-ray tube face of the collimator to a 2 cm diameter circular target centered at isocenter. The isocenter was located at a distance of 11.5 cm from the bottom of the collimator for a total

source-to-axis distance (SAD) of 26.5 cm. The diameters of the apertures in both slabs were then calculated as the necessary width to create 2 cm diameter beamlets at isocenter. The x-ray tube side had apertures with diameters of 6 mm while the phantom side had apertures with diameters of 10 mm. The source position was translated to five different points along the long axis of the collimator. The position of each aperture was determined by tracing the position of the isocenter back to each of the five source locations. The distance between the centers of each aperture were 2.33 cm and 1.67 cm on the x-ray tube side and phantom side, respectively.

Figure 7.3 – Photograph of the custom-built converging brass collimator showing the a) x-ray tube side b) phantom side and c) cross-sectional view.

7.2.3 Film Calibration

EBT3 Gafchromic film (ISP, Wayne, NJ) was calibrated according to TG 55[30]. First, the dose rate of the x-ray system was determined using the dose-in-phantom method of TG 61[29]. A 5 cm thick, 30 cm × 30 cm slab of solid water was used as backscatter and a farmer ionization chamber (PTW, Freiburg, Germany) was placed at the center of the beam at a depth of 2 cm in solid water. The ionization chamber and electrometer (Unidos) used were calibrated by the National Research Council of Canada (NRC) standards laboratory for kilovoltage energies. The source-to-surface distance (SSD) used was 30 cm and a 3 cm × 4 cm collimator was mounted on the x-ray tube with 1 mm of Al filtration. The tube energy was set to 160 kVp with a 5.5 mm diameter circular focal spot. The ionization chamber was irradiated for 1 minute at 13 mA and charge was collected by the electrometer. Three readings were taken and averaged to determine the dose rate. Seventeen films were then individually placed on a 5 cm thick slab of solid water and covered by a 2 cm thick slab of solid water. The films were then irradiated to seventeen doses between 0.2 and 40 Gy. In order to measure a depth dose curve, a film was placed parallel to the beam axis in the centre of two 5-cm thick slabs of solid water phantom. A depth dose curve was measured to serve as a means to validate the MC model of the x-ray tube. For the depth dose irradiation the surface of the solid water was placed 5 cm from the 3 cm × 4 cm collimator. The films were scanned 24 hours after irradiation using a flatbed scanner (Expression 10000 XL, Epson, Suwa, Japan) scanner and the red channel values and their corresponding dose values were fit in MATLAB[78] (The Mathworks, Natick, USA) to produce the dose calibration curve. The depth-dose film was scanned and analysed in MATLAB.

7.2.4 Rectangular and Cylindrical Phantom

The rectangular phantom consisted of fourteen 3 mm thick, 5.8 cm × 5.8 cm slabs of solid water. Three 5.8 cm × 5.8 cm pieces of film were placed in the center of the phantom and at

positions 6 mm away from the center of the phantom. The cylindrical phantom consisted of four 2.5 cm thick circular slabs of TIVAR 1000 material with a diameter of 20 cm. A 20 cm diameter laser-cut film was placed in the center of the cylindrical phantom. Additional films were not used in the cylindrical phantom due to the large thickness of the slabs, which would have placed the films in a region of dose below the sensitivity of the films.

7.2.5 Phantom KVAT Irradiations

For the KVAT irradiation experiments, a 1 cm × 4 cm secondary lead collimator was used along with 1 mm of aluminum filtration. The x-ray tube side of the brass collimator was a distance of 9 cm from the x-ray tube source and the phantom side of the brass collimator was a distance of 11.5 cm from the rotation axis of the rotation stage for a total SAD of 26.5 cm (Figure 7.2). The brass collimator was placed on a wood block in order to position the center of the central aperture with the vertical center of the phantoms (Figure 7.2). Changing the vertical position of the x-ray tube with respect to the collimator produced each of the 5 beamlets. The vertical position of the x-ray tube used to produce each beamlet was determined first by maximizing the ionization chamber reading directly in front of each aperture on the phantom side of the brass collimator. Small modifications of the vertical x-ray tube positions were then made using the rectangular phantom and films to ensure the irradiated region was centered on the rotation axis.

The phantoms were irradiated with each of the 5 beamlets using 160 kVp tube voltage. Each beamlet was used individually so a total of 5 irradiations were used for each phantom. During each beamlet irradiation the phantom was rotated a full 360 degrees over the course of the irradiation time. Irradiation times were 90, 45, 30, 45 and 90 seconds for the first, second, third (central), fourth and fifth beamlets, respectively for the rectangular solid water phantom. For the cylindrical Tivar phantom, irradiation times were 180, 90, 60, 90 and 180 seconds for the

first, second, third (central), fourth and fifth beamlets, respectively. Tube current was set at 18.75 mA and 9.375 mA for the solid water phantom and cylinder phantom, respectively. The irradiation times of the cylindrical phantom were scaled up approximately from the 160 kVp depth dose curve in order to estimate the irradiation time an ensure an adequate level of dose for the sensitivity of the film. The irradiated films were then scanned 24 hours after irradiation and converted into two-dimensional dose maps using the previously calculated calibration curve and MATLAB.

7.2.6 Monte Carlo Simulations

Simulation of the x-ray source was performed using BEAMnrc[23] according to the specifications of the Comet MXR-160/22 x-ray tube. Monoenergetic 160 keV electrons were used as the incident beam in each simulation. The diameter of the incident electron beam was 5.5 mm. The x-ray tube was modeled as an "XTUBE" component module with a tungsten anode at a 20-degree angle. The beryllium filter was modeled as a "SLAB" component module with a thickness of 0.8 mm. The primary conical collimator of the x-ray tube was modeled as a "CONS3R" made of brass. The secondary collimator was modeled as a "BLOCK" component module made of lead. The added aluminum filter was modeled as a "SLAB" component module with a thickness of 1 mm. A phase space file was scored at the exit of the x-ray tube. This phase space file was then used to simulate the collimation of beam. Different vertical positions of the x-ray tube were simulated by vertically translating the original x-ray tube phase space file to 5 positions. At each of the 5 positions a separate beamlet phase space file was produced. The custom brass collimator was modeled as two "BLOCK" component modules each with a thickness of 0.93 cm, lengths of 20 cm and widths of 10 cm. The supports were modeled using a "BLOCK" component module with a thickness of 4.14 cm for a total collimator thickness of 6 cm. The plastic supports were only present along the perimeter of the brass slabs and had a wall

thickness of 1 cm. The rest of the support section was modeled as air. The collimator apertures were modeled as 20-sided polygons. The diameter of the x-ray tube side apertures was 6 mm and the diameter of the phantom side apertures was 10 mm. The center of each aperture was such that the intersection of each x-ray beamlet was at isocenter a distance of 11.5 cm from the end of the collimator.

Five phase space files were independently generated, one for each beamlet, and then combined for dose calculations. Electron and photon cutoff energies were set at 0.521 MeV (including 0.511-MeV rest energy) and 0.01 MeV, respectively. XCOM cross-section data was used for all simulations. Variance reduction techniques were used to increase the speed of the simulations. Bremsstrahlung cross-section enhancement with an enhancement factor of 1 and enhancement constant of 200 was used. Additionally, uniform bremsstrahlung splitting with a splitting factor of 200 was used. For both techniques, Russian roulette was turned on. Each beamlet phase space had a minimum of 10^6 photons.

All dose calculations were performed in DOSXYZnrc[59]. Simulations of the x-ray tube's open beam were calculated using a large solid water phantom with dimensions of 30 cm × 30 cm × 30 cm with 5 mm × 5 mm × 5 mm voxels. The rectangular phantom was simulated as a 5.8 cm × 5.8 cm × 4.2 cm phantom composed solid water (1.035 g/cm^3) with a voxel size of 1 mm × 1 mm × 1 mm. The cylindrical phantom was not simulated as the TIVAR material was patented and unknown. The combined beamlet phase space file was used as the input to the dose calculations and was rotated 360-degrees around each phantom. The statistical uncertainty in the 20 highest dose voxels was less than 2% for all dose calculations. The calculated .3ddose files were analyzed using MATLAB. MC dose values of Gy/incident particle were converted into values of Gy using values of tube current and irradiation time.

7.2.7 Dosimetric Analysis

Five metrics were used to evaluate the measured dose distributions. Values of target-to-skin ratio, penumbra size, beam width and dose rate were calculated for the film and MC results of the rectangular solid water phantom and the film results of the cylindrical phantom. Target-to-skin ratio was calculated as the ratio of 50% of the maximum dose, D_{max}, of the central films (assumed to be the dose covering a hypothetical target volume) and the average dose over 1 mm of the peripheral region for the individual (bottom, central, top and cylindrical) dose profiles (see black ROI's in Figure 7.7b). Penumbra width was measured as the distance between 90% and 30% of the D_{max} for each profile. Beam width was calculated as the width of each profile at half of D_{max}. Dose rate was calculated as 50% of D_{max} in the central films only divided by the total irradiation time. Lastly, the maximum percentage difference between the entire film and MC dose profiles was calculated. All uncertainties in MC data were taken as the calculated values of uncertainty associated with each .3ddose file. For the film data an uncertainty of 3.2% was used[82]. It should be noted that the central film data of the rectangular phantom most directly represent the characterization of the KVAT dose distribution, as it is closest to the center of the dose distribution. The top and bottom films will be less representative of the dose distribution as its shape changes quickly with distance from the center. These extra films are primarily included to serve as extra data to validate the MC model.

7.3 Results

Figure 7.4 illustrates the MC simulated spectrum of the 160 kVp beam of the table top x-ray system. The mean energy of the beam is 57 keV. Figure 7.5 presents the absolute depth dose curves of the film and MC data for the 3 cm × 4 cm single beam irradiation. The maximum dose of 7.2 Gy in the MC data occurs at the surface of the phantom. The initial data points of the film data were untrustworthy as they were on the edge of the film and were thus excluded.

Figure 7.6 presents the two-dimensional film dose distributions of the rectangular solid water phantom for all three films and their corresponding dose profiles through the center of the irradiated volume. Additionally, the MC calculated dose profiles are plotted together with the film data for comparison. The highest central doses of 14 Gy were seen in the central film and MC data. Table 1 lists the calculated values of the maximum percent difference between the dose profiles of the film and MC data, the beam FWHM, beam penumbra, and the target-to-skin ratio for the film and MC data. A target-to-skin ratio of approximately 4 was calculated for the rectangular phantom film and MC data. Figure 7.7 shows the two-dimensional film dose distribution of the cylindrical phantom and its dose profile. The peripheral doses of the cylindrical phantom are much lower than those observed in the rectangular phantom. Table 2 lists the calculated values of FWHM, target-to-skin ratio and penumbra for the cylindrical phantom film data. The cylindrical phantom profile is sharper than in the rectangular phantom and has a higher target-to-skin ratio of 17.00. The dose rate for the rectangular and cylindrical phantom was 2.09 Gy/minute and 0.36 Gy/minute, respectively.

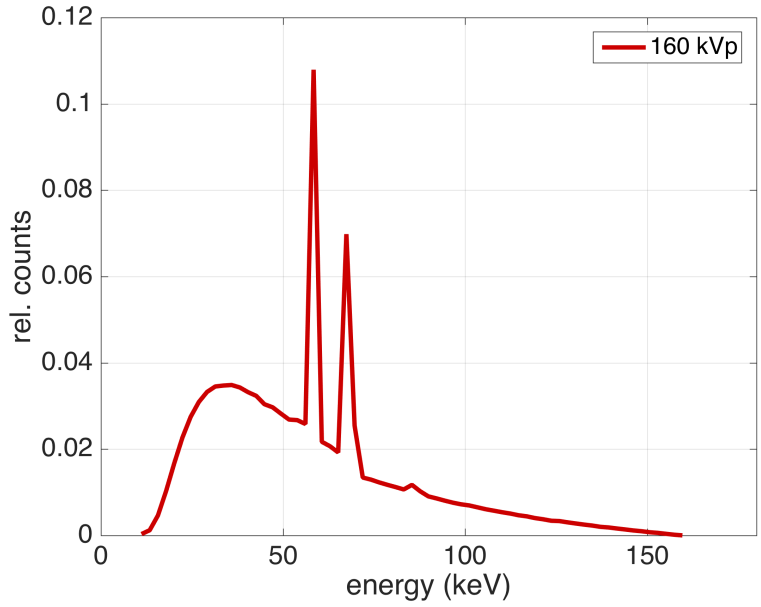

Figure 7.4 – Monte Carlo calculated spectrum of the 160-kVp beam of the tabletop x-ray system.

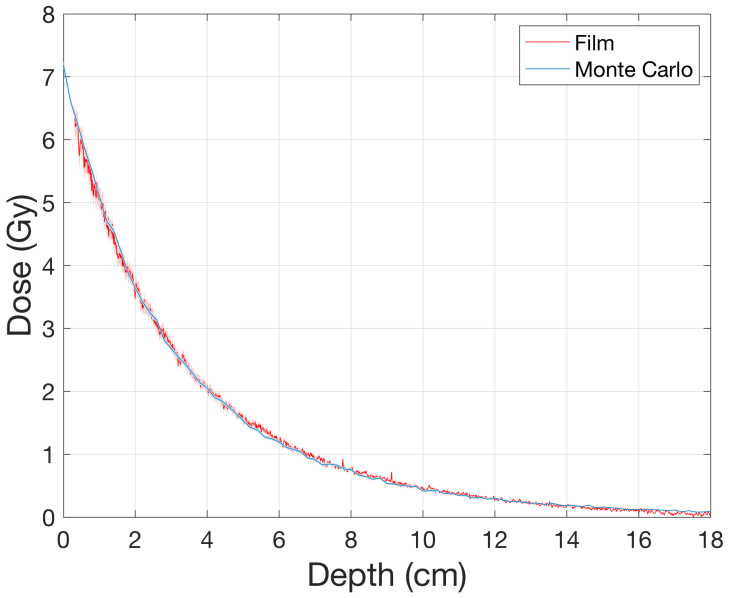

Figure 7.5 – Depth dose curves for the 3-cm × 4-cm 160kVp beam. The red curve represents the film data and the blue curve represents the Monte Carlo data. The shaded region around the curve is the uncertainty associated with each curve.

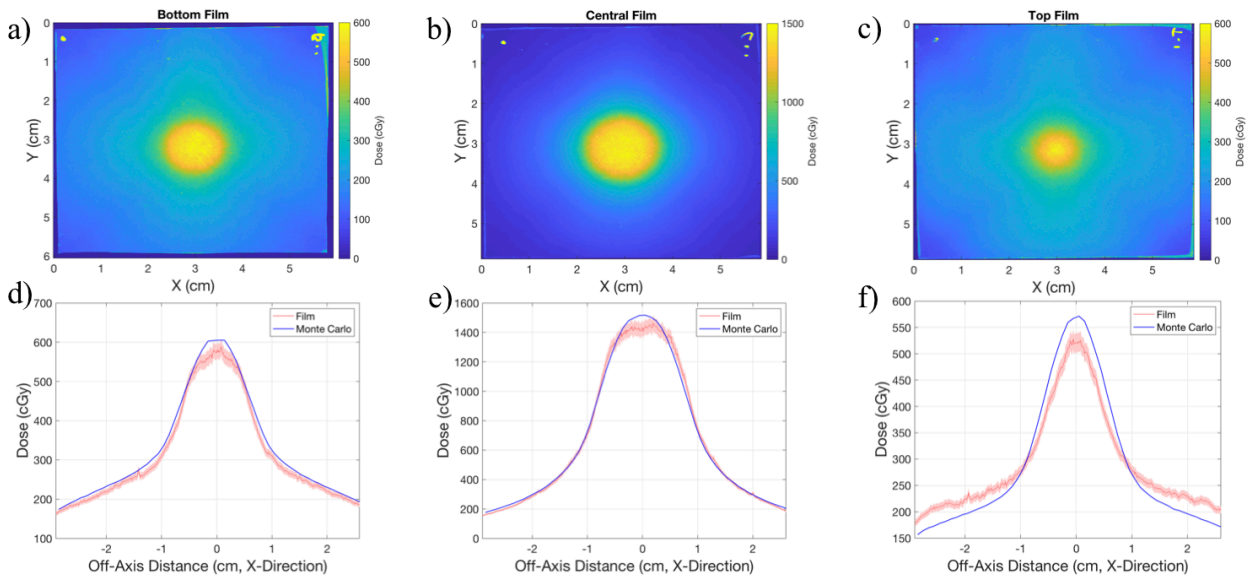

Figure 7.6 – Measured two-dimensional dose distributions of the rectangular phantom in the a) bottom, b) central and c) top film position. Measured film and calculated Monte Carlo dose profiles of the rectangular phantom in the d) bottom, e) central and f) top film position. The shaded region represents the error of the data.

Table 7.1 – Calculated values of FWHM, target-to-skin ratio, penumbra and maximum percent difference of the rectangular phantom data.

Data – Rectangular Solid Water Phantom	*FWHM (cm)*	*Target-to-Skin Ratio*	*Penumbra (cm)*	*Max % Profile Difference*
Bottom Film	2.30	4.10	2.35	6.46
Bottom Monte Carlo	2.15	4.02	2.36	-
Central Film	1.99	4.16	0.94	6.65
Central Monte Carlo	1.95	3.80	1.00	-
Top Film	2.29	3.75	2.72	10.02
Top Monte Carlo	1.89	4.51	2.25	-

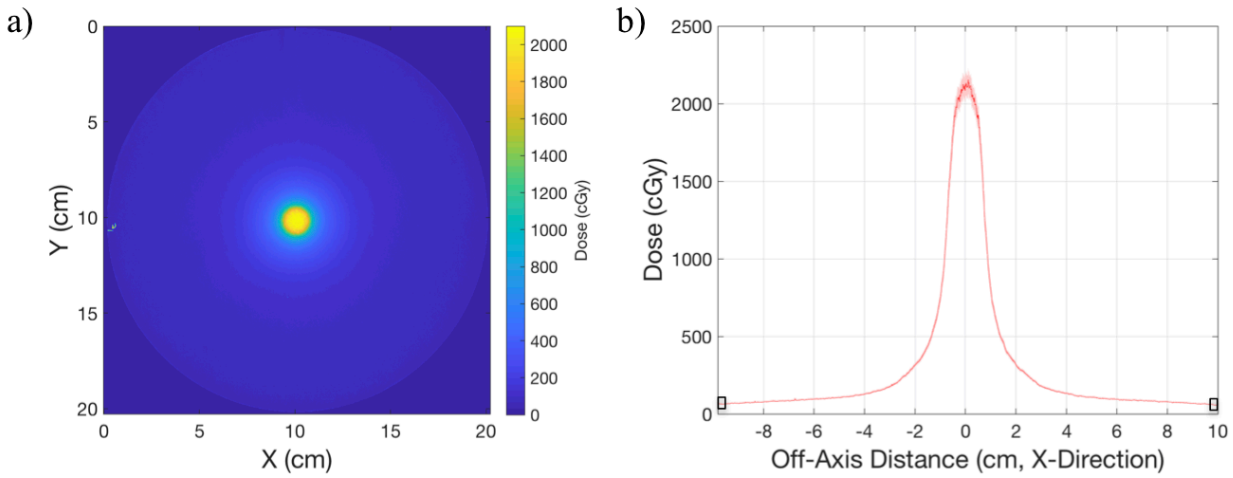

Figure 7.7 - a) Film two-dimensional dose distribution and b) dose profile of the cylindrical phantom. The shaded red region represents 3.5% uncertainty of the film profile data.

Table 7.2 – Calculated values of FWHM, target-to-skin ratio and penumbra of the cylindrical phantom irradiation.

Data – Cylindrical TIVAR Phantom	*FWHM (cm)*	*Target-to-Skin Ratio*	*Penumbra (cm)*
Film	1.64	17.00	0.67

7.4 Discussion

The measured and MC-calculated depth dose curves of the single 3 cm × 4 cm beam show good agreement with a maximum percent difference of 6.06 % and a mean percent difference of 1.49% (Figure 7.5).

The asymmetry of the top and bottom two-dimensional dose distributions in Figure 7.6 indicate the central film was not perfectly aligned to the center of the collimator. The highest target-to-skin ratio of 4.16 is observed in the central film of the rectangular phantom and overestimates the MC calculated value by 8.65%. The lowest target-to-skin ratio of 3.75 is observed in the top film profile. The largest percent difference between film and MC target-to-skin ratios is 20.3% for the top film. The lower values of target-to-skin ratio can also be visually observed in the top and bottom film dose distributions, which have higher dose levels outside of

the central dose region. This is expected due to the fact that the peripheral beamlets will form an ellipse when they intersect with the film planes and have a larger irradiated area. Furthermore, the peripheral beams contribute more to the top and bottom film dose distributions due to their position. The relative contribution of the peripheral and central beamlets to each dose distribution can also be seen in the calculated FWHM and penumbra values with the smallest values occurring in the central film. The smallest FWHM value was 1.99 cm for the central film and differs from the Monte Carlo value by 2.01%. The largest FWHM value was 2.30 cm for the bottom film and differs from the MC calculated value by 6.52%. The smallest penumbra value was 0.94 cm for the central film and differs from the MC calculated value by 6.38%. The largest penumbra value was 2.72 cm for the top film and overestimates the MC data by 17.28%. The smaller values of FWHM and penumbra seen in the central film can be explained by the fact that the central film has the most spherical dose distribution due to the larger contribution of the central beamlet. Furthermore, the peripheral beamlets will have approximately reached their intended size at the central film plane since all beamlet pairs will have traveled the same distance. In contrast, at the top and bottom films the central beamlet contributes less to the dose distribution and the peripheral beamlets are both less spherical and differ in size since the have traveled different distances at the top and bottom film plane.

While the results of the bottom and central films agree fairly well with the MC data, the top film and MC data have the most disparity. This is likely explained by setup error as the location and shape of each beamlet's irradiated area was dependent on the vertical position of the x-ray tube and horizontal position of the brass collimator as well as its angle which ideally should be perpendicular to the x-ray tube's beam axis. If the wooden support of the brass

collimator was not perfectly level the angle of the collimator would have deviated and the deviation would have been most pronounced at the top of the collimator.

The larger size of the cylindrical phantom more closely mimics the size of human anatomy. While a 5.8-cm × 5.8-cm square is too small to represent any part of human anatomy that would be irradiated the 20-cm diameter cylinder could feasibly represent a large head or a small torso. The benefits of both the larger size of the cylindrical phantom and its cylindrical shape are seen in the two-dimensional film dose distribution and profile. The relative dose levels at the periphery of the phantom are much lower than those seen in the rectangular phantom and the profile is sharper due to the equal thickness of material the beamlets pass through at all irradiation angles. The FWHM, penumbra and target-to-skin ratio were calculated as 1.64 cm, 0.67 cm and 17.00, respectively. MC data was not provided for the cylindrical phantom due to the fact that TIVAR 1000 is a patented material. While we knew the density of the material we did not know the composition and could not properly model the phantom.

The dose rate of 2.09 Gy/minute for the rectangular phantom is certainly high enough for clinical treatment. However, it is unlikely that any patient anatomy size similar to the rectangular phantom would be irradiated. The dose rate of 0.36 Gy/minute for cylindrical phantom is likely too low for clinical treatment. A higher dose rate would be more applicable for clinical irradiation. However, previous MC simulations of KVAT with a higher energy of 200 kV, a higher current of 200 mA and a more sophisticated collimator with 70 apertures delivered dose rates of 0.66 Gy/minute for a 3 cm lung lesion[81].

The main goal of this study was to experimentally show evidence of the skin-sparing effect of a simple KVAT prototype system. Both the 5.8-cm rectangular solid water phantom and the cylindrical 20-cm diameter phantom show higher levels of dose in the central regions of their

dose distributions in comparison to their periphery. It can therefore be said that a skin-sparing effect was achieved. The larger cylindrical phantom shows a higher level of skin sparing with a target-to-skin ratio of 17.00 in comparison to values of approximately 4 for the rectangular phantom. In our previous study we chose to use a dose limit of 250 cGy per fraction for skin. Using target-to-skin ratios of 17 and 4, doses of 4250 cGy and 1000 cGy could be delivered the a small region in the center of the cylindrical and rectangular phantom, respectively, without exceeding dose tolerances on skin.

The secondary objective of this study was to validate the MC model of the KVAT prototype using the experimental film data of the rectangular phantom. While the film located in the top position of the phantom showed a discrepancy in dose profiles and metrics of FWHM, penumbra size and target-to-skin ratio the differences can be explained by non-ideal experimental setup. In contrast, the central and bottom film data's metrics and dose profiles all agree within 10% of the MC calculated data. An agreement within 5% would strengthen confidence in the MC model. However, given the un-sophisticated experimental of the brass collimator this would be difficult. A more robust experimental setup would require a mechanism to fix the brass collimator in relation to the x-ray tube and have a means of precision adjustment.

7.5 Conclusions

Using a simple prototype KVAT system, 160 kVp x-rays were collimated into a linear array of five converging beamlets. These beamlets were used to irradiate a 5.8 cm × 5.8 cm × 4.2 cm rectangular solid water phantom and 20 cm diameter cylindrical phantom in a 360-degree arc and dose was measured with radiochromic films. MC simulations of the rectangular solid water phantom agreed with measured values of FWHM, penumbra size, target-to-skin ratio and dose-profiles within 10% for two out of three films in the rectangular solid water phantom. The discrepancies of the third film can be explained by sensitive experimental setup errors. Target-to-

skin ratios of both the rectangular and cylindrical phantom demonstrated skin-sparing effects with the most pronounced skin sparing occurring in the larger cylindrical phantom. The work performed here has demonstrated the skin-sparing ability of a simple KVAT prototype. Future work will consist of developing a more robust experimental setup to reduce experimental uncertainties and improve the prototype KVAT system.

8. Concluding Remarks

8.1 Summary

The work performed in this PhD project aimed to develop, evaluate and validate a cost-effective kilovoltage x-ray arc therapy system through the use of Monte Carlo modeling and experimental dosimetry. While estimates of cost are difficult to make at such an early point in development, the ideal is that this system will cost no more than 5% of a MV linac.

In the first study a MC model of an early transmission anode KVAT system was used to generate treatment plans for cylindrical water phantoms and a breast patient in the prone and supine position. The intent of this work was to theoretically demonstrate the skin sparing ability of 200 kV KVAT. Results indicated that skin sparing could be achieved with the best skin sparing occurring when a full 360-degree arc was used. Furthermore, smaller PTV volumes and full 360-degree arcs had better dosimetric characteristics.

The second study undertaken increased the complexity of KVAT treatment plans by simulating breast, lung and prostate patients. In this work, idealized spherical PTVs of 3-cm, in the breast and lung patient, and 4-cm diameter, in the prostate patient, were irradiated using the transmission anode KVAT model. 200kV x-rays were used for the breast patient and 225 kV x-rays were used for the lung and prostate patient. As a benchmark, 6 MV linac treatment plans were generated for the breast and lung patient and a 15 MV treatment plan was generated for the prostate patient. Inverse optimization was used to fully leverage the large number of non-coplanar beamlets of KVAT and improve the quality of the KVAT plans. The quality of the treatment plans was evaluated primarily based on dose constraints to OARs. It was found that all KVAT plans met dose constraints for OARs. However, the large amount of boney anatomy in the prostate plan increased overall treatment time and resulted in large amounts of healthy, but

non-critical tissue, receiving large amounts of dose. Thus it was concluded that cancers surrounded by a large amount of bone might not be suitable for KVAT treatment.

The third work aimed to expand upon the second study by simulating realistic, non-spherical PTV volumes in lung cancer patients. This study was also the first to use a completely new design of the KVAT system which used a reflection anode and re-designed collimator. The significance of this model was bolstered by the fact that it was designed based on the specifications of the actual commercial prototype KVAT system being constructed by PrecisionRT. 200 kV KVAT treatment plans were generated for three lung SABR patients with clinically contoured PTVs. Using a treatment planning method similar to GammaKnife, non-spherical PTVs were covered by spherical sub-volumes. The KVAT plans were compared to the 6 MV SABR plans delivered to each of the patients at the Vancouver Island Cancer Centre. Once again, the KVAT treatment plans were primarily evaluated in terms of the dose delivered to OARs. It was found that only the ribs of one patient exceeded dose constraints. However, the location of the PTV of this patient was directly adjacent to the rib cage and this result was not unexpected. The conclusion of this study was that KVAT treatment of smaller lung cancers was safe from the perspective of dose-constraints except for patients with cancers directly next to ribs. While these patients with cancers in proximity to ribs may not be ruled out completely for treatment, the risk of radiation-induced rib fracture would be increased.

Since the previous studies had demonstrated the capabilities and limits of the MC modeled KVAT system, the final step of this PhD project was to experimentally demonstrate the skin sparing ability of kV x-rays from a proof-of-principle KVAT system. In this study a simple brass collimator was fabricated and used along with a tabletop x-ray tube system. Five converging beamlets were produced by the brass collimator and used to irradiate a small

rectangular phantom of solid water and a larger cylindrical phantom of high-density polyethylene. During irradiation the phantoms were rotated 360-degrees to achieve arc therapy. Dose was measured using Gafchromic film and compared to MC simulations. Both film and MC data indicated that kV x-rays could deliver clinically relevant doses of at least 2 Gy while not exceeding dose limits on skin.

In summary, the work performed in this PhD has demonstrated the ability of a modeled KVAT system to generate treatment plans for breast, lung and prostate patients which deliver clinical doses to PTVs without exceeding doses to at-risk organs. Use of multiple spherical sub-volumes allows coverage of non-spherical PTVs. Finally, the crux of the KVAT system - that skin sparing can be achieved with kV x-rays - was experimentally demonstrated using a proof-of-principle KVAT system.

8.2 Future Work

Several areas of future work on the KVAT project still remain at the time of writing this dissertation. The most notable area will be working with the experimental prototype being built by PrecisionRT, which is in its final stages of construction. Much work can be done with this but the first step would be to compare the dosimetric characteristics of the real system to the Monte Carlo model based on the system. Once the model has been validated, it could be used to explore KVAT treatment of other cancer sites.

Another area of future work that is important is the development of a dedicated optimization algorithm for KVAT. While the McGill optimization framework worked well for the purposes of this dissertation there are certain features that would be beneficial to KVAT optimization, such as defining a minimum or maximum weighting of specific beamlets.

Lastly, the 200 kV x-rays of KVAT are in a favourable energy range for dose enhancement via gold nanoparticles. Simulations should be conducted to investigate the dose enhancement of KVAT treatments in comparison to MV photon treatments. It is possible that KVAT will have a greater dose enhancement effect which would allow treatment times and dose to at-risk organs to be reduced.

9. References

1. Breitkreutz DY, Renaud MA, Seuntjens J, Weil MD, Zavgorodni S, Bazalova-Carter M. Inverse optimization of low-cost kilovoltage x-ray arc therapy plans. *Med Phys*. 2018. doi:10.1002/mp.13153
2. M.B. B, M. F. Role of radiotherapy in cancer control in low-income and middle-income countries. *Lancet Oncol*. 2006;7(7):584-595.
3. Otto K. Volumetric modulated arc therapy : IMRT in a single gantry arc. *Med Phys*. 2008;35(1). doi:10.1118/1.2818738
4. Atun R, Jaffray DA, Barton MBM, et al. *Expanding Global Access to Radiotherapy*. Vol 16.; 2015. doi:10.1016/S1470-2045(15)00222-3
5. Rodin D, Jaffray D, Atun R. The need to expand global access to radiotherapy. *Lancet Oncol*. 2014;16(10).
6. Datta N, Samiei M, Bodis S. Radiation therapy infrastructure and human resources in low- and middle-income countries: present status and projections for 2020. *Int J Radiat Oncol Biol Phys*. 2014;89(3).
7. Feain IJ, Court L, Palta JR, Beddar S, Keall P. Innovations in Radiotherapy Technology. *Clin Oncol*. 2017;29(2):120-128. doi:10.1016/j.clon.2016.10.009
8. Yap ML, Zubizarreta E, Bray F, Ferlay J, Barton M. Global Access to Radiotherapy Services: Have We Made Progress During the Past Decade? *J Glob Oncol*. 2016;2(4):207-215. doi:10.1200/JGO.2015.001545
9. Yap ML, Hanna TP, Shafiq J, et al. The Benefits of Providing External Beam Radiotherapy in Low- and Middle-income Countries. *Clin Oncol*. 2017;29(2):72-83. doi:https://doi.org/10.1016/j.clon.2016.11.003

10. Barton MB, Zubizarreta E, Gospodarowicz M. Radiotherapy in Low- and Middle-income Countries. What Can We Do Differently? *Clin Oncol*. 2017;29(2):69-71. doi:10.1016/j.clon.2016.11.009

11. Zubizarreta E, Van Dyk J, Lievens Y. Analysis of Global Radiotherapy Needs and Costs by Geographic Region and Income Level. *Clin Oncol*. 2017;29(2):84-92. doi:https://doi.org/10.1016/j.clon.2016.11.011

12. Johns H, Cunningham J. *The Physics of Radiology*. 4th Editio. Charles C Thomas; 1983.

13. Khan F. *The Physics of Radiation Therapy*. 3rd Editio. Lippincott Williams & Wilkins; 2003.

14. Berger, M.J., Hubbell, J.H., Seltzer, S.M., Chang, J., Coursey, J.S., Sukumar, R., Zucker, D.S., and Olsen K. XCOM: Photon Cross Sections Database.

15. Videtic GMM, Singh AK, Chang JY, et al. *RTOG 0915: A Randomized Phase II Study Comparing 2 Stereotactic Body Radiation Therapy Schedules for Medically Inoperable Patients with Stage I Peripheral Non-Small Cell Lung Cancer*.; 2014.

16. IAEA. *Radiation Biology: A Handbook for Teachers and Students*.; 2010.

17. Joiner M, van der Kogel A, eds. *Basic Clinical Radiobiology*. Fourth Edi. London: Hodder Arnold; 2009.

18. Nikjoo H, Lindborg L. RBE of low energy electrons and photons. *Phys Med Biol*. 2010;55(10). doi:10.1088/0031-9155/55/10/R01

19. ICRP. Recommendations of the International Commission on Radiological Protection. *Ann ICRP*. 1991.

20. Amols HI, Lagueux B, Cagna D. Radiobiological Effectiveness (RBE) of Megavoltage X-Ray and Electron Beams in Radiotherapy. *Radiat Res*. 1986;105.

21. Kawrakow I, Fippel M. VMC++, a MC algorithm optimized for electron and photon beam dose calculations for RTP. In: *Proceedings of the 22nd Annual International Conference of the IEEE Engineering in Medicine and Biology Society (Cat. No.00CH37143)*. Vol 2. ; 2000:1490-1493 vol.2. doi:10.1109/IEMBS.2000.898024

22. Agostinelli S, Allison J, Amako K, et al. Geant4—a simulation toolkit. *Nucl Instruments Methods Phys Res Sect A Accel Spectrometers, Detect Assoc Equip*. 2003;506(3):250-303. doi:https://doi.org/10.1016/S0168-9002(03)01368-8

23. Rogers DWO, Walters B, Kawrakow I. BEAMnrc Users Manual. *Man - Guid*. 2011;509:1-260. http://irs.inms.nrc.ca/software/beamnrc/documentation/pirs0509/pirs0509.pdf.

24. Walters B, Kawrakow I, Rogers DWO. *DOSXYZnrc Users Manual*.; 2018.

25. Briesmeister JF. MCNP – A General Monte Carlo N-Particle Transport Code. *Los Alamos Natl Lab*. 2000;(March):790.

26. Salvat F, Fernandez-Varea JM, Acosta E, Sempau J. *Penelope - A Code System for Monte Carlo Simulation of Electron and Photon Transport*. Nuclear Energy Agency of the OECD (NEA): Organisation for Economic Co-Operation and Development - Nuclear Energy Agency; 2001. http://inis.iaea.org/search/search.aspx?orig_q=RN:33008692.

27. Johnstone CD, Bazalova-carter M. MicroCT imaging dose to mouse organs using a validated Monte Carlo model of the small animal radiation research platform ((SARRP). *Phys Med Biol*. 2018;63.

28. Seco J, Verhaegen F, eds. *Monte Carlo Techniques in Radiation Therapy*.; 2013.

29. Ma CM, Coffey CW, DeWerd LA, et al. AAPM protocol for 40 – 300 kV x-ray beam dosimetry in radiotherapy and radiobiology. *Med Phys*. 2001;28(6).

doi:10.1118/1.1374247

30. Niroomand-rad A, Blackwell CR, Coursey BM, et al. Radiochromic film dosimetry : Recommendations of AAPM Radiation Therapy Committee Task Group 55. *Med Phys*. 1998;25(11).

31. Renaud M-AA, Serban M, Seuntjens J. On mixed electron-photon radiation therapy optimization using the column generation approach. *Med Phys*. 2017;44(8):4287-4298. doi:10.1002/mp.12338

32. Desaulniers G, Desrosiers J, Solomon M, eds. *Column Generation*. Springer; 2005.

33. Bentzen SM, Heeren G, Cottier B, et al. Towards evidence-based guidelines for radiotherapy infrastructure and staffing needs in Europe: The ESTRO QUARTS project. *Radiother Oncol*. 2005. doi:10.1016/j.radonc.2004.12.007

34. World Health Organization. The Global Burden of Disease: 2004 update. *2004 Updat*. 2004:146. doi:10.1038/npp.2011.85

35. Prionas ND, McKenney SE, Stern RL, Boone JM. Kilovoltage rotational external beam radiotherapy on a breast computed tomography platform: A feasibility study. *Int J Radiat Oncol Biol Phys*. 2012. doi:10.1016/j.ijrobp.2011.12.042

36. Bazalova-Carter M, Weil MD, Breitkreutz DY, Wilfley BP, Graves EE. Feasibility of external beam radiation therapy to deep-seated targets with kilovoltage x-rays: *Med Phys*. 2017. doi:10.1002/mp.12047

37. Bazalova M, Weil MD, Wilfley B, Graves EE. Monte Carlo model of the scanning beam digital x-ray (SBDX) source. *Phys Med Biol*. 2012;57(22):7381-7394. doi:10.1088/0031-9155/57/22/7381

38. Kawrakow I, Mainegra-Hing E, Rogers DWO, Tessier F, Walters BRB. *The EGSnrc Code*

System: Monte Carlo Simulation of Electron and Photon Transport.; 2018.

39. Ali ESM, Rogers DWO. Efficiency improvements of x-ray simulations in EGSnrc user-codes using bremsstrahlung cross-section enhancement (BCSE). *Med Phys*. 2007. doi:10.1118/1.2736778

40. Mohan, R., Chui, C., Lidofsky L. Energy and angular distributions of photons from medical linear accelerators. *Med Phys*. 1985;12(5):592-597.

41. Kry SF, Smith SA, Weathers R, Stovall M. Skin dose during radiotherapy: A summary and general estimation technique. *J Appl Clin Med Phys*. 2012;13(3):20-34. doi:10.1118/1.3469011

42. Vicini F. *RTOG 0319: A Phase I/II Trial to Evaluate Three Dimensional Conformal Radiation Therapy (3D-CRT) Confined to the Region of the Lumpectomy Cavity for Stage I and II Breast Carcinoma*.

43. Vicini F, White J. RTOG 0413 NSABP B-39: A Randomized Phase III Study of Conventional Whole Breast Irradiation (WBI) versus Partial Breast Irradiation (PBI) for Women with Stage 0, I or II Breast Cancer.

44. Zavgorodni S, Bush K, Locke C, Beckham W. *Vancouver Island Monte Carlo (VIMC) System for Radiotherapy Treatment Planning Dosimetry and Research*.; 2007.

45. Hasenbalg F, Fix MK, Born EJ, Mini R, Kawrakow I. VMC++ versus BEAMnrc: A comparison of simulated linear accelerator heads for photon beams. *Med Phys*. 2008. doi:10.1118/1.2885372

46. Graves EE, Quon A, Loo BW. RT_Image: An open-source tool for investigating PET in radiation oncology. *Technol Cancer Res Treat*. 2007;6(2):111-121.

47. ICRP. *Report of Task Group on Reference Man*. Vol 23.; 1975. doi:10.1016/S0074-

2740(75)80018-3

48. Lindfors KK, Boone JM, Nelson TR, Yang K, Kwan AL, Miller DF. Dedicated Breast CT: Initial Clinical Experience. *Radiology*. 2008;246(3):725-733.

49. Lee N, Chuang C, Quivey JM, et al. Skin toxicity due to intensity-modulated radiotherapy for head-and-neck carcinoma. *Int J Radiat Oncol Biol Phys*. 2002;53(3):630-637. doi:10.1016/S0360-3016(02)02756-6

50. Szeifert GT, Kondziolka D, Levivier M, Lunsford LD, eds. Radiosurgery and Pathologic Fundamentals. In: 1st ed. Basel: Karger; 2007:20-21.

51. Chin LS, Regine WF, eds. Principles and Practice of Stereotactic Radiosurgery. In: 2nd Ed. New York City: Springer Publishing; 2015:41.

52. Aoki M, Sato M, Hirose K, et al. Radiation-induced rib fracture after stereotactic body radiotherapy with a total dose of 54–56 Gy given in 9–7 fractions for patients with peripheral lung tumor: impact of maximum dose and fraction size. *Radiat Oncol*. 2015;10(1):1-8. doi:10.1186/s13014-015-0406-8

53. Fahimian B, Yu V, Horst K, Xing L, Hristov D. Trajectory modulated prone breast irradiation: A LINAC-based technique combining intensity modulated delivery and motion of the couch. *Radiother Oncol*. 2013;109(3):475-481. doi:10.1016/j.radonc.2013.10.031

54. Laissue J, Blattmann H, Slatkin D. Alban Köhler (1874-1947): Inventor of grid therapy. *Z Med Phys*. 2012;22(2).

55. Rose JH, Norman A, Ingram M, Aoki C, Solberg T, Mesa A. First radiotherapy of human metastatic brain tumors delivered by a computerized tomography scanner (CTRx). *Int J Radiat Oncol • Biol • Phys*. 1999;45(5):1127-1132. doi:10.1016/S0360-3016(99)00347-8

56. Abbas H, Mahato DN, Satti J, MacDonald CA. Measurements and simulations of focused beam for orthovoltage therapy. *Med Phys*. 2014;41(4):041702. doi:10.1118/1.4866224

57. Breitkreutz DY, Weil MD, Zavgorodni S, Bazalova-Carter M. Monte Carlo simulations of a kilovoltage external beam radiotherapy system on phantoms and breast patients: *Med Phys*. 2017. doi:10.1002/mp.12619

58. Kurup G. CyberKnife: A new paradigm in radiotherapy. *J Med Phys*. 2010;35(2).

59. Walters B, Kawrakow I, Rogers DWO. DOSXYZnrc Users Manual. *NRCC Rep PIRS-0794*. 2007:1-125.

60. Bradley J, Choy H, Masters G. *RTOG 0617: A Randomized Phase III Comparison of Standard- Dose (60 Gy) Versus Highdose (74 Gy) Conformal Radiotherapy with Concurrent and Consolidation Carboplatin/Paclitaxel +/- Cetuximab (IND #103444) in Patients with Stage IIIA/IIIB Non-Small Cell Lung*.; 2016.

61. Amin MB, Angeles L, Bruner DW, et al. *RTOG 0415: A Phase III Randomized Study of Hypofractionated 3DCRT/IMRT versus Conventionally Fractionated 3DCRT/IMRT in Patients Treated for Favorable-Risk Prostate Cancer*.; 2015.

62. Garofalo MC, Hong T, Hospital MG, et al. RTOG 0822: A Phase II Evaluation of Preoperative Chemoradiotherapy Utilizing Intensity Modulated Radiation Therapy (IMRT) in Combination With Capecitabine and Oxaliplatin for Patients With Locally Advanced. 2011.

63. Wang D. RTOG 0630: A Phase II Trial of Image Guided Preoperative Radiotherapy for Primary Soft Tissue Sarcomas of the Extremity.

64. Zavgorodni S, Bush K, Locke C, Beckham W. Vancouver Island Monte Carlo (VIMC) system for radiotherapy treatment planning dosimetry and research. *Radiother Oncol*.

2007;84.

65. Zavgorodni S, Bush K, Townson R. Monte Carlo simulation of RapidArc radiotherapy delivery. *Phys Med Biol*. 2008;53(19):N359.

66. The Mathworks Inc. MATLAB 2016b.

67. ICRU. Report 83: Prescribing, Recording, and Reporting Photon-Beam Intensity-Modulated Radiation Therapy (IMRT). *J ICRU*. 2010;10(1).

68. De Gersem WRT, Derycke S, Colle CO, De Wagter C, De Neve WJ. Inhomogeneous target-dose distributions: A dimension more for optimization? *Int J Radiat Oncol Biol Phys*. 1999;44(2):461-468. doi:10.1016/S0360-3016(98)00464-7

69. Di Lillo F, Mettivier G, Castriconi R, et al. Synchrotron radiation external beam rotational radiotherapy of breast cancer: proof of principle. *J Synchrotron Radiat*. 2018;1(25).

70. Deloar HM, Kunieda E, Kawase T, et al. *Monte Carlo Simulations for Stereotactic Radiotherapy System with Various Kilo-Voltage x-Ray Energy*. Japan; 2005. http://inis.iaea.org/search/search.aspx?orig_q=RN:38045779.

71. Deloar HM, Kunieda E, Kawase T, et al. Investigations of different kilovoltage x-ray energy for three-dimensional converging stereotactic radiotherapy system: Monte Carlo simulations with CT data. *Med Phys*. 2006;33(12):4635-4642. doi:10.1118/1.2361080

72. Garnica-Garza HM. Stereotactic breast irradiation with kilovoltage x-ray beams. *Phys Med Biol*. 2016;61(2):983. http://stacks.iop.org/0031-9155/61/i=2/a=983.

73. Sanchez-Arreola S V, Garnica-Garza HM. Feasibility of robotic stereotactic body radiotherapy of lung tumors with kilovoltage x-ray beams. *Med Phys*. 2017;44(4):1224-1233. doi:10.1002/mp.12140

74. Fagerstrom JM, DeWerd LA, Palmer B, Culberson WS. Prototype modulated orthovoltage

stereotactic radiosurgery cones. *Radiat Meas*. 2018;119(September):33-41. doi:10.1016/j.radmeas.2018.09.002

75. Ferlay J, Soerjomataram I, Dikshit R, et al. Cancer incidence and mortality worldwide: Sources, methods and major patterns in GLOBOCAN 2012. *Int J Cancer*. 2015;136(5):E359-E386. doi:10.1002/ijc.29210

76. Bank MI. Superimposition of beams to vary shot size in gamma knife stereotactic radiosurgery. *J Appl Clin Med Phys*. 2002;3(1):19. doi:10.1120/1.1428242

77. Benedict SH, Yenice KM, Followill D, et al. Stereotactic body radiation therapy: The report of AAPM Task Group 101. *Med Phys*. 2010;37(8):4078-4101. doi:10.1118/1.3438081

78. The Mathworks Inc. MATLAB 2017b.

79. Feuvret L, Noël G, Mazeron J-J, Bey P. Conformity index: A review. *Int J Radiat Oncol • Biol • Phys*. 2006;64(2):333-342. doi:10.1016/j.ijrobp.2005.09.028

80. Alaei P, Spezi E. Imaging dose from cone beam computed tomography in radiation therapy. *Phys Medica*. 2015;31(7):647-658. doi:10.1016/j.ejmp.2015.06.003

81. Breitkreutz DY, Renaud M-A, Weil MD, et al. Kilovoltage x-ray arc therapy for three lung cancer patients. *Under Rev*. 2019.

82. Marroquin EYL, González JAH, López MAC, Barajas JEV, García-garduño OA. Evaluation of uncertainty in Gafchromic EBT3 film. *J Appl Clin Med Phys*. 2016;17(5):466-481.